TU Wien

Diploma Thesis

Investigation of mixed conducting oxygen storage electrodes via chemical capacitance measurements

Author:
Barbara Wagner

Supervisors:
Univ.Prof. Dipl.Phys. Dr.rer.nat.
Jürgen Fleig

Projektass. Dipl.-Ing. Dr.techn. BSc.
Alexander Schmid

Projektass. Dipl.-Ing. Dr.techn. BSc.
Martin Krammer

A thesis submitted in fulfilment of the requirements for the degree of
Master of Science at the

Institute of Chemical Technologies and Analytics

07.08.2023, Vienna

Barbara Wagner

Abstract

Solid Mixed Ionic Electronic Conductors (MIECs) are frequently used in energy applications, such as high temperature Solid Oxide Fuel Cells (SOFC), Solid Oxide Electrolysis Cells (SOEC) and oxygen permeation membranes. However, their ability to conduct both ionic oxygen vacancies and electronic charge carriers and the resulting variability of the oxygen non-stoichiometry also makes them attractive oxide ion battery anode and cathode materials. Those are based on the transport of O^{2-} ions between the anode and cathode through an electrolyte via oxygen vacancies. Therefore, suitable electrode materials not only need good ion and electron conductivity, but also a highly variable oxygen non-stoichiometry (δ) to chemically store large amounts of charge. In this work, several candidates ($La_{0.6}Sr_{0.4}FeO_{3-\delta}$ (LSF), Gd:CeO_2 (GDC), $La_{0.5}Sr_{0.5}Cr_{0.2}Mn_{0.8}O_{3-\delta}$ (LSCrMn), $La_2NiO_{4+\delta}$ (LNO), $YBaCo_4O_{7-\delta}$ ($YBCo_4O_7$) and $SrTiO_3$ Strontium Titanate (STO), $La_{0.8}Ca_{0.2}FeO_{3-\delta}$ (LCF)) are investigated for their usability as electrode materials in oxide ion batteries. Thin film microelectrodes were prepared on Yttrium stabilized Zirconia (YSZ) single crystal solid electrolytes. Electrochemical Impedance Spectroscopy (EIS) measurements were conducted over a wide range of temperatures (T = 300 − 600 °C) and frequencies ($f = 10^6 - 4 \cdot 10^{-3}$ Hz). The chemical capacitance extracted from the impedance spectra allow predicting the charge/discharge characteristics of the corresponding electrode. These were then compared with charge/discharge characteristics obtained by DC voltage measurements.

Kurzfassung

Feste gemischtleitende Oxide (MIECs) werden häufig in Energieanwendungen wie zum Beispiel Hochtemperatur-Festoxid-Brennstoffzellen (SOFC), Festoxid-Elektrolysezellen (SOEC) und Sauerstoffpermeationsmembranen eingesetzt. Die Eigenschaft, sowohl ionische Sauerstoffleerstellen als auch elektronische Ladungsträger zu leiten, und die daraus resultierende Variabilität der Sauerstoff-Nichtstöchiometrie machen sie jedoch auch zu attraktiven Anoden- und Kathodenmaterialien für Oxidionenbatterien. Diese basieren auf dem Transport von O^{2-}-Ionen zwischen Anode und Kathode durch einen Elektrolyten über Sauerstoffleerstellen. Geeignete Elektrodenmaterialien benötigen daher nicht nur eine gute Ionen- und Elektronenleitfähigkeit, sondern auch eine Variabilität an der Sauerstoff-Nichtstöchiometrie (δ), um große Mengen an Ladung chemisch zu speichern. In dieser Arbeit wurden diverse Materialien ($La_{0.6}Sr_{0.4}FeO_{3-\delta}$ (LSF), Gd:CeO_2 (GDC), $La_{0.5}Sr_{0.5}Cr_{0.2}Mn_{0.8}O_{3-\delta}$ (LSCrMn), $La_2NiO_{4+\delta}$ (LNO), $YBaCo_4O_{7-\delta}$ ($YBCo_4O_7$), $SrTiO_3$ Strontium Titanate (STO), $La_{0.8}Ca_{0.2}FeO_{3-\delta}$ (LCF)) auf ihre Verwendbarkeit als Elektrodenmaterialien in Oxidionenbatterien untersucht. Dafür wurden Dünnfilm-Mikroelektroden auf Einkristall-Festelektrolyten aus yttriumstabilisiertem Zirkonoxid YSZ hergestellt. Anschließend wurden elektrochemische Impedanzspektroskopie (EIS) Messungen über einen breiten Temperatur- (T = 300 - 600 °C) und Frequenzbereich (f = 10^6 - $4 \cdot 10^{-3}$ Hz) durchgeführt. Die, aus den Impedanzspektren bestimmte, chemische Kapazität ermöglicht die Vorhersage der Lade-/Entladekurven der entsprechenden Elektrode. Diese wurden anschließend mit den Lade-/Entladekurven von Gleichspannungsmessungen verglichen.

List of Symbols

μ	Chemical Potential
μ_i^0	Standard Chemical Potential
σ_{ion}	Ionic Conductivity
C	Capacitance [F]
c_{O}	Oxygen Site Concentration in the Lattice
C_{chem}	Chemical Capacitance [$\mathrm{F} \cdot \mathrm{cm}^{-3}$]
d	Electrode Diameter (µm)
D^{σ}	Diffusion Coefficient [$\mathrm{m}^2 \cdot \mathrm{s}^{-1}$]
e	Elemental Charge
F	Faraday Constant [96485.3415 As $\cdot mol^{-1}$]
f	Frequency [Hz]
f_{max}	Maximum Frequency (Hz)
f_{min}	Minimum Frequency (Hz)
h	Electrode Height (nm)
I	Current [A]

j Imaginary Unit

k^{σ} Surface Exchange Coefficient

k_B Boltzmann Constant [$1.3806 \cdot 10^{-23}\ \mathrm{m}^2 \cdot \mathrm{kg} \cdot \mathrm{s}^{-2} \cdot \mathrm{K}^{-1}$]

$p_{O_2,\ chamber}$ Oxygen Pressure in the Measuring Chamber [mbar]

$p_{O_2,\ norm}$ Standard Oxygen Pressure [1013 mbar]

p_{O_2} Oxygen Partial Pressure [mbar]

$p^{\star}_{O_2}$ Effective Oxygen Partial Pressure [mbar]

Q Specific Capacity [$\mathrm{mA} \cdot \mathrm{h} \cdot \mathrm{g}^{-1}$]

R Universal Gas Constant [$8.3145\ \mathrm{J} \cdot \mathrm{mol}^{-1} \cdot \mathrm{K}^{-1}$]

R_S Incorporation Resistance [Ω]

R_T Transport Resistance [Ω]

T Temperature [K]

t Time [s]

T_{max} Maximum Temperature (°C)

T_{min} Minimum Temperature (°C)

U Voltage [V]

$V_{A,limit}$ Maximum Anodic Potential (V)

$V_{A,step}$ Anodic Potential Step (V)

$V_{C,max}$ Maximum Cathodic Potential (V)

$V_{C,step}$ Cathodic Potential Step (V)

$V_{C,step}$ Cathodic Potential Step (V)

Contents

1 Introduction

Fossil fuels, like coal, oil, and natural gas, have been the primary source of energy for a long time now, due to their high energy density and ease of use. However, they do come with several significant disadvantages. Their extraction and combustion are one of the biggest contributors to air pollution, greenhouse gases and harmful microparticles world wide. All of these have detrimental impacts on the environment and human health, due to their link to an increase in strokes, heart diseases, lung cancer, acute and chronic respiratory diseases. Fossil fuel consumption also contributes to climate change, leading to global warming, rising sea levels, and extreme weather events[1]–[3]. Another downside to fossil fuel is, that the reserves are finite and becoming increasingly difficult and expensive to extract, meaning than sooner than later, the lack of them will lead to concerns about future energy security[4]. All of these detrimental effects of fossil fuels have heralded a transition to renewable energy sources, like solar, wind or hydroelectric power, that offer a sustainable and "green" alternative to fossil fuels[5]. However, due to the intermittent nature of renewable energy sources, e.g the sun not always shining or windless days, these energy sources requires efficient energy storage solutions to ensure a consistent and reliable power supply for the population. Excess energy needs to be stored during times of high production and released, when demand exceeds the generated supply[6],[7]. Lithium-ion batteries have emerged as a leading energy storage solution, driven by their high energy density, efficiency, and versatility[8]. However, the widespread usage of lithium-ion batteries poses great challenges. Lithium is a critical metal and not available in abundance. Due to the scarcity of lithium resources, the challenging recycling process, alternatives and as the demand for electric cars, consumer electronic devices and energy storage systems grows, concerns start to arise about a lithium shortages in the near future. The limited global reserves, combined with geopolitical turmoil and complex and health detrimental extraction processes, highlight the need to find sustainable methods for lithium extraction, processing, recycling and alternatives[9]. Due to these problems with lithium and lithium-ion batteries, it is essential to diversify energy storage technologies. One promising new development is the Oxygen Ion Battery (OIB). OIBs operate on a similar principle as lithium-ion batteries, utilizing oxygen ions instead of lithium ions, and they offer several advantages, especially regarding an

improvement in safety and the use of more abundant materials. Electrodes and electrolyte of OIBs are solid oxides, giving them the advantage, that they are not flammable. One of the most important possible future applications, due to their higher operating temperatures, is the usage in stationary energy storage systems. However, OIBs are still in the very early stages of their development. Further research and optimization is required before they are commercially viable and a real competitor to lithium-ion batteries, which do have nearly half a century of a head start[10]. This thesis focuses on the search for new electrode materials for OIBs as one step towards optimization and in making them a strong competitor for the energy storage battery of the future.

2 Theoretical Background

2.1 Crystal Structure

Crystals are defined as solid materials that possess a highly ordered and periodic arrangement of atoms, ions, or molecules in three dimensions. This periodicity directly affects many of the crystal properties, such as their symmetry, mechanical strength, optical properties, and electrical conductivity[11]. The crystal structure of a material is determined by the arrangement of its constituent atoms or molecules. In a perfect crystal, the arrangement is highly ordered and periodic, which means that the same sub arrangement is repeated over and over again in all three dimensions. This periodicity can be described by a lattice, that represents the positions of the constituent atoms or molecules. The lattice is characterised by the unit cell. The unit cell is is the smallest repeating unit of the crystal structure and can be described by its lattice parameters - the lengths of the edges and the angles between them. There are seven so called crystal systems, which are based on the symmetry of the unit cell. Each system has a unique set of lattice parameters. The symmetry is described by the crystallographic point groups, which are groups of symmetry operations that leave the crystal unchanged. There are 32 possible point groups in three dimensions, which are classified into six crystal classes based on their symmetry elements. The crystal classes are: cubic, tetragonal, orthorhombic, monoclinic, triclinic, and hexagonal. Each crystal class is further characterised by its Bravais lattice, which is the specific lattice type that corresponds to that symmetry[11],[12]. Common crystal structures are often named after a specific material, e.g. the fluorite or perovskite structure.

2.1.1 Fluorite MX_2

The fluorite structure is defined by its chemical composition of MX_2. It is a face-centered cubic (FCC) structure in which the X ions occupy the eight tetrahedral lattice sites, while the M ions occupy the regular sites. Examples for such a compound would be Fluorite itself (CaF_2) or Yttria Stabilized Zirconia ($(ZrO_2)_{1-x}(Y_2O_3)_x$). While zirconia (ZrO_2) itself has a monoclinic baddelyte

structure at ambient conditions, it undergoes phase transitions at elevated temperatures. First into a tetragonally distorted fluorite structure at 1170 °C and then into a cubic fluorite structure at 2370 °C[13],[14].

$$monoclinic \underset{950\ °C}{\overset{1170\ °C}{\longleftrightarrow}} tetragonal \overset{2370\ °C}{\longleftrightarrow} cubic \overset{2706\ °C}{\longleftrightarrow} melt$$

To stabilize the cubic structure, Y_2O_3 is used. Figure 2.1 shows the schematic fluorite structure of cubic Yttria-stabilized Zirconia in which there is one oxygen vacancy for every two yttrium ions. The exact defect chemistry is explained in Chapter 2.2.

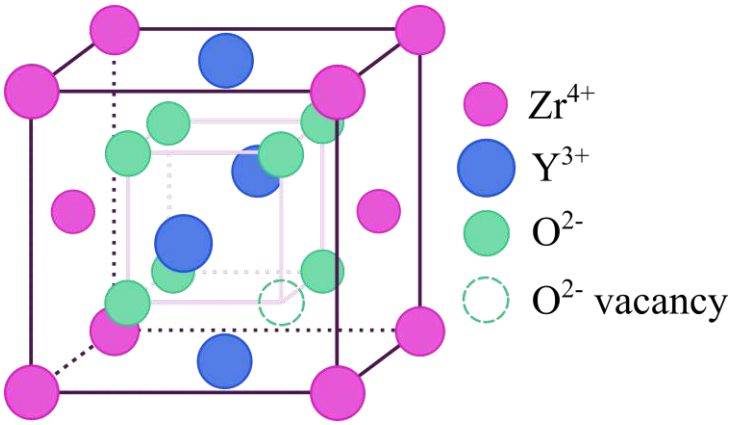

Figure 2.1: Unit cell of the cubic fluorite YSZ structure. Placement of the O^{2-} vacancy and the Y^{3+} ions are randomly selected.

Because of it's excellent properties as a functional and structural ceramic, Yttria-stabilized Zirconia has found widespread usage in SOECs and SOFCs. Especially YSZ stabilized with 8 mol % of Y_2O_3 is often used as a solid electrolyte in such appliances, due to it's high ionic conductivity, while still having good mechanical properties and fracture resistance[15]. The solid electrolyte used in this work was YSZ and a fluorite-type oxide that was investigated in this work was Gd:CeO_2 (GDC).

2.1.2 Perovskite ABO_3

The perovskite-type crystal structure is characterized by the chemical compostion of ABO_3 and it's namesake is the first discovered mineral with this structure, the Perovskite - $CaTiO_3$. Figure 2.2 shows the unit cell of the cubic perovskite structure from a B centered view. When looking at the involved ions, A and B are cations, with A generally being larger than B and a combined

valence of +6, and *O* an anion with the valence of -2, that bonds to both cations. Perovskites are also often easily dopable and many stable forms exist, where either one or both of the *A* and *B* sites are partly replaced by another ion of similar size, resulting in $(A1_{1-x}A2_x)(B1_{1-y}B2_y)$. Because of this the *O* also often deviates from the ideal configuration and results in an oxygen non stoichiometry of the form $O_{3-\delta}$ when the ions A and B change their oxidation states[16].

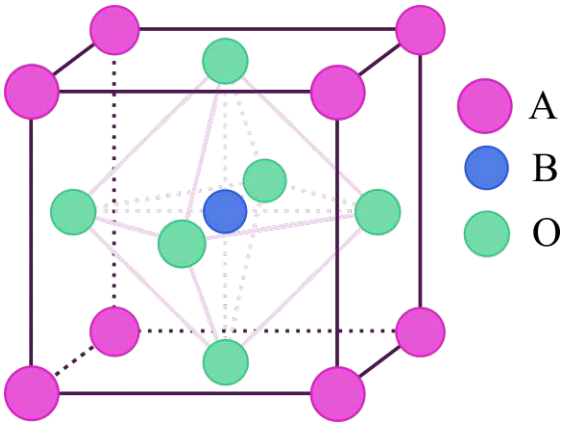

Figure 2.2: B-centered unit cell of a perovskite

Especially MIEC perovskite oxides are of great interest for electrochemical applications, such as SOFC's, SOEC's, oxygen permeation membranes or OIB's. This mixed conducting ability is the result of a high oxygen nonstoichiometry, which results in a good oxygen ion conductivity, and a mixed valence state of a transition metal on the *B* site, that gives the material it's electronic conductivity[17]. Examples for perovskite-type oxides that were investigated in this work are $La_{0.6}Sr_{0.4}FeO_{3-\delta}$ (LSF), $La_{0.5}Sr_{0.5}Cr_{0.2}Mn_{0.8}O_{3-\delta}$ (LSCrMn), $SrTiO_3$ Strontium Titanate (STO), and $La_{0.8}Ca_{0.2}FeO_{3-\delta}$ (LCF).

2.1.3 Ruddlesden-Popper A_2BO_4

The Ruddlesden-Popper structure is a variation of the perovskite-type crystal structure. The layers of the Ruddlesden-Popper structure alternate between rock-salt layers (AO) and perovskite layers (ABO_3) along the vertical axis. The chemical composition of the structure is $A_{n+1}B_nX_{3n+1}$ with *n* representing the number of consecutive perovskite layers between two rock-salt layers, A is a cation of an alkali, alkali metal or rare earth metal and B a transition metal cation. Like in regular MIEC perovskite-type oxides, Ruddlesden-Popper perovskite-type oxides also often possess both electronic and ionic conductivity and therefore also oxygen nonstoichiometry to some extent. Figure 2.3 shows the simplest schematic structure of

a Ruddlesden-Popper crystal, with $n = 1$ and the chemical composition of A_2BO_4[18]. Due to to their spacious crystal structure, Ruddelesden-Popper materials can form interstitials as a defect, which is further explained in Chapter 2.2.

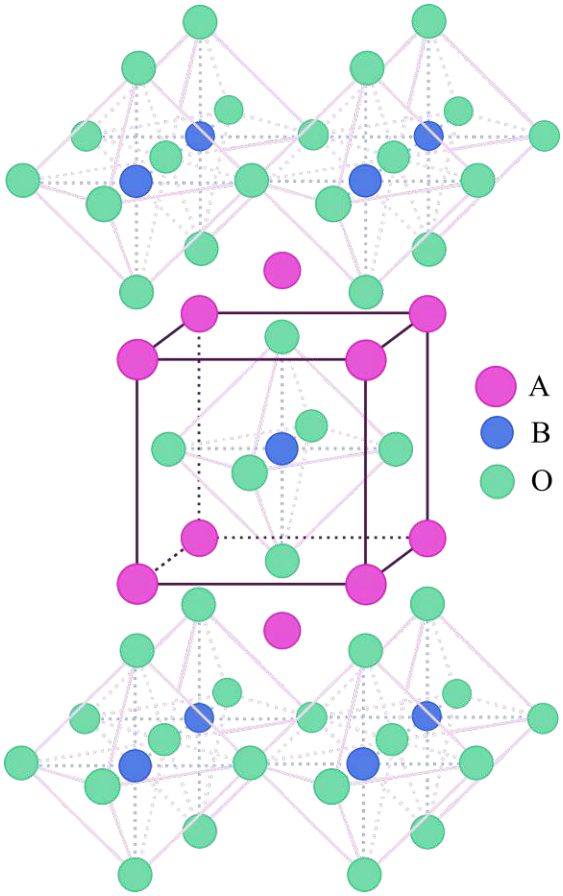

Figure 2.3: Schematic crystal structure of a Ruddleston-Popper perovskite with the chemical composition of A_2BO_4.

An example for a Ruddlesden-Popper perovskite-type oxide that was investigated in this work is LNO.

2.2 Point Defect Chemistry

As the understanding of crystal structures grew, so did the realization, that a perfect crystal only exists in theory and all real crystals possess some kind of defects. What started with the recognition of simple point defects, such as a missing atom or an impurity or different atom in

its place, evolved into its own field of interest, as the complexity of the discovered defects grew. Not long after, defect chemistry started to become a powerful tool to describe the physical and chemical behaviour of materials such as oxides or metals. Nowadays the control and deliberate manipulation of these defects and the effect they have on crystalline solids, plays a central role in material sciences and is used in many different fields of application such as batteries, fuel cells, displays, data storage, computer memories and many more[19],[20].

Defects can be classified in a dimensional hierarchy[21]:

- **Zero-dimensional defects** - Point defects (e.g. missing or interstitial atoms, doping)
- **One-dimensional defects** - Linear defects (e.g dislocations)
- **Two-dimensional defects** - Planar defects (e.g. surface or grain boundaries)
- **Three-dimensional defects** - Volume defects (e.g. clusters, voids or precipitates)

2.2.1 Point Defects in Oxides

In regard to solid state electrochemistry, zero-dimensional point defects are the most important for understanding various electrochemical properties. They can be further classified into either extrinsic or intrinsic point defects. Intrinsic point defects can be vacancies V_M or a self-interstitials M_i. A vacancy is a point defect, where an atom is absent from a normally occupied position (Figure 2.4 a) and a self-interstitial is an extra atom, forced to occupy a space in the crystal, where usually there is none (Figure 2.4 b). Extrinsic point defects always include atoms, foreign to the main crystal lattice. Such extrinsic defects can be foreign interstitials A_i (Figure 2.4 c), where a foreign atom is forced to occupy a space in the crystal lattice of an otherwise monoatomic lattice or foreign substitutional atoms A_M (Figure 2.4 d), where a foreign atom takes the place of a lattice atom in it's stead[19]–[22].

Interstitials and vacancies often occur together, when an atom leaves it's usual lattice occupation and moves across the lattice between ordered atoms. This combination is also called Frenkel disorder (Figure 2.5 a). A crystal only exhibiting Frenkel disorder would therefore have the same concentration of interstitial sites and vacancies[22] A situation with a vacancy pair, consisting of an unoccupied anion and an unoccupied cation site, is called Schottky disorder (Figure 2.5 b). In both cases, charge neutrality remains[23].

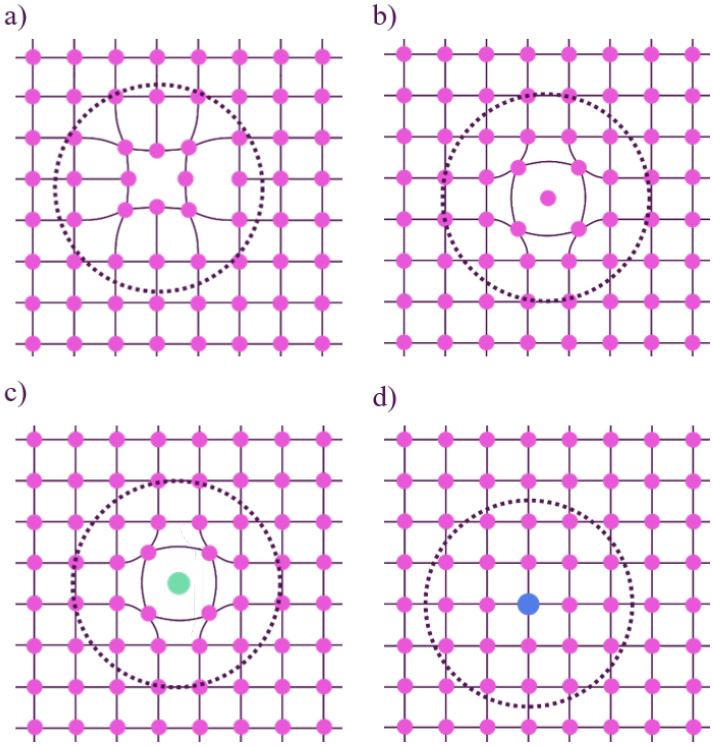

Figure 2.4: Schematic crystal structure with four different point defects.
Intrinsic: a) Vacancy V_M b) Self-Interstitial M_i
Extrinsic: c) Foreign Interstitial A_i d) Foreign Substituitional A_M

However, not all foreign atoms are unwanted. It can be distinguished between unwanted extrinsic defects - impurities - and intentionally introduced foreign atoms - dopants - which are specifically used to enhance or add certain material properties, like conductivity, hardness or thermal stability. The substitution with differently charged atoms is possible, however, the crystal system to be stable, it needs to maintain charge neutrality. Therefore, depending on the charge, relative to the substituted ion, a distinction between different dopant types can be made:[23]

- **Acceptor dopants** - The dopant has a lower charge than the substituted lattice ion. Acceptor dopants can be compensated by introducing electron holes, cation interstitials or anion vacancies into the lattice.
- **Donor dopants** - The dopant has a higher charge than the substituted lattice ion. Donor dopants can be compensated with electrons, cation vacancies or anion interstitials.

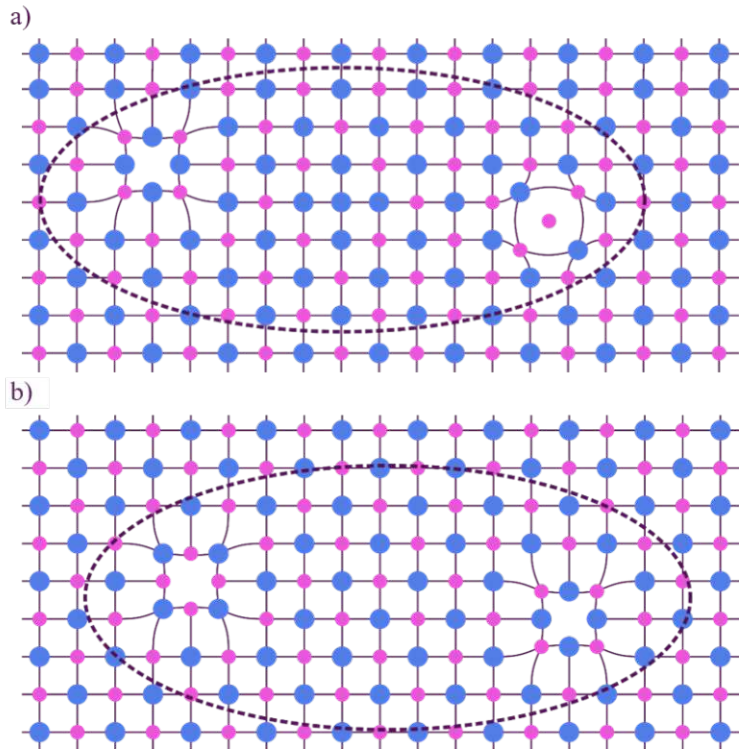

Figure 2.5: Schematic crystal structure showing a) Frenkel disorder b) Schottky disorder

- **Isovalent dopants** - The dopant has the same charge as the substituted lattice ion. However, size differences may affect the mechanical properties of the crystal.

2.2.2 Kröger-Vink-Notation

To describe such point defects in solids, the so called Kröger-Vink-Notation is used[24],[25]. It follows the scheme:

$$M_S^C$$

The main letter M describes the species of the defect and can be:

- **Atoms** - La, Sr, O, ...
- **Vacancies** - V
- **Electrons** - e

- **Electron holes** - h

The subscript S describes the lattice site, that the species occupies. E.g. in $La_{0.6}Sr_{0.4}CoO_{3-\delta}$ (LSC) strontium is used to acceptor dope the lanthanum cobaltite to improve it's ionic conductivity. When doped, strontium occupies lanthanum sites in the lattice. In this case, the main letter M would be replaced by Sr and the subscript S by La (Sr_{La}). If the ion doesn't replace another ion, but an interstice instead, the subscript i is used. For a more general notation, cation sites are also often written as C or M (for metal) and anion sites as A or X.

The superscript C describes the charge of the species in relation to the occupied site. When looking at LSC as the example, Sr with the charge +2 on a La site with the charge +3 results in a single negative charge. Comparing the charges can lead to either a negative, a positive or zero charge, which are represented with different symbols. Negative charges are indicated by $'$, positive charges are indicated by $\cdot$ and for zero charges $\times$ is used. This means that the Kröger-Vink notation for a Sr ion with a +2 charge on a La site with a +3 charge would be Sr'_{La}.

When using the Kröger-Vink-Notation for extrinsic and intrisic defects to describe the full defect reaction it is important to keep all the charges, masses and sites balanced. When looking at the LSC example, the Sr doping results in the formation of oxygen vacancies and holes to keep the charges balanced. (Eq. (2.1))

$$LaCoO_3 \xrightarrow{SrCO_3} 2\,Sr'_{La} + V_O^{\cdot\cdot} + 3\,O_O^{\times} \tag{2.1}$$

2.2.3 Brouwer Diagram

In addition to the aforementioned defects, taking the interaction of the oxide with the surrounding gaseous atmosphere into account, results in a variability of the oxygen stoichiometry due to the incorporation and removal of oxygen. The Brouwer diagram illustrates how the defect concentrations vary in dependence of the oxygen partial pressure. When simplified, there are four different defect types, that are relevant for the Brouwer-Diagram. (Table 2.1)

The effects of the partial pressure can be described with the chemical potential (Eq. (2.2)). A change in the partial pressure leads to a change in the chemical potential, which then results in a driving force in the material to adapt to the new conditions and to adopt a more energetically favorable state.

Table 2.1: Relevant defects for the Brouwer diagram

Kröger-Vink-Notation	Defect
$V_O^{\cdot\cdot}$	2-times positively charged oxygen vacancy
$V_M^{''}$	2-times negatively charged metal vacancy
e'	electron
$h^{\cdot}$	electron hole

$$\mu = \mu_i^0 + RT \cdot ln(p_i) \tag{2.2}$$

These reactions can be described by Equation (2.3) for the reduction (oxygen release) and Equation (2.4) for the oxidation (oxygen incorporation). Therefore, in accordance with the corresponding mass action law, a low partial pressure increases the number of oxygen sites and electrons (Eq. (2.5)), whereas a high partial pressure leads to the formation of more holes and metal vacancies. (Eq. (2.6)).

$$O_O^{\times} \rightleftharpoons \frac{1}{2}\, O_2 + V_O^{\cdot\cdot} + 2\, e' \tag{2.3}$$

$$\frac{1}{2}\, O_2 \rightleftharpoons O_O^{\times} + V_M^{''} + 2\, h^{\cdot} \tag{2.4}$$

$$[e'] = K_{e^-}^{\frac{1}{2}} \cdot [V_O^{\cdot\cdot}]^{-\frac{1}{2}} \cdot p_{O_2}^{-\frac{1}{4}} \tag{2.5}$$

$$[h^{\cdot}] = K_O^{\frac{1}{2}} \cdot [V_M^{''}]^{-\frac{1}{2}} \cdot p_{O_2}^{\frac{1}{4}} \tag{2.6}$$

Together with the mass action laws for the electron/hole excitation (Eq. (2.7) and (2.8)), the Schottky disorder equilibrium and the charge balance, these result in a system of equations, which can be solved to give the defect concentrations as a function of p_{O_2} (see Figure 2.6)[21],[26],[27]. Three different regimes can be distinguished:

$$[e'] = 2\, [V_O^{\cdot\cdot}] \tag{2.7}$$

$$[V_O^{\cdot\cdot}] = (\frac{1}{4} \cdot K)^{\frac{1}{3}} \cdot p_{O_2}^{-\frac{1}{6}} \tag{2.8}$$

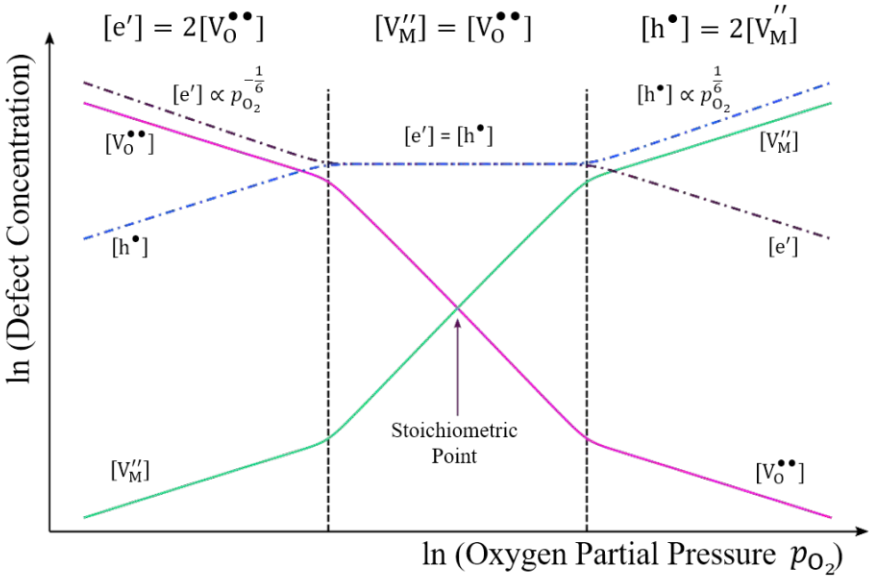

Figure 2.6: Schematic Brouwer diagram

These considerations describe only the equilibrium state; the kinetics of the oxygen incorporation, however, depend not only on the surrounding gas atmosphere, but also on other parameters and properties such as temperature, structure, incorporation resistance, and many more[28]–[30]. The surface exchange coefficient k^σ describes the number of oxygen atoms that are incorporated and removed per surface area and time, and in electrochemical terms, it directly translates to the oxygen exchange resistance (Eq. (2.9)).

$$k^\sigma = \frac{k_B \cdot T}{4 \cdot e^2 \cdot R_S \cdot c_O} \tag{2.9}$$

The incorporation resistance R_S is the resistance the oxygen experiences between the adsorption and incorporation site. The following charge transfer in the material happens via diffusion characterized by the diffusion coefficient D^σ. D^σ specifies how many oxygen ions diffuse through an area per time (Eq. (2.10)). Like k^σ, the diffusion coefficient is dependent on the temperature T, the Boltzmann constant k_B, the elemental charge e, the oxygen site concentration c_O and additionally on the ionic conductivity σ_{ion}.

$$D^{\sigma} = \frac{\sigma_{ion} \cdot k_B \cdot T}{4 \cdot e^2 \cdot c_O} \tag{2.10}$$

The ratio between the diffusion coefficient D^{σ} and the surface exchange coefficient k^{σ} gives the critical length L_C, that describes the distance, at which transport and incorporation resistance are equal (Eq. (2.11)).

$$L_C = \frac{D^{\sigma}}{k^{\sigma}} \hat{=} R_T = R_S \tag{2.11}$$

2.3 Chemical Capacitance

MIEC oxides have two different charge carriers, oxygen vacancies or interstitials for their ionic conductivity and electrons or electron holes for the electric conductivity. In contrast to the electrical capacitance, which is an increase of charge with the electrical potential, the chemical capacitance is defined as the increase of matter concentration with a varying chemical potential[31],[32]. When applying this concept to mixed ion-electron conducting oxides it is a measure of the readiness to change their stoichiometry as a result of a change in oxygen chemical potential and furthermore gives important information about the defect chemistry of the material[33]. The chemical capacitance of an oxide is defined in Eq. (2.12).

$$C_{chem} = 4 \cdot F^2 V n^0 \cdot \left(\frac{\partial \mu_O}{\partial c_O}\right)^{-1} \tag{2.12}$$

In it, F is Faraday's constant, V the sample volume, n^0 the absolute concentration of oxygen sites, μ_O the oxygen chemical potential and c_O the normalized oxygen concentration. The latter, c_O, is directly related to the non-stoichiometry δ of the material $ABO_{3-\delta}$ and the oxygen chemical potential is given by the chemical potential of oxide ions and electrons (Eq. (2.13)).

$$\mu_O = \mu_{O^{2-}} - 2\mu_{e^-} \tag{2.13}$$

Furthermore, the oxygen chemical potential can also be written as:

$$\mu_O = -\mu_V + 2\, z_{eon}\, \mu_{eon} \tag{2.14}$$

in which oxygen vacancies (V) are the dominating ionic defects and either electrons (e) or holes (h) the electronic defects. eon thus stands for either electrons e or holes h with z_eon being the charge number. The variation of the oxygen concentration and oxygen vacancies must be balanced and is given by

$$dc_O = -dc_V \tag{2.15}$$

and the local charge neutrality by

$$dc_{eon} = -2\, z_{eon}\, dc_V = 2\, z_{eon}\, dc_O \tag{2.16}$$

When differentiating Eq. (2.14) in respect to c_O and combining it with Eq. (2.15) and Eq. (2.16) we get:

$$\frac{\partial \mu_O}{\partial c_O} = -\frac{\partial \mu_V}{\partial c_O} + 2\, z_{eon}\, \frac{\partial \mu_{eon}}{\partial c_O} = \frac{\partial \mu_V}{\partial c_V} + 4\, \frac{\partial \mu_{eon}}{\partial c_{eon}} \tag{2.17}$$

When assuming that both ionic and electronic defects d are diluted, the chemical potential is:

$$\mu_d = \mu_d^0 + RT \cdot ln(c_d) \tag{2.18}$$

with c_d being the defect concentration n_d normalized over n^0, R the universal gas constant and T the temperature:

$$c_d = \frac{n_d}{n^0} \tag{2.19}$$

With Eq. (2.12), (2.18) and (2.17) an expression for C_{chem} can be obtained which shows its dependence on the defect concentrations:

$$C_{chem} = \frac{4F^2Vn^0}{RT}\left(\frac{1}{c_V} + \frac{4}{c_{eon}}\right)^{-1} = \frac{F^2V}{RT} \cdot \frac{1}{\left(\frac{1}{4n_V} + \frac{1}{n_{eon}}\right)} \tag{2.20}$$

However, often there is a significant difference in the ionic and electronic defect concentrations. In these cases, the chemical capacitance is determined by the minority charge carrier concentration n_{min}. Taking this into account, Eq. (2.20) can be simplified, which gives:[33]

$$C_{chem} \approx \frac{F^2V}{RT} z_{min}^2 n_{min} \tag{2.21}$$

2.4 Oxygen Ion Batteries (OIB)

2.4.1 Idea and Working Priciple

In principle, the ability of some MIEC's to change their oxygen stoichiometry, depending on the oxygen chemical potential, also gives them the ability to not only conduct ions, but also to store formally neutral oxygen in it's structure, by occupying oxygen vacancy sites and creating electron holes in their stead. In EIS measurements, this changeable oxygen stoichiometry manifests as the chemical capacitance. To get the MIEC to display battery-like behaviour, it is important that the oxygen exchange with the atmosphere is inhibited, such that the electrical energy can be stored chemically by changing the oxygen content of the electrode. When oxygen is stored in the MIEC, the oxidation states of the oxide material components change (meaning the oxide is either oxidized or reduced) and it acts as an oxide ion insertion electrode. In theory this oxygen insertion and removal works with the same principle as in a common Lithium Ion Battery (LIB), with the difference, that instead of the lithium stoichiometry, the oxygen stoichiometry of the material changes[10]. Figure 2.7 shows a comparison and the similarities between the working principle of a LIB and an OIB.

The half cell potential of either cathode or anode for OIB's can be determined from the materials reducibility. The reducibility of an oxide is it's oxygen chemical potential for the shift between electronic to ionic defects, as the majority defect. For an acceptor-doped MIEC like LSF, this would be the transition from holes (electronic) to oxygen vacancies (ionic). The chemical capacitance is at a maximum at this point and when calculating the charge-voltage curve, it shows itself as a charge plateau for a range of potentials. Combining materials with

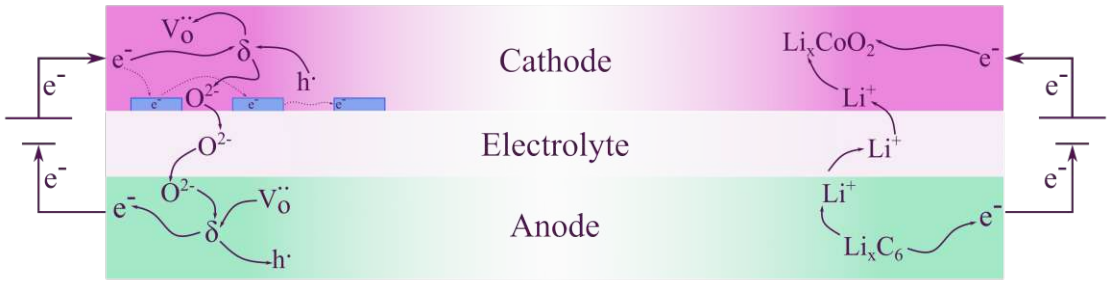

Figure 2.7: Comparison and similarities between the working principle of a LIB and an OIB. Image adapted from[10].

different half cell potentials and an electronically isolating electrolyte between them can thus create an OIB in which oxygen ions and electrons are transported between the two electrodes. When using a fully solid cell, the working temperatures for such batteries ranges from 350 - 600 °C and so far capacities of around 120 mA h cm^{-3} have been achieved[34].

2.4.2 Comparison with other Battery Types

When comparing oxygen ion batteries to other battery types, like lithium ion, sodium sulphur, ZEBRA or redox-flow batteries, one of its biggest advantages is, that it consists of only solid, non-flammable oxides, which reduces the risk of device failure through overheating and self-ignition. When compared to batteries that use metal ions, like lithium ion batteries, OIB's also don't pose a risk for dendrite formation and they also don't rely on the usage of flammable liquid electrolytes. Furthermore, possible electrode materials can be made from mostly abundant and safe elements (such as Fe, Ti, Mn, Cr, Ca, etc.) and don't have to rely on critical elements such as lithium or cobalt. Due to their high working temperature, possible applications are balancing systems for renewable energy sources, transformer stations or other stationary applications in high temperature environments[10].

2.5 Electrical Impedance Spectroscopy (EIS)

EIS is a non-destructive characterisation technique that measures the electrical impedance of a material over a range of frequencies. It gives information about the electrical properties of the measured material, like the resistance, capacitance, and inductance. It can also be used to investigate the physical and chemical processes that occur at the material-electrolyte or

electrolyte-electrode interface[35]. It is widely used for material characterisation in many fields, like energy conversion and storage technologies[36], corrosion studies[37], semiconductor science[38] or chemical and bio sensing[39].

The electrical impedance is the ratio of an applied voltage to the resulting current. It is a complex parameter that has a magnitude and phase. A substantial element of electrical impedance measurements is the fitting of the spectrum to an equivalent circuit with common passive components such as resistors, capacitors or inductors[40],[41].

2.5.1 Working Principle

The general working principle of electrical impedance spectroscopy is the frequency dependent measurement of the current response to an applied, alternating voltage, which results in the complex AC resistance, the impedance. For linear systems, and sine shaped applied voltages, the responding current also follows a sine wave, shifted by the phase angle ϕ. A phase angle of 0° can be interpreted as purely real, ohmic behaviour, and phase angles of −90 and +90 represent inductive and capacitive behaviour respectively. The impedance itself can be stated as the ration of the voltage amplitude ($U(\omega)$) divided by the current amplitude ($I(\omega)$) times a phase factor (Eq. (2.22)).

$$Z(\omega) = \frac{U(\omega)}{I(\omega)} \cdot e^{i \cdot \phi(\omega)} \tag{2.22}$$

To calculate the total impedance and characterize equivalent circuits including resistive, capacitive and inductive elements in serial and parallel connections, Kirchhoff's laws can be applied. Kirchhoff states that the total impedance of elements in series is equal to the sum of the individual impedances (Eq. (2.23)) and the total impedance of parallel elements is equal to one over the sum of the reciprocal impedances (Eq. (2.24).

$$Z_{1-2} = Z_1 + Z_2 \tag{2.23}$$

$$Z_{1||2} = \frac{1}{\frac{1}{Z_1} + \frac{1}{Z_2}} \tag{2.24}$$

The impedances Z of the three most common passive components (resistors Z_{res}, capacitors Z_{cap} and inductors Z_{ind} are given in Eq. (2.25), (2.26) and (2.27) respectively. Resistive effects can be interpreted as the movement of charge carriers or as electrochemical reactions. Capacitive effects can be attributed to a standard, dielectric capacitance, the charging of the double layer or the chemical capacitance. Inductive effects are only of minor importance in regards to electrochemistry and the application of EIS in energy storage technologies.

$$Z_{res} = R \tag{2.25}$$

$$Z_{cap} = \frac{1}{i \cdot \omega \cdot C} \tag{2.26}$$

$$Z_{ind} = i \cdot \omega \cdot L \tag{2.27}$$

However due to inhomogeneities, the behaviour of the capacitance is rarely ideal. This non-ideal behaviour can be considered by a Constant Phase Element (CPE) instead of a regular capacitor in the equivalent circuit. Eq. (2.28) gives the impedance of a CPE and (2.29) its capacitance. T is the CPE parameter and the exponent P is used to quantify the non-ideal behaviour of the element. If $P = 1$, then the CPE is an ideal capacitor.

$$Z_{CPE} = \frac{1}{(i\omega)^P \cdot T} \tag{2.28}$$

$$C_{CPE} = (R^{1-P} \cdot T)^{\frac{1}{P}} \tag{2.29}$$

2.5.2 Impedance Spectra

The frequency dependent impedance can be visualized in various plots. All plots contain the same information, but emphasize different aspects and characteristics of the impedance to enable interpretation specific to the purpose of the measurement. The two most common ones for electrochemical purposes are[42]:

- **Nyquist Plot** - The imaginary and real part of the impedance are plotted against each other. Each data point has a different frequency, which decreases from left to right. This specific plot displays an R||C element, in which case the apex of the semi-circle represents the relaxation frequency ω_p. (Eq. (2.30); Fig. 2.8)

$$\omega_p = \frac{1}{RC} = \frac{1}{\tau_p} \tag{2.30}$$

τ_p is the relaxation time, which is the time needed until a system responds to a disturbance with a physical process.

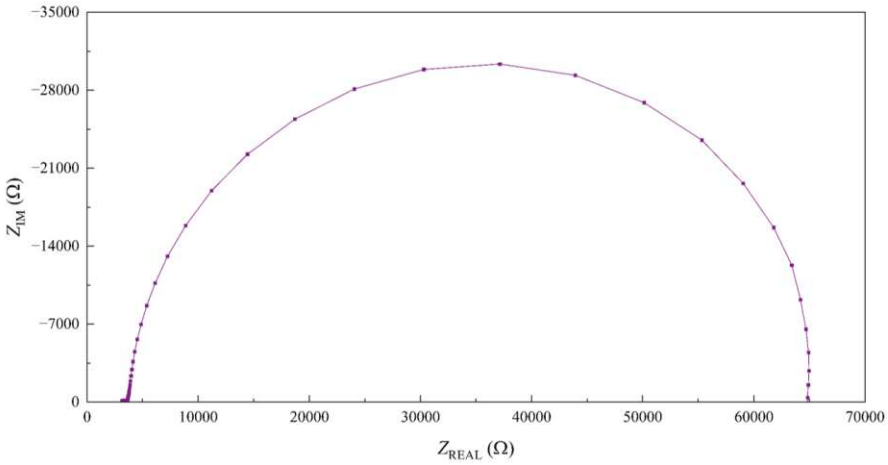

Figure 2.8: Example of a Nyquist plot

- **Bode Plot** - Bode Plots are a combination of two graphs. One describes the magnitude and the other the phase angle of the impedance as a function of the logarithmic frequency. (Fig. 2.9)

2.5.3 Equivalent Circuits

To quantitatively analyze measured impedance spectra, they need to be fitted with a suitable equivalent circuit. Jamnik and Maier[43] developed a basic model circuit (Figure 2.10 a)) for MIEC's, which can be simplified and adapted to the relevant materials. In our specific case, the model circuit reflects a three point measurement of a MIEC on a YSZ electrolyte, with a reference electrode in close proximity. Therefore the ionic transport resistance through the YSZ and the counter electrode can be neglected. For two point measurements, the ionic transport

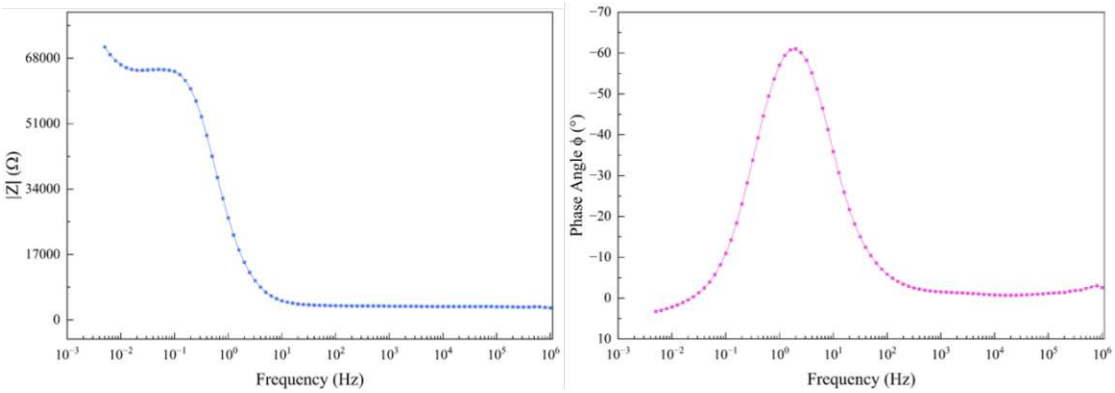

Figure 2.9: Example of a Bode plot

resistance through the electrolyte also has to be considered, since it contributes to the total impedance as well, and is added in the circuit as a single, serial resistance R_{YSZ}. Since MIEC oxides often have high electronic conductivity, the electronic resistors R_{eon} can be neglected and the electronic rail short circuited. Additionally, when working with a thin film geometry and assuming sufficient ionic conductivity of the MIEC, the entire electode reaction is limited by the oxygen surface exchange resistance R_S, which is in parallel with the surface capacitance $C_{s,ion}$. Therefore, the ionic transport resistances R_{ion} can be neglected as well and all the parallel chemical capacitors C_{chem} can be combined into a single chemical capacitance C_{chem}. The remaining circuit elements $R_{MIEC|YSZ}$ and $C_{MIEC|YSZ}$ are the ionic transfer resistance and capacitance, that occur due to the electron blockage at the MIEC|YSZ interface and the ionic transport resistance through the electrolyte R_{YSZ}. The model equivalent circuit with all the simplifications applied is shown in Figure 2.10 b). Depending on how much larger C_{chem} is, compared to the parallel surface capacitance $C_{s,ion}$, $C_{s,ion}$ can also be neglected.

For a measurement setup with microelectrodes, the impedance of the counter electrode can often be completely neglected as well. This is because the surface of the counter electrode is much larger, which results in a very small impedance, when compared to the working electrode.

Current Collector

When an additional current collector is used to guarantee a high electronic conductivity, the simplified equivalent circuit from Figure 2.10 b) has to be adapted accordingly. The adaptations differ with weather the current collector is placed above or below the working electrode. Since

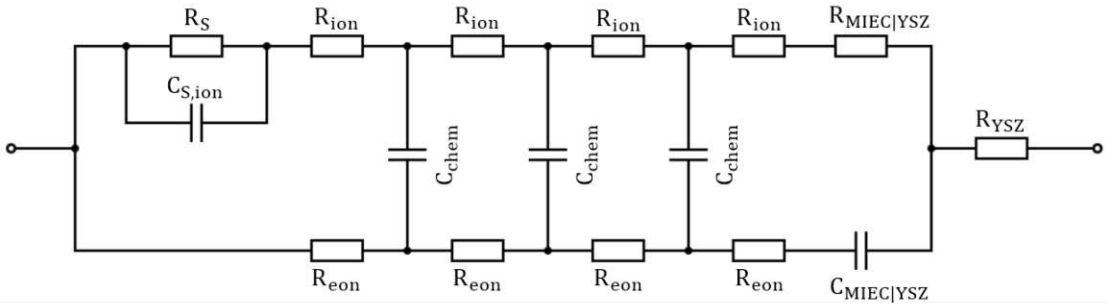

a) General model equivalent circuit

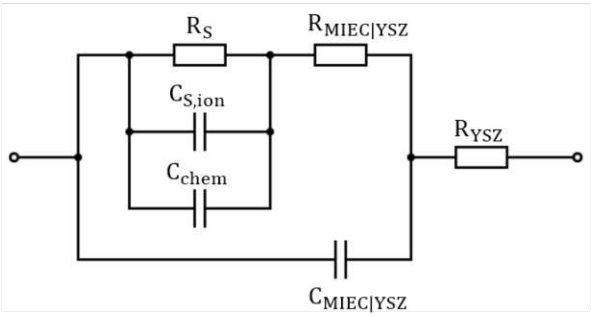

b) Simplified model equivalent circuit

Figure 2.10: a) General model equivalent circuit for a MIEC on a YSZ electrolyte and b) a simplified model equivalent circuit, assuming high electronic and ionic conductivity and the oxygen surface exchange as the limiting step

all measured samples have the current collector placed below the working electrode, only this case will be discussed[44]. A full model equivalent circuit with the current collector below the working electrode is shown in Figure 2.11.

- **Reducing Conditions** - In this case, the lateral ionic tansport resistance R_{ion} is low, compared to the surface resistance R_S, and therefore both circuit sides (1 and 2) contribute to the surface exchange $C_{MIEC|YSZ}$ and chemical capacitance C_{chem}. The electronic conductivity is low, which causes a Warburg slope feature in the high frequency domain of the impedance spectrum. This can be described with a CPE element. The low frequency domain is dominated by the surface exchange resistance parallel to the chemical capacitance C_{chem}. The simplified model circuit for reducing conditions is shown in Figure 2.11 b)

- **Oxidizing Conditions** In this case, the lateral ionic transport resistance R_{ion} is high, compared to the surface resistance. Therefore the left branch (1) in Figure 2.11 a) is blocked by this resistance and does not contribute to the surface exchange and chemical

capacitances. The electronic conductivity is high and can therefore be neglected in the right circuit (2). The simplified model circuit for oxidizing conditions can be seen in Figure 2.11 c).

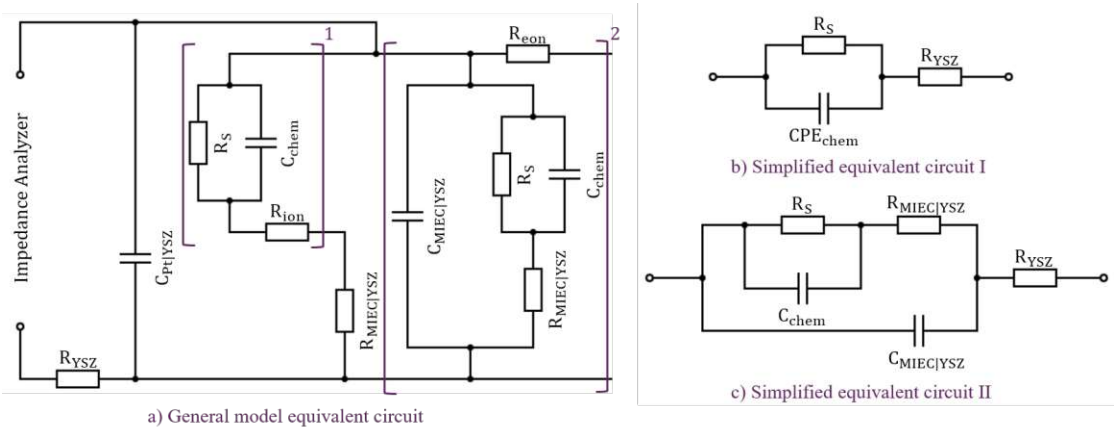

Figure 2.11: a) General model equivalent circuit for MIEC on a YSZ electrolyte, with the current collector beneath the working electrode b) a simplified model equivalent circuit for reducing conditions and c) a simplified model equivalent circuit for oxidizing conditions

2.5.4 Measurements with DC bias

As previously mentioned, an electrochemical reaction reaction is driven back and forth around it's equilibrium by applying an alternating voltage. By applying an additional DC bias voltage U_{DC}, the equilibrium is disturbed. This causes an additional net reaction rate and DC current I_{DC}. Figure 2.12 shows the current-voltage curve for an arbitrary electrochemical reaction with two investigated ranges measured by impedance spectroscopy with and without an applied DC bias.

To understand how an applied DC bias affects the measured cell, it is necessary to take the electrochemical potentials of the MIEC Counter Electrode (CE) and Working Electrode (WE) and the oxygen ion conducting solid electrolyte into account. The electrochemical potential of oxygen $\tilde{\mu}_O$ in the electrode is defined as the electrochemical potential of the electrons $\tilde{\mu}_e$ subtracted from the electrochemical potential of the oxygen ions $\tilde{\mu}_{O^{2-}}$ (Eq. (2.31)).

$$\tilde{\mu}_O = \tilde{\mu}_{O^{2-}} - 2 \cdot \tilde{\mu}_e \tag{2.31}$$

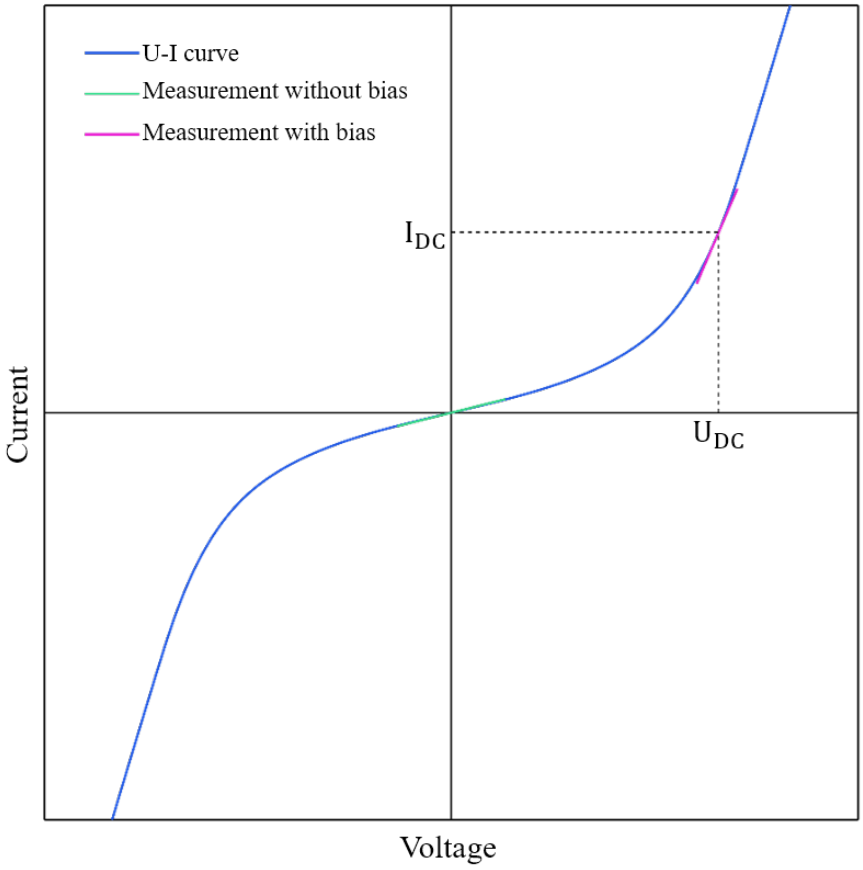

Figure 2.12: Current-Voltage curve of an arbitrary electrochemical reaction (blue) with two investigated ranges without (teal) and with (pink) bias.

Since an ideal, reversible CE is always in equilibrium with the gas phase, it's chemical potentials of oxygen, oxygen ions, and electrons is fixed, regardless of the applied voltage. This is not the case for the WE and results in a difference in potentials between the WE and CE, when a DC bias is applied (Eq. (2.32)

$$\Delta\tilde{\mu}_e = F \cdot U_{DC} \tag{2.32}$$

Since both electrodes possess a high electronic conductivity, it can be assumed, that the electrochemical potential of the electrons $\tilde{\mu}_e$ is constant within them. This potential difference between the electrodes and the finite ionic conductivity of the electrolyte result in a change in the electrochemical potential of the oxygen ions across the thickness of the electrolyte and is expressed by:

$$\Delta\tilde{\mu}_{O^{2-}} = 2 \cdot F\eta_{YSZ} \tag{2.33}$$

With Faraday's constant F and the Ohmic overpotential η_{YSZ}, which is the loss across the electrolyte and defined in Eq. (2.34) by the DC current I_{DC} and the ionic transport resistance R_{YSZ}.

$$\eta_{YSZ} = I_{DC} \cdot R_{YSZ} \tag{2.34}$$

Due to the electrochemical potential changes across the cell, there's also a change in the oxygen electrochemical potential and Eq. (2.31) can be rewritten as:

$$\delta\tilde{\mu}_O = \delta\tilde{\mu}_{O^{2-}} - 2 \cdot \delta\tilde{\mu}_e \tag{2.35}$$

Consequently, the WE is not in equilibrium with the oxygen partial pressure of the gas phase. This described electrochemical potential difference is the overpotential of the working electrode η_{WE} and a part of the applied DC voltage. Assuming the CE is lossless, n_{WE} is defined as:

$$\eta_{WE} = U_{DC} - \eta_{YSZ} = U_{DC} - I_{DC} \cdot R_{YSZ} \tag{2.36}$$

In accordance with the Nernst equation, the overpotential can be converted to an oxygen partial pressure (Eq. (2.37)) and an equivalent oxygen partial pressure p_{eq} can be defined (Eq. (2.38)), with the actual oxygen partial pressure p_{act}.

$$\eta_{WE} = \frac{RT}{4F} \cdot ln(\frac{p_{eq}}{p_{act}}) \tag{2.37}$$

$$p_{eq} = p_{act} \cdot e^{\frac{\eta_{WE} 4F}{RT}} \tag{2.38}$$

Therefore the the defect chemical state of the working electrode is defined by the actual atmospheric oxygen partial pressure p_{act} and the applied voltage bias V_{DC}.

3 Experimental

3.1 List of Chemicals

All chemicals that were required for either the synthesis, measurements or sample preparations are listed in Table 3.1.

Table 3.1: Overview of the used chemicals

Chemical Formula	Name	Purity	Supplier
C_2H_5OH	Ethanol	99.8	Sigma Aldrich
Extran	Extran	-	Sigma Aldrich
Fe_2O_3	Iron(II,III) Oxide	99.99%	Alpha Aesar
$SrCO_3$	Strontium Carbonate	99.99%	Sigma Aldrich
La_2O_3	Lanthanum Oxide	99.99%	Sigma Aldrich
$MnCO_3$	Manganese (II) Carbonate	99.98%	Alpha Aesar
$Cr(NO_3)_3$ /*cdot* $9H_2O$	Chromium (III) Nitrate Nonahydrate	99.99%	Alpha Aesar
HNO_3	Nitric Acid	99.99%	Sigma Aldrich
$C_6H_8O_7$	Citric Acid	99.5%	Sigma Aldrich
Y_2O_3	Yttrium Oxide	99.99%	Sigma Aldrich
$BaCO_3$	Barium Carbonate	99.98%	Sigma Aldrich
Co_3O_4	Cobalt(II,III) Oxide	99.5%	Sigma Aldrich
$C_2H_6O_2$	Ethylene Glycole	99.8%	Sigma Aldrich
-	ma-N 1420 Photoresist	-	MicroResist Technology
-	ma-D 533 Developer	-	Microresist Technologies

3.2 Sample Preparation

3.2.1 Methods

Metal Sputtering

For the deposition of the current collector grid, a MED 020 Coating System (BAL-TEC, Germany) was used to sputter Pt and Ti on the YSZ sample. The samples were put into a vacuum chamber. It was evacuated to 10^{-5} mbar and then adjusted to the desired Ar pressure. First a 10 nm Ti layer was sputtered onto the sample. Then a 100 nm Pt layer was sputtered over the Ti layer. Afterwards the samples were cleaned again with ethanol. The exact parameters for the sputter process can be found in Table 3.2

Table 3.2: Metal Sputtering Parameters

	Titanium	Platinum
Sputter time (s)	55	161
Argon pressure (mbar)	$7 \cdot 10^{-3}$	$2 \cdot 10^{-2}$
Sputter current (mA)	100	100
Target distance (cm)	6	6

Pulsed Laser Deposition (PLD)

Deposition of the electrode materials onto the YSZ electrolyte was done in a vacuum chamber using a Compex Pro 201F KrF excimer laser (Coherent, Germany) with a wavelenght of 248 nm. The samples were cleaned with ethanol and then put into the sample holder. Before the depostion, the chamber was evacuated to 10^{-5} mbar and then the oxygen partial pressure was adjusted. The targed was pre-ablated for 100 pulses with a pulse rate of 2 Hz, before the samples were then heated to the desired deposition temperature. After reaching steady values for the temperature and the pressure, the material was deposited with a pulse rate of 10 Hz with an energy between 350 mJ and 450 mJ per pulse. After the deposition was finished, the samples were cooled with a cooling rate of 15 °C per minute and after removing them from the chamber, they were cleaned with ethanol. The exact depostion parameters for each material are summarized in Table 3.6 and Table 3.7.

Photolithography

All photolithography steps were done in a dust-free cleanroom. Before the coating of the samples with a photoresist paint, they were cleaned with ethanol and dried with nitrogen gas. The samples were then coated with 2 x 100 µL of ma-N 1420 Photoresist Laquer (MicroResist Technology, Germany) on a SCC-200 spincoater (KLM, Germany). The samples were then heated on a hot plate to evaporate excess solvent and then exposed to UV light (350 W, USHIO 350DP Hg, Ushio, Japan) through a patterned shadow mask for either the grid (35 x 35 µm squares / 15 µm spacing) or the circular microelectrodes (d = 50 - 300 µm). The parts of the photoresist, that were not exposed to the UV light were removed with the ma-D 533/s developer solution (Microresist Technologies, Germany) and then cleaned with de-ionized water. The parameters for all photolithography steps can be found in Table 3.3.

Table 3.3: Photolithography parameters per sample

Photoresist (µL)	200
Temperature (°C)	450
Spincoater speed (rpm)	75
Spincoater duration (s)	45
Heating temperature (°C)	100
Heating duration (min)	5
UV light exposure (s)	35 to 70
Developing time (s)	60 to 120

Ion Beam Etching

The areas of the sample not protected by photoresist were then removed with an ion beam etcher (ionEtch Sputter Gun, tectra GmbH, Germany). The samples were placed on a thin film of thermally conducting paste in a vacuum chamber, which was then evacuated to 10^{-5} mbar. The etching was then carried out using an Ar plasma. After removing the samples from the ion beam etcher, a multimeter was used to see if the etching process is complete. The samples were then cleaned with ethanol to remove the remaining photoresist. The exact parameters used for the ion beam etching can be found in Table 3.4. For the first two created samples (with LSF and LSCrMn as the working electrode materials) no thermally conducting paste was used and it was not possible to remove all of the remaining photoresist. Other than just wiping it away with ethanol, the samples were also soaked in ethanol, acetone and isopropanol respectively

for 60 minutes in an ultrasonic bath and then another 24 h outside of it, each, but there was still some remaining photoresist. A probable cause for this could be a reaction between the photoresist and the working electrode material and the YSZ due to the long duration at elevated temperatures caused by the etching process. Figure 3.1 shows the difference between two samples with LSCrMn as the working electrode material. On the sample in 3.1 a) it no thermally conducting paste was used for the ion beam etching process and some photoresist remained on the surface, whereas Figure 3.1 b) shows a sample for which thermally conducting paste was used and all photoresist could be removed by wiping it away with ethanol and a clean room wipe.

Table 3.4: Ion beam etching parameters

Argon pressure (mbar)	$4{\cdot}10^{-4}$
Plasma current (mA)	100
Etching time (min)	75 to 100
Beam voltage (kV)	500

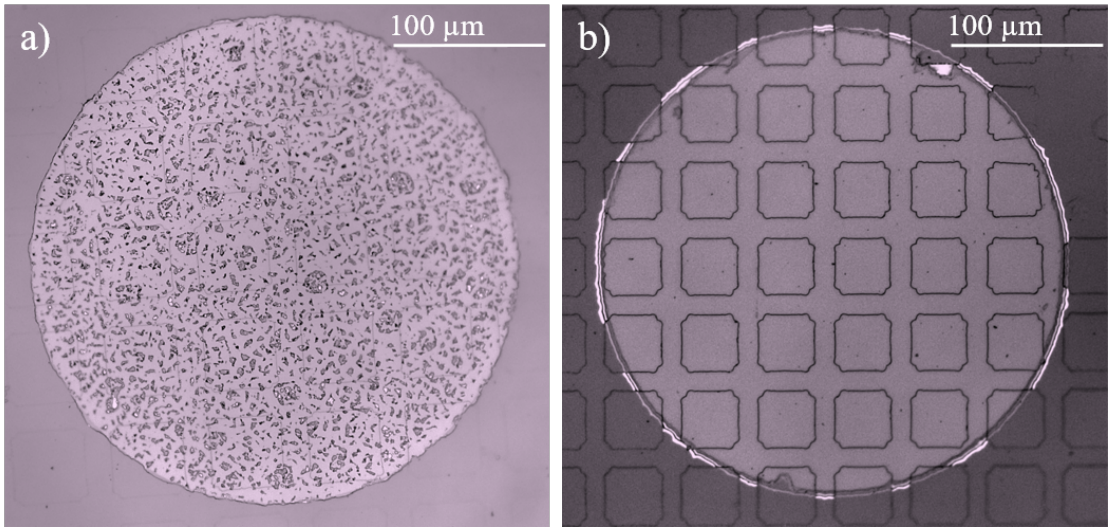

Figure 3.1: Picture of a 250 µm microelectrode with the visible Pt/Ti lattice underneath

3.2.2 Material Synthesis

$La_{0.6}Sr_{0.4}FeO_{3-\delta}$ - Lanthanum Strontium Ferrite

The used LSF64 target for the PLD was synthesized by the Pechini[45] method. Stoichiometric amounts of La_2O_3, $SrCO_3$ and Fe_2O_3 were weighed and then dissolved in HNO_3 and citric acid was added in a 1:1.1 molar ratio of the used metal cations. The solution was then concentrated to form a gel and further heated until it self-ignited. After cool down, the obtained powder was calcinated for 3 h at 900 °C and then annealed for 5 h at 1200 °C. In a final step, the powder was grinded, pressed into pellets using a cold isostatic press and then sintered at 1250 °C for 5 h[46].

$La_{0.5}Sr_{0.5}Cr_{0.2}Mn_{0.8}O_{3-\delta}$ - Lanthanum Strontium Chromium Manganite

The used LSCrMn82 target for the PLD was synthesized by a modified Pechini[45] method. Stoichiometric amounts of La_2O_3, $SrCO_3$, $MnCO_3$ and $Cr(NO_3)_3 \cdot 9\,H_2O$ were used and dissolved in nitric acid and citric acid. More citric acid was then added in a 1:1 molar ratio of the metal cations. The solution was then concentrated to form a gel and further heated with a Bunsen Burner to ignite it. The received powder was then calcinated at 800 °C for 4 h, pressed into pellets using a cold isostatic press and the pellets were then sintered at 1300 °C for 7 h[47].

$Gd{:}CeO_2$ - Gadolinium doped Ceria

GDC10 powder was obtained from Treibacher Group AG, Austria. The powder was then cold isostatically pressed into pellets and sintered at 1300 °C for 7 h.

$La_2NiO_{4+\delta}$ - Lanthanum Nickel Oxide

The sample with LNO as the working electrode was made at the Laboratoire des Matériaux et du Génie Physique in Grenoble. The sample used a 10 x 10 x 0.5 YSZ single crystal as the electrolyte and also used a Pt/Ti grid as a current collector underneath the working electrode film. The LNO thin film was then grown by Pulsed-Injection Metalorganic Chemical Vapor Deposition (PI-MOCVD) as described by Stangl et. al.[48].

$YBaCo_4O_{7-\delta}$ - Yttrium Barium Cobaltate

The used $YBaCo_4O_7$ target for the PLD was synthesized by a solid state reaction described in reference[49]. Starting point are stoichiometric amounts of Y_2O_2, $BaCO_3$ and Co_3O_4. The balanced reaction equation can be seen in Equation (3.1) and the exact amounts used to synthesize 12 g of product can be found in Table 3.5. The first step was to grind and mix all powders together. The powder was then unixaially pressed into pellets at 15 kbar for 1 minute and then sintered in the oven at 1000 °C for 10 h. For the heat treatment, a corundum crucible was used and additional $YBaCo_4O_7$ powder was used as a powder bed. The pellets were then ground up, pressed and sintered again. This time at 1200 °C for 24 h. The heating rate for both steps was 5 °C min^{-1}. The last step was to sand the surface of the pellets by hand to roughly smooth out any irregularities. The samples were examined via XRD measurements to determine phase purity.

$$6\,Y_2O_3 + 12\,BaCO_3 + 16\,Co_3O_4 \longrightarrow 12\,YBaCo_4O_7 + 12\,CO_2\uparrow + 5\,O_2\uparrow \tag{3.1}$$

Table 3.5: Components and amounts used for the $YBaCo_4O_7$ synthesis

Y_2O_2	4.72 g
$BaCO_3$	4.12 g
Co_3O_4	5.03 g

$SrTiO_3$ - Strontium Titanate

The STO target for the PLD was synthesized via a solid state reaction starting from $SrCO_3$ and TiO_2. Stoichiometric amounts were weighed and mixed for about 45 minutes in a mortar and then pressed and caclinated for 2 h at 1000 °C. The pellets were then milled again, pressed with a cold isostatic press and then sintered at 1200 °C for 5 h in air[50].

$La_{0.6}Ca_{0.4}FeO_{3-\delta}$ - Lanthanum Calcium Ferrite

The used LSF target for the PLD was synthesized by a modified Pechini[45] method. Stoichiometric amounts of La_2O_3, $CaCO_3$ and Fe_2O_3 were used and dissolved in nitric acid and citric acid. More citric acid was then added in a 1:1 molar ratio of the metal cations. The solution

was then concentrated to form a gel and further heated with a Bunsen Burner to ignite it. The received powder was then calcinated at 800 °C for 5 h, pressed into pellets using a cold isostatic press and the pellets were then sintered at 1300 °C for 7 h[51].

3.2.3 Sample Architecture

YSZ Single Crystal Electrolyte

YSZ single crystals (MaTeck GmbH, Germany) were used as the base and electrolyte of the sample. For the LSF and LSCrMn samples, crystals that have been polished on both sides are used and for all other samples, single crystals that have been polished on only one side were used. The crystal lattice orientation of the samples is (100) and the dimensions are 10 mm x 10 mm x 0.5 mm. The samples were cleaned with Extran, ethanol and de-ionized water for 30 minutes each in a 50 °C ultra sonic bath. Afterwards they were annealed for 12h at 1200 °C in air and lastly wiped with ethanol again.

Counter Electrode

For all prepared samples, LSC was used as the counter electrode. A 300 nm layer was deposited on the non-polished side of each single crystal. The Pulsed Laser Deposition (PLD) parameters for depositing the LSC layer are depicted in Table 3.6

Table 3.6: PLD parameters for the deposition of LSC

Heating power (%)	35
Temperature (°C)	450
Number of pulses ()	18000
Frequency (Hz)	10
Time (min)	30
Pressure (mbar)	$4 \cdot 10^{-3}$
Target distance (cm)	6
Energy set (mJ)	400

Pt/Ti Current Collector Grid

All prepared samples have a current collector grid under between the YSZ single crystal and the working electrode layer. It consists of a 10 nm Platinum layer and a 100 nm Titan layer, which were sputtered on. Structuring of the grid was done by photo-lithography and ion beam etching.

Working Electrode

To create the working elctrodes, a layer of the material was depositioned on top of the current collector grid. The layer thickness ranges between 150 and 300 nm and the exact PLD parameters vary between different materials and can be seen in Table 3.7. After depositioning the layer, a lithography mask with circles between 50 - 300 µm was used to create the shaped of the microelectrodes and any excess material was etched away.

The following materials were investigated for the usage as working electrodes:

- $La_{0.6}Sr_{0.4}FeO_{3-\delta}$ (LSF)
- $La_{0.5}Sr_{0.5}Cr_{0.2}Mn_{0.8}O_{3-\delta}$ (LSCrMn)
- Gd:CeO_2 (GDC)
- $YBaCo_4O_{7-\delta}$ ($YBCo_4O_7$)
- $La_2NiO_{4+\delta}$ (LNO)
- $SrTiO_3$ Strontium Titanate (STO)
- $La_{0.8}Ca_{0.2}FeO_{3-\delta}$ (LCF)

Completed Sample

Figure 3.2 shows a schematic image of a finished sample. The scale is not true to size, but was chosen to make every part of the sample well visible and distinguishable.

Table 3.7: PLD parameters for the deposition of different working electrode materials

	LSF	LSCrMn	GDC	$YBaCo_4O_7$	STO	LCF
Heating Power (%)	50	65	50	80	60	50
Temperature (°C)	600	700	650	800	650	600
Number of Pulses	18000	12000	6500	6000	13500	18000
Frequency (Hz)	10	10	10	5	10	10
Time (min)	30	20	11	20	22.5	30
Pressure (mbar)	$4{\cdot}10^{-2}$	$1.5{\cdot}10^{-2}$	$4{\cdot}10^{-2}$	$3{\cdot}10^{-1}$	$1.5{\cdot}10^{-1}$	$4{\cdot}10^{-2}$
Target Distance (cm)	6	6	6	6	6	6
Energy Set (mJ)	400	400	400	450	350	400

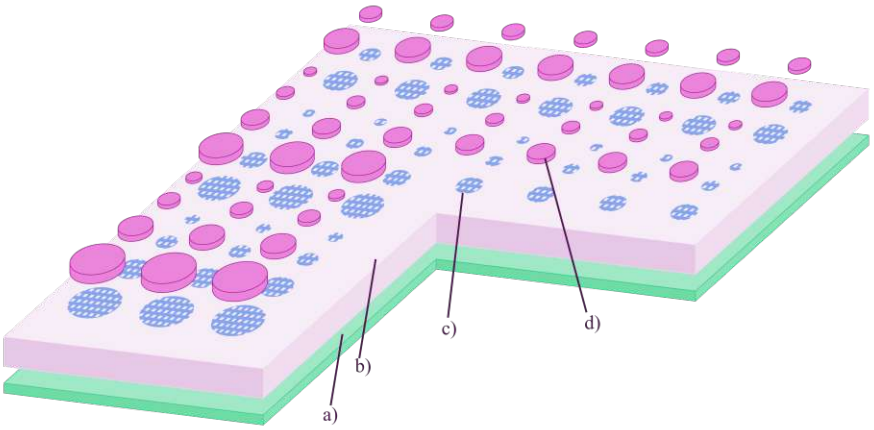

Figure 3.2: Schematic 3D sample architecture with a) the LSC counter electrode, b) the YSZ electrolyte c) the Pt/Ti current collector grid and d) the micro working electrodes in different sizes.

In Figure 3.3, a light microscope image of a single microelectrode can be seen. The measured diameter of the electrode was 249.64 µm and the Pt/Ti lattice was had a width of 12.38 µm, with the open spaces in between measuring 37.44 µm. The reason a very light imprint of the lattice can be seen on the blank single crystal, even though it was etched away, is, because it was slightly overetched, to make sure that all Pt/Ti remnants are removed so that an electric separation between the microelectrodes can be guaranteed.

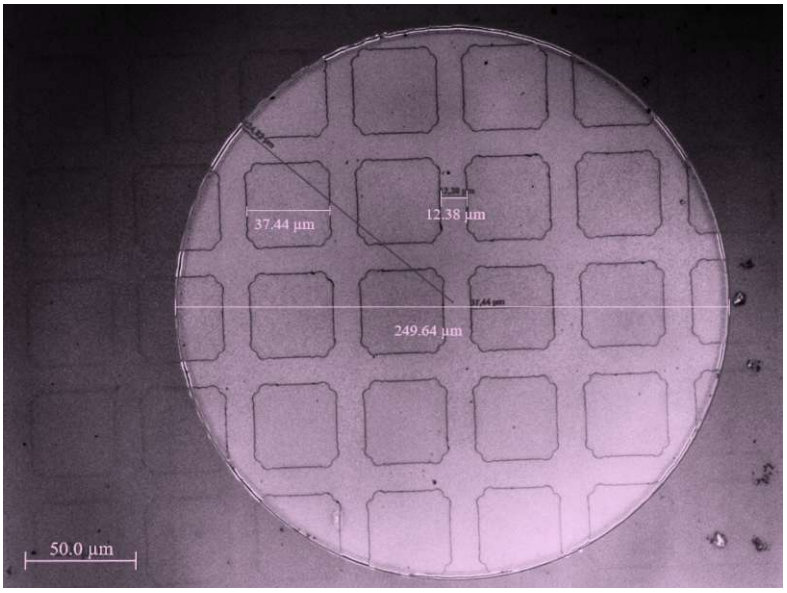

Figure 3.3: Picture of a 250 µm microelectrode with the visible Pt/Ti lattice underneath

Scanning Electrode Microscope (SEM)

Secondary Electron Microscope (SEM) images were taken at the USTEM - Elektronenmikroskop of the TU Wien on a Quanta 250 FEG (FEI, USA). Although all samples have some electric conductivity, a thin layer of gold was sputtered on to achieve an even conductivity and ensure good image results.

X-Ray Diffraction (XRD)

X-Ray Diffraction (XRD) measurements were done at the XRC - X-Ray Center. Bragg Brentano XRD measurements for the pressed $YBCo_4O_7$ target were carried out at the X'Pert MPDII (PANanalytical, United Kingdon) and Grazing Incidence Diffraction (GID) for the deposited $YBaCo_4O_7$ thin film on the single crystal with the Empyrean material diffractometer (PANalaytical, United Kingdom).

3.3 Electrochemical Characterization

For the electrical impedance measurements an Alpha-A High Performance Frequency Analyzer with an Electrical Test Station POT/GAL 30V/2A (Novocontrol Technologies GmbH & Co. KG, Germany) was used. The full measurement set-up for the electrical impedance measurements is shown in Figure 3.4 and a schematic close up of the inside of the furnace is shown in Figure 3.5. The sample was placed on the Pt sheet inside the furnace and one 300 µm microelectrode was connected via one of the Pt-Ir needles. The temperature inside the furnace was controlled by a Eurotherm 3216 (Eurotherm, Germany) temperature control system. The measurements were conducted either in a 1% oxygen in N_2 atmosphere or a wet H_2 atmosphere. The atmosphere was regulated with a GF40 Mass Flow Controller (Brooks Instrument, USA) and a ROD-4 Control Panel (GCE Group, Sweden). The outside of the system was cooled via a water cooling system. Due to their small size, the positioning of the needle to connect the microelectrodes was done with a movable micromanipulator equipped with a camera.

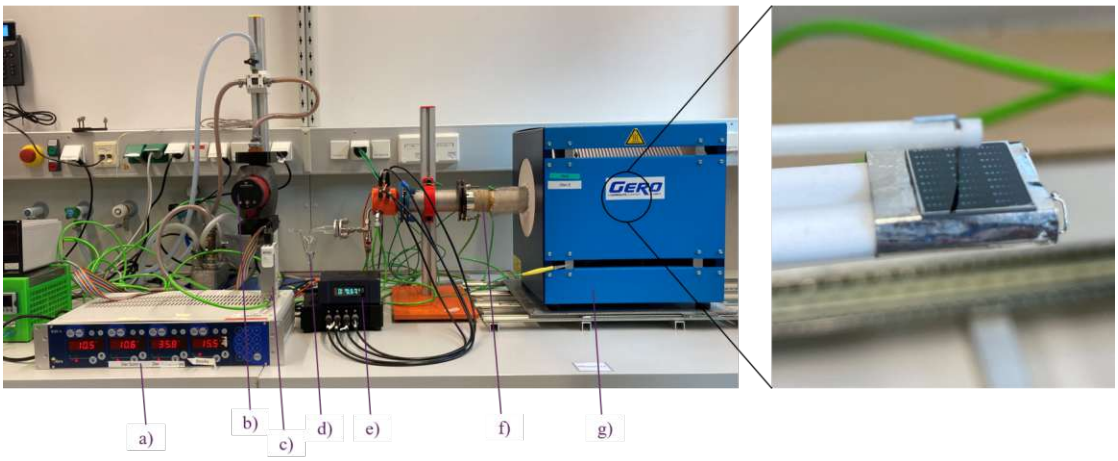

Figure 3.4: Photo of the full measurement set up and a close up of a connected microelectrode. a) ROD-4 Control panel, b) Water cooling system c) MFC d) Bubbler e) "Thermolino" temperature sensor f) Copper cooling tubes over furnace tube g) Furnace

The chosen atmosphere gas was bubbled through the chamber for at least 30 minutes prior to heating in order to avoid any reactions between the samples and possible contamination in the lab air at elevated temperatures. The impedance was measured in the frequency range of 1 MHz to 4 mHz with 10 data points per decade. For all measurements, a bias ranging from

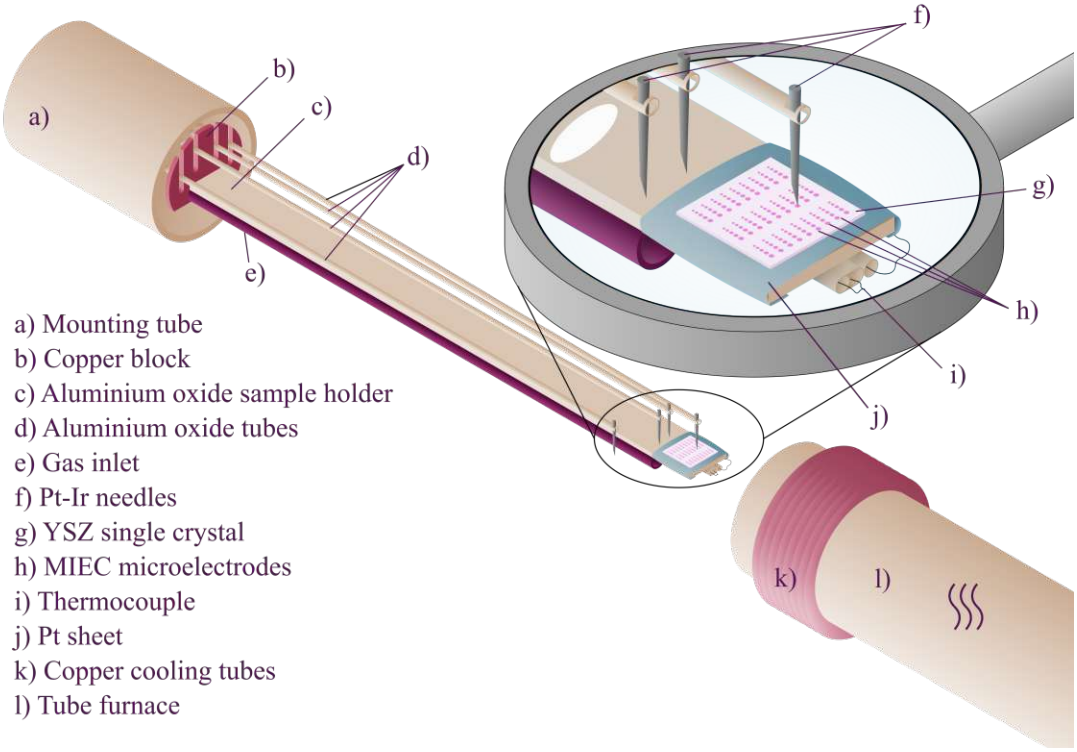

Figure 3.5: Schematic sketch of the central parts inside the furnace of the measurement-set up and a close up of a contacted sample. Image adapted with permission from the author[52].

0 to up to 2500 mV, with the exact value depending on the sample, was applied, with bias steps of either 50 or 100 mV. For each measurement, at least two cycles were measured at each temperature, alternating between cycles with increasing and decreasing bias steps.

The used measurement software to record the impedance spectra was JavaLab 1.41 and they were fitted in ZView 2. All calculations were done in Microsoft Excel, with scripts to import impedance data and calculate the mean current values (for the code see Appendix A), data graphs were created using Origin Lab 2023 and images were created in Inkscape.

4 Results and Discussion

4.1 Thin Film Morphology

The morphology of the thin film samples was characterized with a light microscope and with a SEM. The optical microscope was used to measure the dimensions of the current collector grid and the microelectrodes and see if the etching process was complete. The SEM was used to compare how the thin films grow on the blank YSZ electrolyte and the Pt/Ti current collector grid. Although thickness measurements for all thin films were attempted, only a cross section of the GDC thin film was possible, since, due to the thin nature of the film, they prove to be quite difficult to focus on. For the calculation of the C_{chem} values, the height calculated from the Quartz Crystal Microbalance (QCM) inside PLD was used. For $YBaCo_4O_7$ both, thin film and PLD target were also characterized with XRD and grazing incidence measurements to ensure phase purity.

The slight outline of the current collector grid, which is visible on most light microscope images on the YSZ electrode, is not a real current collector, but a slight indent in the YSZ surface itself. This is because when etching the current collector, it was slightly overetched to guarantee the removal of all material. The same principle was applied to the etching process of the microelectrodes, however, this is not visible. How smooth or rough a material grows on the electrolyte or the grid depends on the material itself and its crystal structure compared to the medium its growing onto. Usually, if the crystal structures are similar to each other, the surface will be smoother with less imperfections and grains. The more different the crystal structures of the layers are, the rougher and more uneven the surface will become. This also plays a significant role in the density and leak tightness of the electrode, which increases with a more similar crystal structure.

Model Material - LSF

Figure 4.1 shows a single LSF microelectrode under the Zeiss microscope. The width of the current collector grid was measured to be 12.4 µm, while the spacing in between was 37.4 µm. The diameter of the microelectrode itself was determined to be 249.6 µm. The surface appears to be smooth without significant differences between the LSF on the YSZ electrolyte and the Pt/Ti current collector grid.

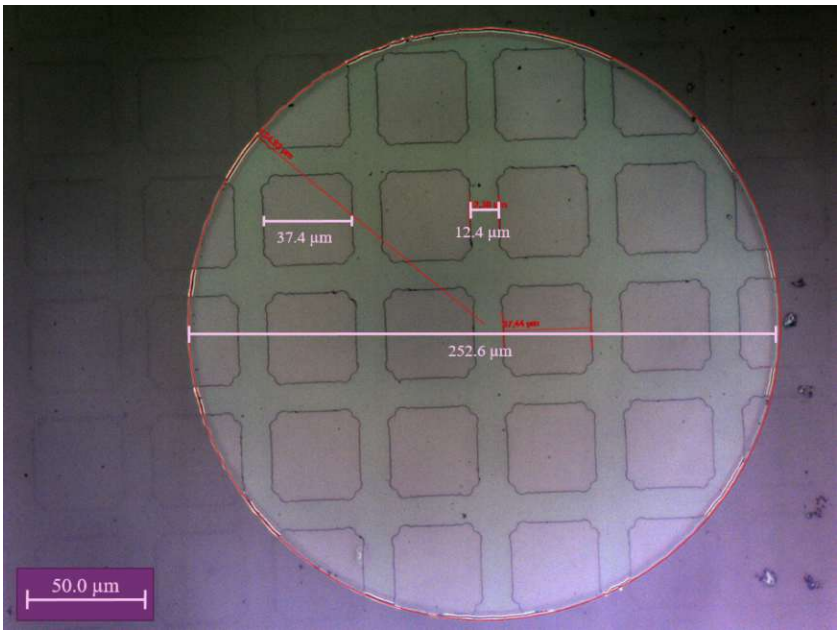

Figure 4.1: Light microscope close-up of one 250 µm LSF microelectrode with measurements for the current collector grid

Figure 4.2 shows a close-up of how LSF grows a) on the Pt/Ti grid and b) next to the current collector grid, directly on the YSZ electrolyte surface. Both sides show a kind of wrinkled surface with larger grains growing on top of it. The grains have a size of some 10 nm and can be assumed to be SrO particles. The LSF on the YSZ electrolyte looks a bit darker than on the Pt/Ti current collector grid, compared to the YSZ. There are slightly smaller parts on the film above the YSZ than above the Pt/Ti grid.

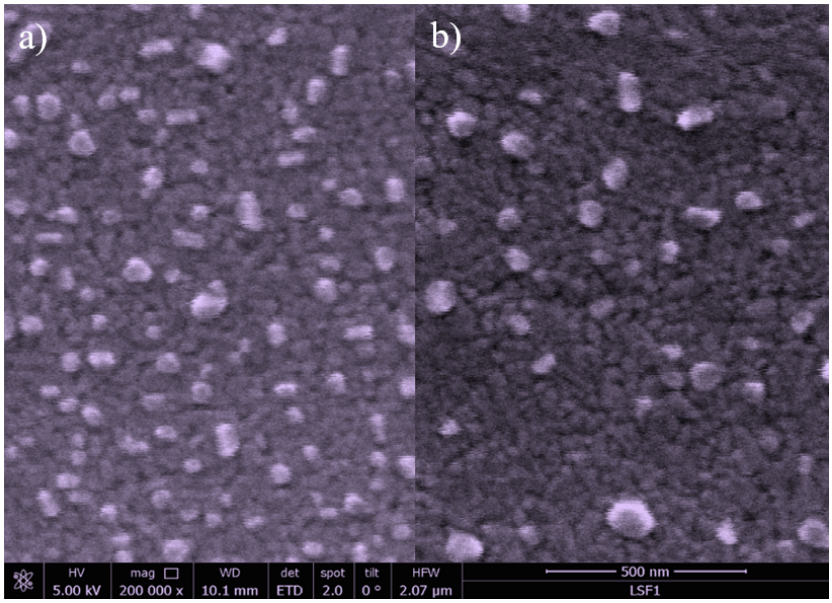

Figure 4.2: SEM image of the LSF surface grown a) on the Pt/Ti current collector grid and b) directly on the YSZ single crystal

LSCrMn

Figure 4.3 shows a single LSCrMn microelectrode under the microscope. The width of the current collector grid was measured to be 11.6 µm, while the spacing in between was 35.7 µm. The diameter of the microelectrode itself was determined to be 252.4 µm. Similar to the LSF film, the LSCrMn film also appears smooth without any significant differences between the LSCrMn layer on the YSZ electrolyte and the Pt/Ti grid.

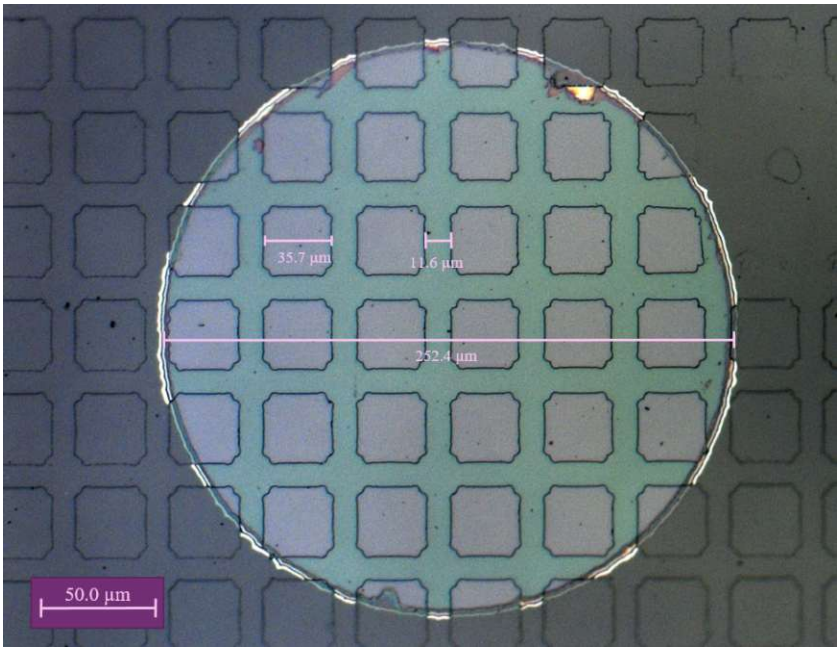

Figure 4.3: Light microscope close-up of one 250 µm LSCrMn microelectrode with measurements for the current collector grid

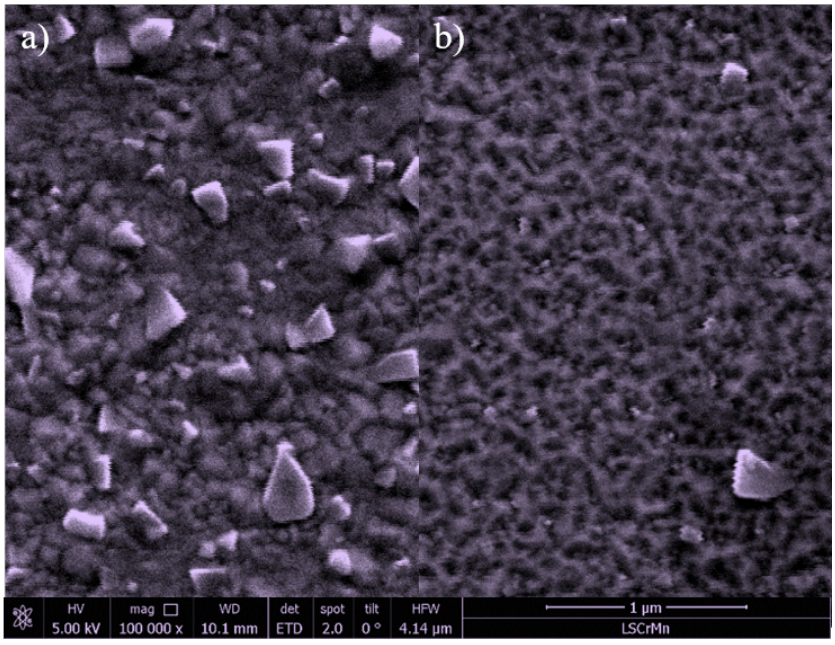

Figure 4.4: SEM image of the LSCrMn surface grown a) on the Pt/Ti current collector grid and b) directly on the YSZ single crystal

Figure 4.4 shows a close-up of how LSCrMn grows a) on the Pt/Ti grid and b) next to the current collector grid, directly on the YSZ electrolyte surface. The thin film grown on the current collector itself has a very rough and grainy surface with large crystal particles growing in multiple directions out of the surface. The thin film grown next to the current collector grid, directly on the YSZ electrolyte, while also a bit rough with small ridges on the surface, only has very few grains growing out of it.

GDC

Figure 4.5 shows a single GDC microelectrode under the microscope. The width of the current collector grid was measured to be 11.3 µm, while the spacing in between was 37.8 µm. The diameter of the microelectrode itself was determined to be 256.5 µm. The GDC thin film appears to be very smooth all over, however with a noticeable difference in darkness, with the GDC directly grown on the electrolyte appearing much darker in the light microscope image than the thin film grown on the current collector grid.

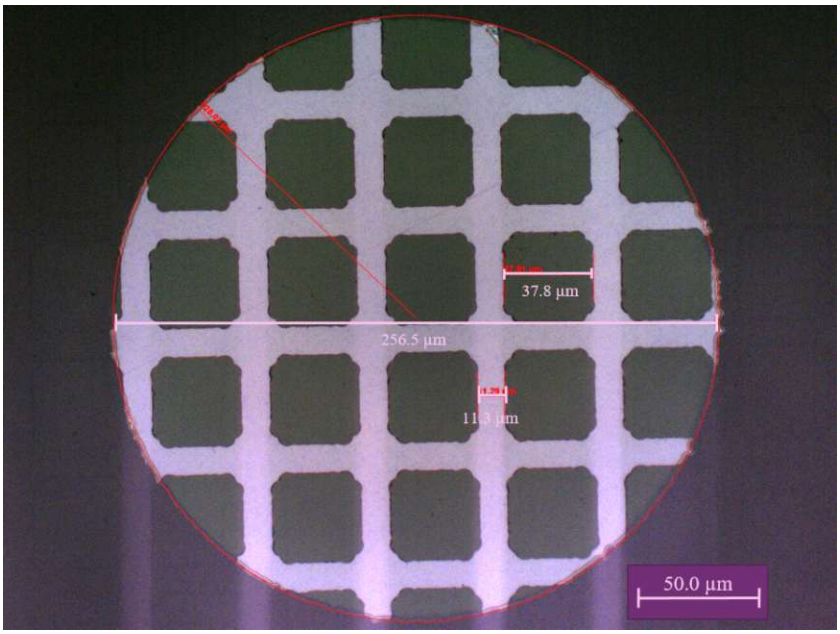

Figure 4.5: Light microscope close-up of one 250 µm GDC microelectrode with measurements for the current collector grid

Figure 4.6 shows a SEM image of a cross section of the GDC sample. The thickness of the deposited layer GDC layer was estimated to be 226.6 nm.

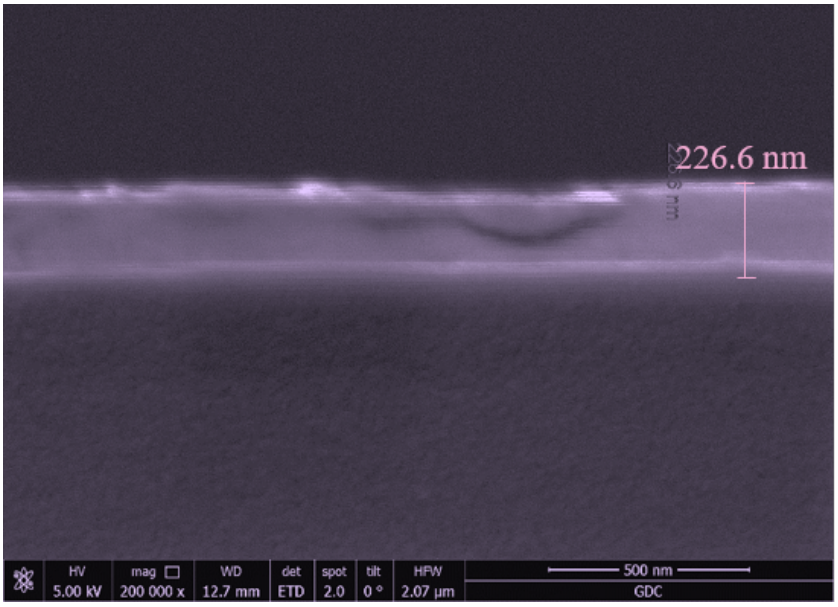

Figure 4.6: SEM image of the cross section of the GDC thin film deposited above the YSZ electrolyte.

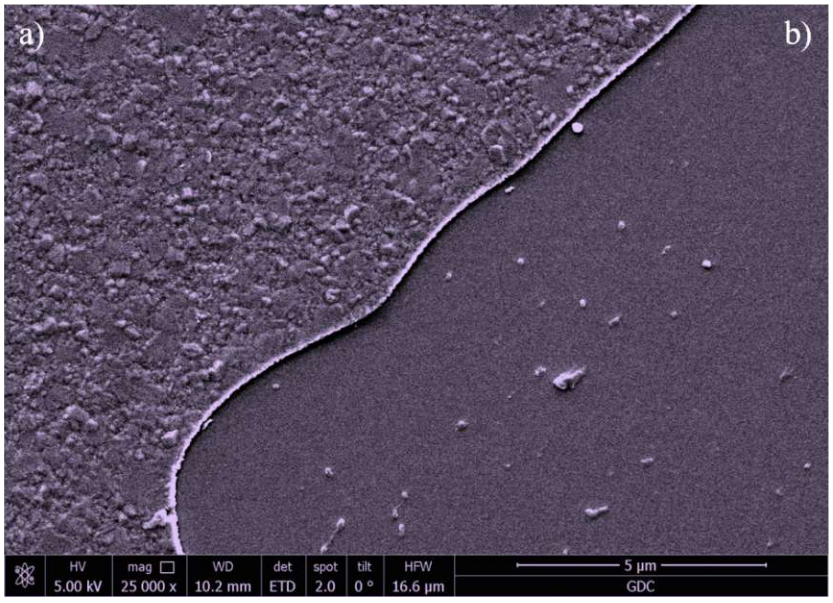

Figure 4.7: SEM image of the GDC surface grown a) on the Pt/Ti current collector grid and b) directly on the YSZ single crystal

Figure 4.7 shows a close-up of how GDC grows a) on the Pt/Ti grid and b) next to the current collector grid, directly on the YSZ electrolyte surface. The thin film grown on the current collector itself has a rough and grainy texture. The thin film grown next to the current collector grid, directly on the YSZ electrolyte, appears to be very smooth and dense with a low number of small and few particles disturbing the layer.

LNO

Figure 4.8 shows a single LNO microelectrode under the microscope. The width of the current collector grid was measured to be 12.7 µm, while the spacing in between was 36.2 µm. The diameter of the microelectrode itself was determined to be 255.4 µm. The LNO thin film appears to grow an even layer on the YSZ single crystal, but very rough and coarse with some light interference on the Pt/Ti grid. The color of the LNO on the current collector grid also seems to be a much darker shade and absorbing the light of the microscope much better than the LNO layer on the electrolyte. A possible explanation for the LNO layer on the current collector grid appearing much darker than next to it, could be that the smooth surface reflects the light of the optical microscope better and therefore appears lighter in the image, when directly compared to the thin film on the current collector.

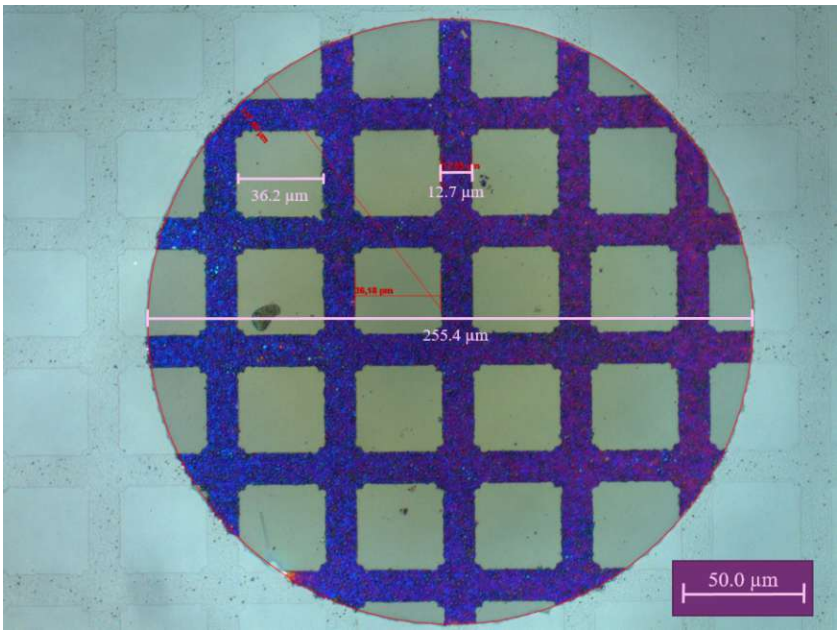

Figure 4.8: Light microscope close-up of one 250 µm LNO microelectrode with measurements for the current collector grid

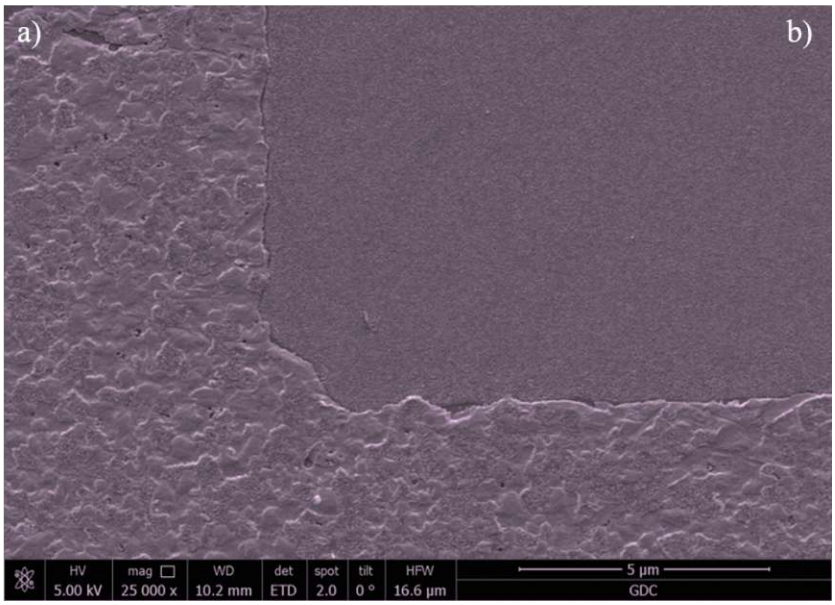

Figure 4.9: SEM image of the LNO surface grown a) on the Pt/Ti current collector grid and b) directly on the YSZ single crystal

Figure 4.9 shows a close-up of how LNO grows a) on the Pt/Ti grid and b) next to the current collector grid, directly on the YSZ electrolyte surface. The thin film grown on the electrolyte is smooth and dense with litte to no imperfections or visible grains. On the current collector itself the thin film layer has a rough and grainy texture.

$YBaCo_4O_7$

Figure 4.10 shows a single $YBaCo_4O_7$ microelectrode under the microscope. The width of the current collector grid was measured to be 17.0 µm, while the spacing in between was 25.2 µm. The diameter of the microelectrode itself was determined to be 257.5 µm. The $YBaCo_4O_7$ thin film appears to have a very rough and coarse texture all over, with the layer directly on the electrolyte appearing slightly darker than on the Pt/Ti grid.

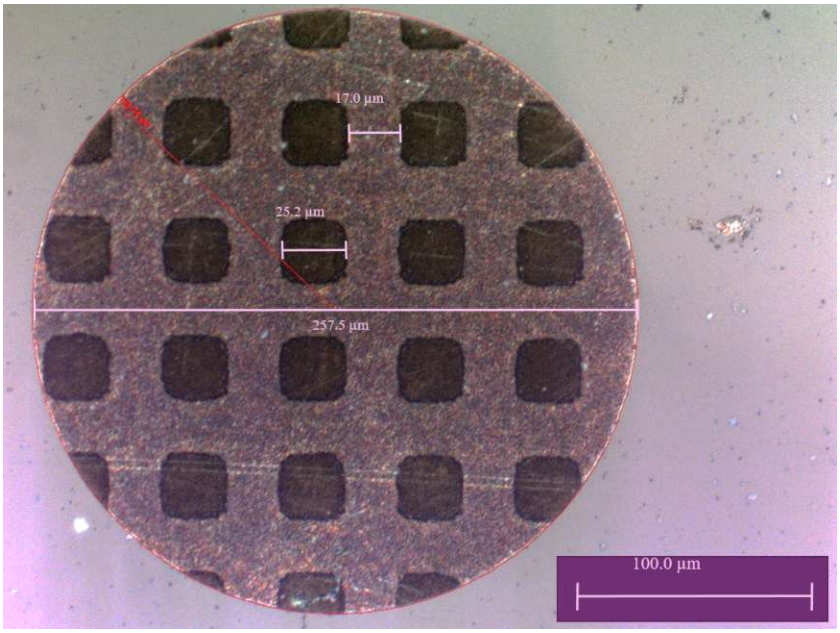

Figure 4.10: Light microscope close-up of one 250 µm $YBaCo_4O_7$ microelectrode with measurements for the current collector grid

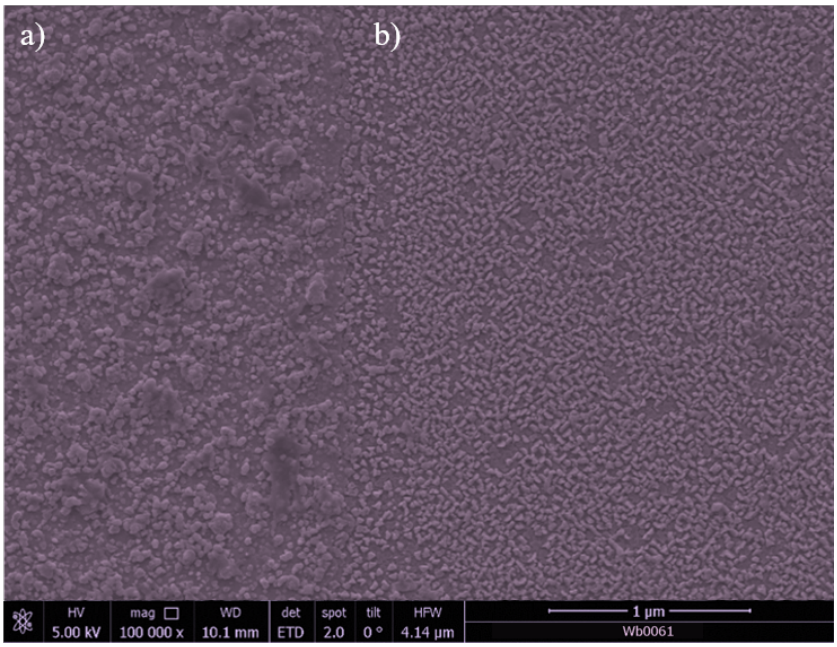

Figure 4.11: SEM image of the $YBaCo_4O_7$ surface grown a) on the Pt/Ti current collector grid and b) directly on the YSZ single crystal

Figure 4.11 shows a close-up of how $YBaCo_4O_7$ grows a) on the Pt/Ti grid and b) next to the current collector grid, directly on the YSZ electrolyte surface. Both on and next to the current collector grid the material grows in a very coarse and rough manner with the particles directly on the electrolyte appearing to be smaller in general and more even in size and distribution on the surface, with a clear preferred orientation. The thin film grown on the current collector grid appears to have larger protruding particles and is more uneven in size and distribution.

STO

Figure 4.12 shows a single STO microelectrode under the microscope. The width of the current collector grid was measured to be 15.9 µm, while the spacing in between was 27.2 µm. The diameter of the microelectrode itself was determined to be 254.5 µm. The STO thin film appears to be very smooth overall, with the STO directly grown on the electrolyte appearing almost black under the light, while the STO on the Pt/Ti grid creates a green-yellowish light interference.

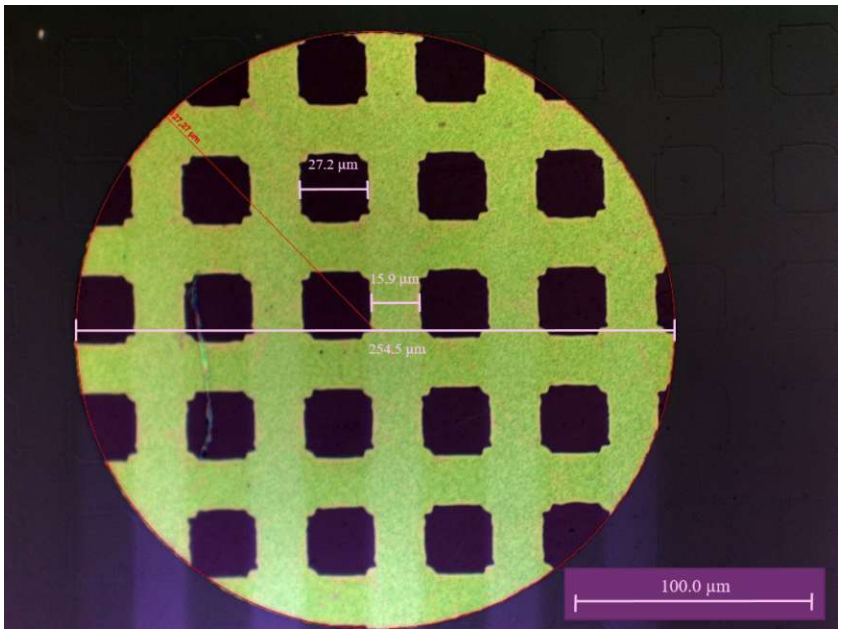

Figure 4.12: Light microscope close-up of one 250 µm STO microelectrode with measurements for the current collector grid

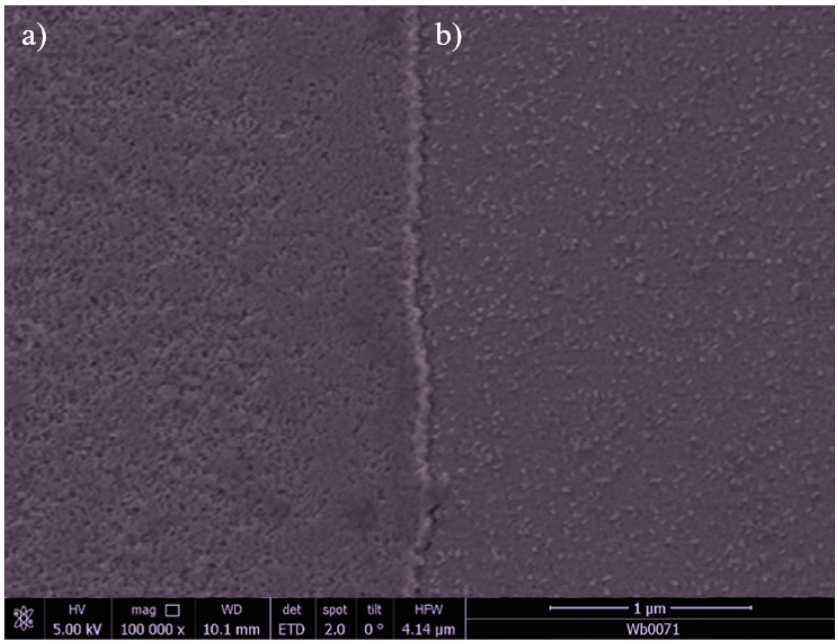

Figure 4.13: SEM image of the STO surface grown a) on the Pt/Ti current collector grid and b) directly on the YSZ single crystal

Figure 4.13 shows a close-up of how STO grows a) on the Pt/Ti grid and b) next to the current collector grid, directly on the YSZ electrolyte surface. The thin film grown on the current collector itself has indents on an otherwise smooth surface and the STO grown on the YSZ electrolyte has small crystal structures protruding from the rest of the film. Overall, both appear to be relatively dense and even.

LCF

Figure 4.14 shows a single LCF microelectrode under the microscope. The width of the current collector grid was measured to be 18.7 µm, while the spacing in between was 30.9 µm. The diameter of the microelectrode itself was determined to be 253.8 µm. The LCF thin film appears to be smooth but becomes uneven on the outer edges of the microelectrode. The microelectrode has a distinguishable interference halo on the edge of the electrode, indicating a height difference of the layer compared to the center of the electrode.

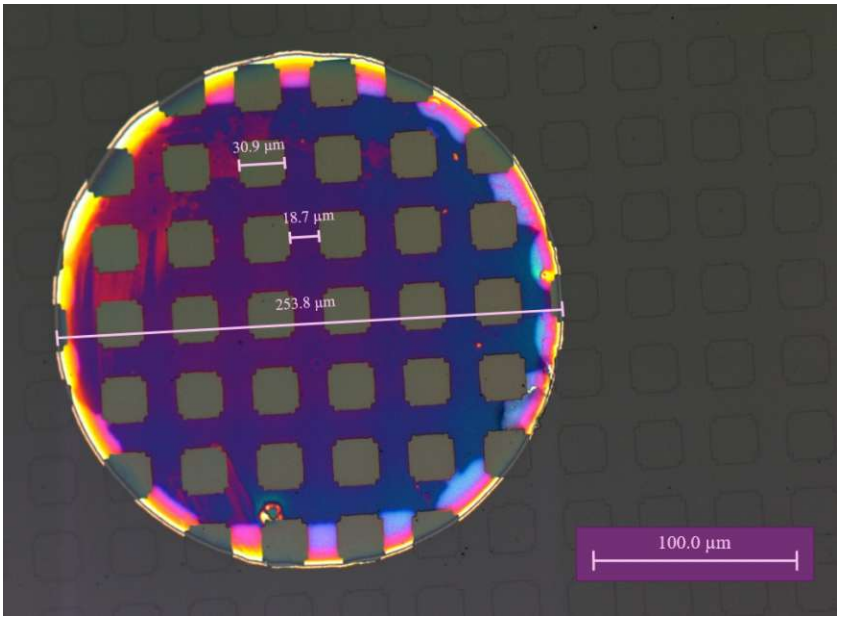

Figure 4.14: Light microscope close-up of one 250 µm LCF microelectrode with measurements for the current collector grid

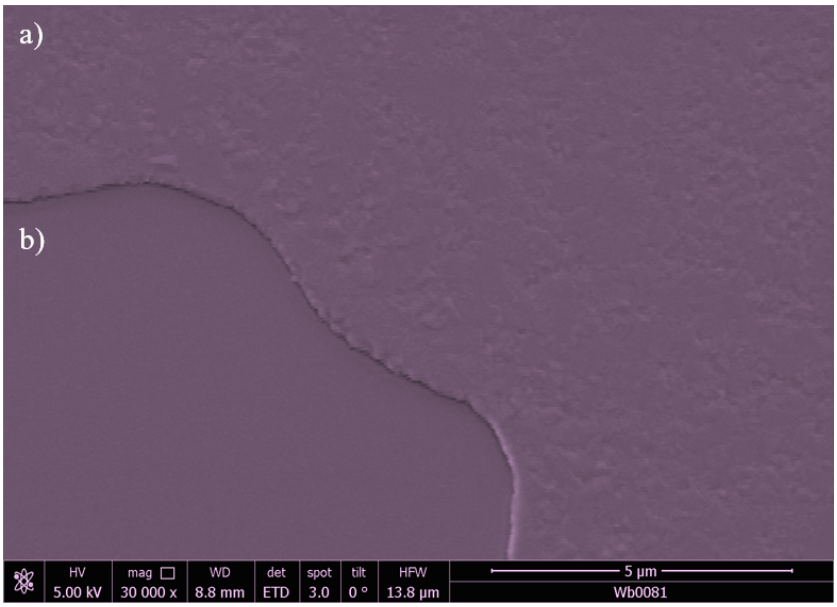

Figure 4.15: SEM image of the LCF surface grown a) on the Pt/Ti current collector grid and b) directly on the YSZ single crystal

Figure 4.15 shows a close-up of how LCF grows a) on the Pt/Ti grid and b) next to the current collector grid, directly on the YSZ electrolyte surface. Overall, both surfaces appear to be very dense and even. With the thin film grown on the current collector itself shows slight indents and protrusions on an otherwise leveled surface, the LCF grown on the YSZ electrolyte seems to have grown nearly perfectly even and dense.

4.2 Electrochemical Characterization

All samples were characterized by EIS and from the spectra the chemical capacitance was extracted (details see below). This chemical capacitance was then used to predict the charge/voltage characteristics of an OIB electrode made from the respective material. The electrochemical characterization with impedance measurements was either conducted in a oxidizing 1% O_2 in N_2 or a reducing, humidified H_2 atmosphere with Ar as the carrier gas. To be able to compare different data sets with each other, the potential was normalized to 1 bar O_2. This shift can be calculated with the Nernst equation (Equation (4.1) and results in a potential shift, that can be calculated by:

$$\eta_{shift} = \frac{RT}{2F} \cdot ln(\frac{p_{O_2,\ chamber}}{p_{O_2,\ norm}}) \tag{4.1}$$

With p_{O_2} being the oxygen partial pressure in the measuring chamber and $p_{O_2,\ norm}$ for the standard pressure of 1.013 bar. The measurement frequency ranged from 1 MHz to 4 mHz and stayed constant for all samples. For all samples, cathodic bias measurements were performed in steps of -50 mV up to 2500 mV, depending on the sample. In addition, for the LNO and $YBaCo_4O_7$ sample, anodic bias measurements in steps of 50 mV up to 500 mV were performed. The measurement temperatures were 350 °C to 600 °C. The exact measurement parameters for each sample can be seen in Table 4.1.

Table 4.1: EIS measurement parameters

	Bias Range (mV)	Bias Step (mV)	Temperature Range (°C)	Atmosphere
LSF	-1500 - 0	50	400 - 600	1% O_2
LSCrMn	-2500 - 0	50	350 - 600	1% O_2
GDC	-1800 - 0	50	350 - 600	1% O_2, wet H_2
LNO	-1500 - 500	50	400 - 600	1% O_2
$YBaCo_4O_7$	-1500 - 500	50	350 - 600	1% O_2
STO	-2000 - 0	50	500	1% O_2, wet H_2

4.2.1 Model Material - LSF ($La_{0.6}Sr_{0.4}FeO_{3-\delta}$)

LSF was chosen as a possible electrode material due to its well studied crystal structure and defect chemistry and thus also serves to validate our microelectrode based approach. It is an A-site acceptor-doped perovskite-type MIEC and changes its electronic properties with the $Fe^{4+}/Fe^{3+}/Fe^{2+}$ ratio. Measurements were conducted in a 1% O_2 atmosphere between 600 and 400 °C. 3-Point measurements and the recreation of the OIB battery curve for LSF have been done before[34] and due to its well studied nature, LSF was used to see, if those measurements could be repeated, using microelectrodes. The following section also describes in detail, how the battery curve was obtained. Since these steps stays the same for all materials, it will only be explained here.

EIS Measurements

Figures 4.16, 4.17 and 4.18 show the measured impedance spectra (dots) of LSF for different set voltages and temperatures including the respective fit (lines) achieved from the equivalent circuit shown in the inset. The reason why the inset equivalent circuit was chosen is the Warburg curve appearance of the low frequency semi-circle and is elaborated in Chapter 2.5.3. Each figure shows four impedance spectra at -0.15 V (purple), -0.40 V (blue) -0.80 V (pink) and -1.20 V (teal) respectively. The high frequency feature represents the YSZ electrolyte. With a decreasing temperature, the high frequency feature (R_{YSZ}) increases strongly in resistance and changes from a downward slope, into a distinguishable semicircle. This was also a good indicator to control if the microelectrode was successfully connected or not. At 600 °C this value should not exceed 15 kΩ. Neither cathodic nor anodic polarization has an effect on the high

frequency feature. The medium frequency feature can be attributed to the interface resistance. It is not visible for all spectra, since it is sometimes overlapped by either the high or the low frequency feature. The low frequency feature represents the electrode material.

The electrolyte resistance increases from 7 kΩ at 600 °C to approximately 700 kΩ at 400 °C. The medium frequency interface feature is only identifiable at 600 °C, where it can be estimated to be approximately 300 Ω. The low frequency feature, contains the information about the chemical capacitance. Its diameter decreases with a bias increase, which is expected as nonlinear current voltage characteristics occur, and increases with a decrease in temperature. Since only the capacitance, that can be extracted from the low frequency feature was important, the high and medium frequency features were neglected in the fit and only considered by an R_{offset} resistance. The aforementioned Warburg curve, which demands the usage of a CPE element to fit the curves, can be seen in almost all measured spectra. The capacitance value of the CPE element can be calculated using its R_{CPE} and T_{CPE}.

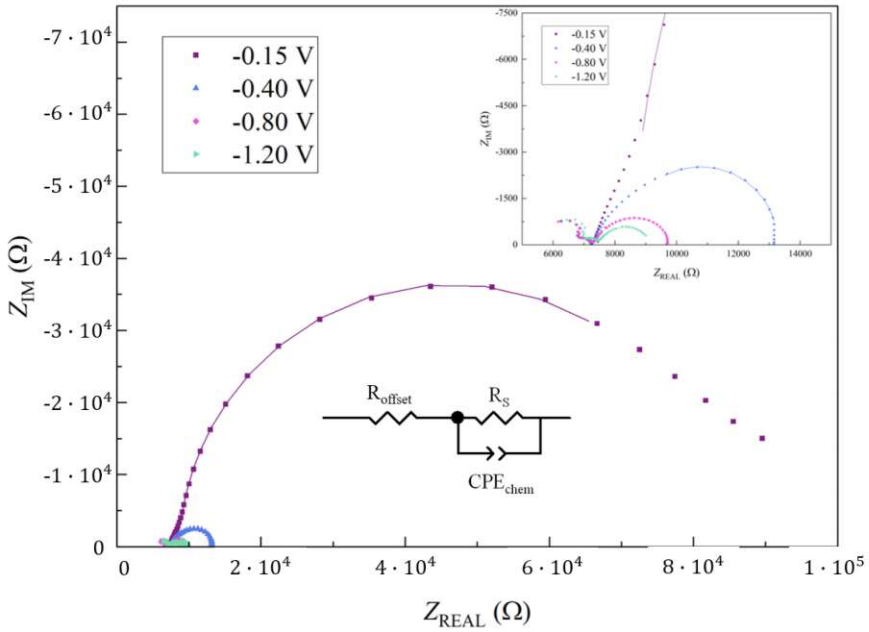

Figure 4.16: Measured impedance spectra of a 300 µm LSF microelectrode under cathodic bias measured in 1% O_2 atmosphere at 600°C. Data points are the measured values, and the fits are represented by solid lines.

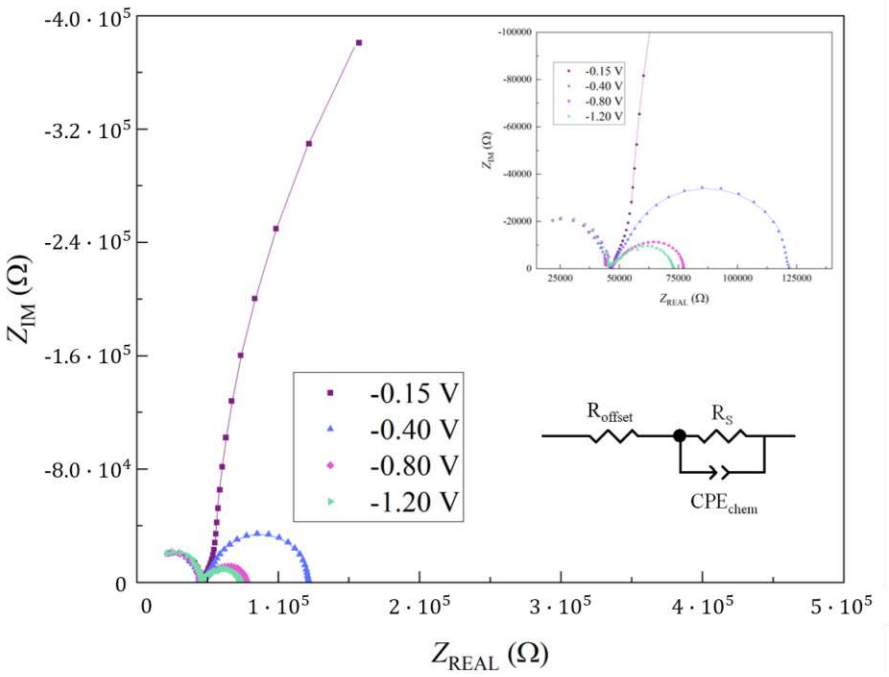

Figure 4.17: Measured impedance spectra of a 300 µm LSF microelectrode under cathodic bias measured in 1% O_2 atmosphere at 500°C. Data points are the measured values, and the fits are represented by solid lines.

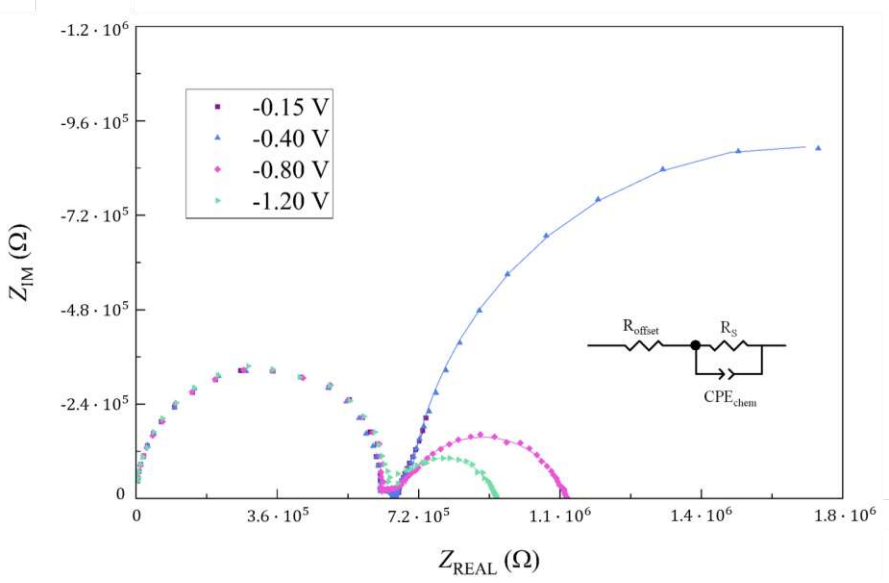

Figure 4.18: Measured impedance spectra of a 300 µm LSF microelectrode under cathodic bias measured in 1% O_2 atmosphere at 400°C. Data points are the measured values, and the fits are represented by solid lines.

Not all of the applied bias voltage is available at the electrode. According to the voltage divider laws, parts of it are lost at the electrolyte, the interface or through electronic transport. The effective overpotential at the working electrode was therefore calculated as seen in Equation (4.2).

$$\eta_{WE} = U_{DC} - I_{DC} \cdot R_{YSZ} \tag{4.2}$$

Reconstruction of the battery curves

The chemical capacitance of an oxide is defined as:

$$C_{chem} = 4 \cdot F^2 \, Vn^0 \cdot (\frac{\partial \mu_O}{\partial c_O})^{-1} \tag{4.3}$$

With F being Faraday's constant, V the sample volume, n_0 the absolute concentration of oxygen sites, μ_O the oxygen chemical potential and c_O the normalized oxygen concentration. The latter, c_O, is directly related the capacity Q with:

$$\partial Q = 2 \, \partial c_O \tag{4.4}$$

The oxygen chemical potential of a MIEC with a high electronic conductivity and a slow oxygen exchange reaction at the surface can be expressed as:

$$\mu_O = \mu_O^0 + \frac{kT}{2} \cdot ln \frac{p^\star_{O_2}}{1 \; bar} \tag{4.5}$$

and can be varied with $p^\star_{O_2}$ with the effective oxygen partial pressure $p^\star_{O_2}$ being:

$$p^\star_{O_2} = 1 \; bar \cdot exp \frac{4 \cdot eU}{kT} \tag{4.6}$$

with the effective working electrode potential U being the difference between the effective overpotential η_{WE} (Eq. (4.2)) and the potential shift η_{shift} (Eq. (4.1)).

The chemical capacitance is the differential capacitance and represents the inverse slope of the battery curve, i.e. Eq. (4.7).

$$\frac{dU}{dQ} = \frac{1}{C_{chem}} = k \tag{4.7}$$

Therefore, it is possible to express the OIB battery capacity as a function of the potential at the working electrode as:

$$Q(U_{WE}) = \int_0^{U_{WE}} C_{chem} \cdot dU \tag{4.8}$$

Figure 4.19 shows how to get the OIB battery curves from the chemical capacitance curves in a graphical way.

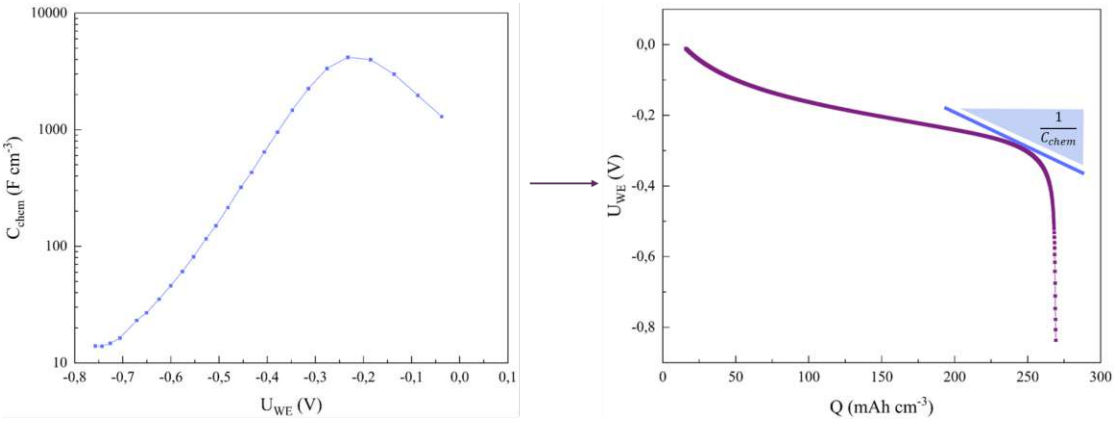

Figure 4.19: Visualization of exemplary chemical capacitance and battery curves.

The chemical capacitance C_{chem}, calculated from the CPE element, with its R_{CPE} and T_{CPE} values, was normalized to the active electrode bulk volume, with d being the diameter of the contacted electrode and h the film thickness:

$$C_{chem} = (R^{1-P} \cdot T)^{\frac{1}{P}} \cdot \frac{4}{d^2 \cdot \pi \cdot h} \tag{4.9}$$

Figure 4.20 shows the potential normalized to 1 bar O_2 against the calculated chemical capacitance C_{chem}. η_{shift} is temperature dependent and is -0.039 V (400 °C), -0.049 V (500 °C) and -0.059 V (600 °C). The blue curve for the measurements at 400 °C starts at a value of 615 F cm^{-3}

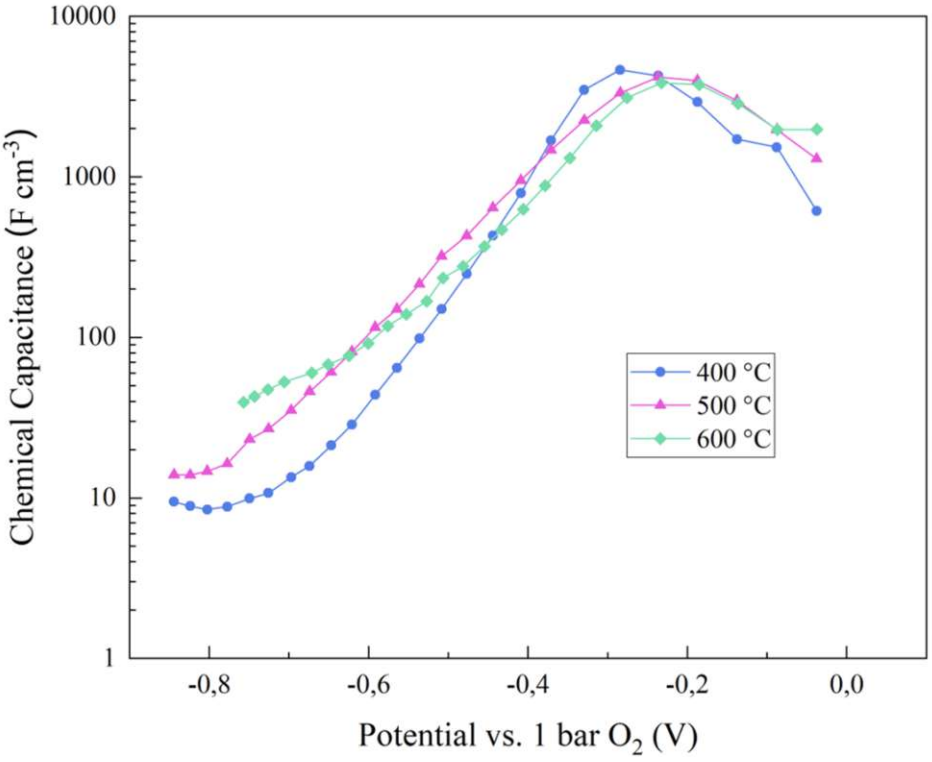

Figure 4.20: Chemical capacitance as a function of the effective electrode overpotential for a 300 µm LSF microelectrode, from 0 to -900 mV cathodic bias at different temperatures

at -0.049 V and rises to a local maximum of 4644 F cm^{-3} at -0.28 V. After this maximum, the chemical capacitance drops to a value of 8.5 F cm^{-3} at -0.83 V and then shows a continuation for another increase afterwards. The pink curve for the measurements at 500 °C starts at a value of 1296 F cm^{-3} at -0.049 V and rises to a local maximum of 4239 F cm^{-3} at -0.23 V. After this maximum, the chemical capacitance drops to a value of 12.5 F cm^{-3} at -0.81 V. The teal curve for the measurements at 600 °C starts at a value of 1977 F cm^{-3} at -0.059 V and rises to a local maximum of 3845 F cm^{-3} at -0.24 V. After this maximum, the chemical capacitance decreases to its lowest measured point with a value of 34.4 F cm^{-3} at -0.65 V. From a defect chemical point of view and when taking the Brouwer diagram (Figure 2.6) into consideration, oxide ions are released from the material, forming an oxygen vacancy and two electrons:

$$2\delta e^- + La_{0.6}Sr_{0.4}FeO_3 \rightleftharpoons La_{0.6}Sr_{0.4}FeO_{3-\delta} + \delta\, O^{2-} \tag{4.10}$$

This can also be expressed as:

$$2\ Fe_{Fe}^{\cdot} + 2\delta e_{cc}^{-} + O_{O}^{x} \rightleftharpoons \delta O_{yte}^{2-} + \delta V_{O}^{\cdot\cdot} + 2\ Fe_{Fe}^{x} \tag{4.11}$$

or

$$2\ Fe_{Fe}^{x} + \mathrm{O}_{\mathrm{O}}^{\times} + 2\delta e_{cc}^{-} \rightleftharpoons \delta \mathrm{O}_{\mathrm{yte}}^{2-} + V_{\mathrm{O}}^{\cdot\cdot} + 2\ Fe_{Fe}^{\prime} \tag{4.12}$$

When looking at the chemical capacitance as a function of the effective electrode overpotential, it scales with the minority charge carrier. Right of the maximum the holes are the majority defect and the oxygen vacancies slowly increase, while the holes slowly decrease. The ratio of Fe^{4+}/Fe^{3+} at this part of the curve is 0.4/0.6 to balance the Sr acceptor doping. At the peak, the oxygen vacancy and hole concentration is about equal and the chemical capacitance reaches a local maximum. Left of the peak, the vacancy concentration remains constant, while the hole concentration decreases and the electron concentration rises. The ratio of Fe^{4+}/Fe^{3+} at this part of the curve is about 0.0/1.0. The local minimum is the stoichiometric point of the Brouwer diagram, where the hole and electron concentration is equal. The oxygen vacancy concentration stays constant and is still the majority defect. After this minimum, the electron concentration is larger than the hole concentration. Upon further lowering of the potential, the material reaches its stability limit and eventually starts to disintegrate at around -1.2 V.

Figure 4.21 shows the resulting battery curves reconstructed from the corresponding C_{chem} measurements, compared with the DC battery curve at 500 °C. The capacity has a plateau at around -0.2 V for 200 mA h cm^{-3} and then has a sharp cut off capacity between 260 and 280 mA h cm^{-3}. LSF used as an electrode material shows very similar across the wide temperature range and is also in good agreement with the previously measured DC measurements. This confirms that the microelectrode approach is a viable technique for predicting battery curves.

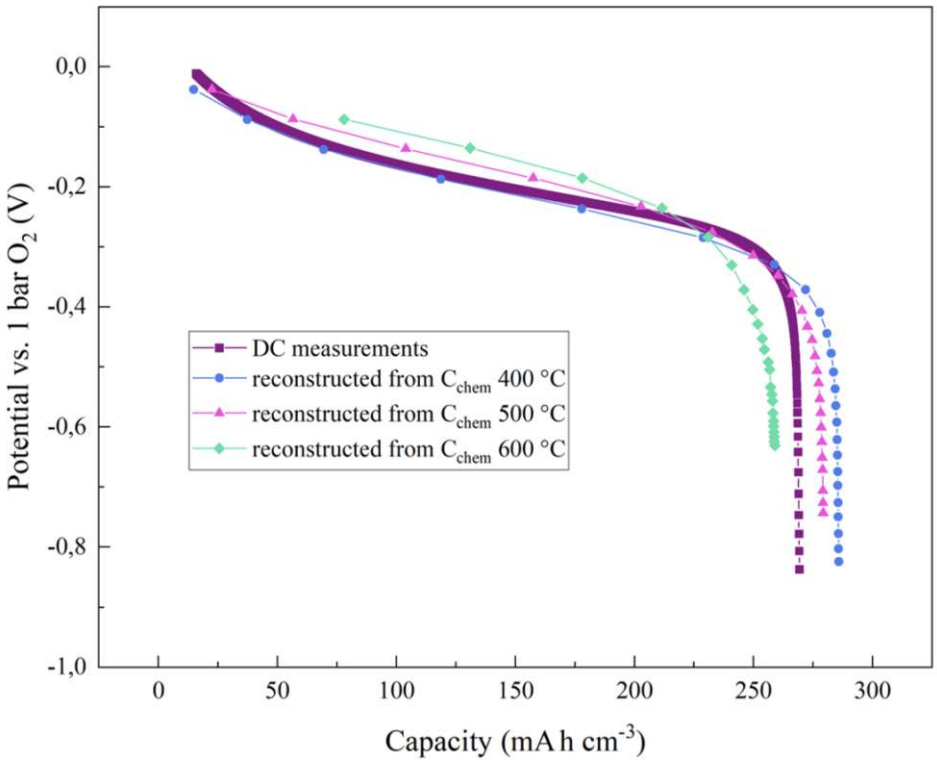

Figure 4.21: Potential vs. capacity curves for a 300 µm LSF microelectrode, from 0 to 900 mV cathodic bias reconstructed from chemical capacitance measurements at different temperatures

4.2.2 LSCrMn ($La_{0.5}Sr_{0.5}Cr_{0.2}Mn_{0.8}O_{3-\delta}$)

LSCrMn was chosen as a possible electrode material due to its low reducibility and thus an expected very negative potential. LSCrMn itself is an A-site acceptor-doped perovskite-type MIEC with a ratio of 0.2/0.8 of Cr^{3+}/Mn^{3+} on the B-site. Measurements were conducted in a 1% O_2 atmosphere between 600 and 350 °C. The applied cathodic biases range from 0 to -2000 mV in -50 mV steps.

EIS Measurements

Figures 4.22, 4.23, 4.24 and 4.25 show the measured impedance spectra (dots) and the respective fit (lines) achieved from the equivalent circuit shown in the inset, of LSCrMn for different set voltages and temperatures. Each figure shows four impedance spectra at -0.20 V (purple), -0.60 V (blue) -1.20 V (pink) and -1.80 V (teal) respectively. The high frequency feature is the intercept

arc and represents the YSZ electrolyte. The medium frequency feature can be attributed to the interface resistance. It is not visible for all spectra, since it sometimes overlaps with either the high or the low frequency feature. The low frequency feature represents the electrode materials electrochemical surface reaction and chemical capacitance. The electrolyte resistance increases from 6 kΩ at 600 °C to approximately 2.4 MΩ at 350 °C. The low frequency feature again decreases with a bias increase and increases with a decrease in temperature. At low bias voltages (up to -0.60 V) the low frequency feature exhibits a distinct slope on its high frequency arc. At higher bias voltages, this slope gradually vanishes and a small, depressed semicircle (800 Ω at 600°C to 120 kΩ at 350 °C) becomes visible at intermediate frequencies. Since only the capacitance, that can be extracted from the low frequency feature was important, the high and medium frequency features were neglected in the fit and only considered with an R_{offset} resistance. The low frequency semi-circle shrinks with an increasingly cathodic bias and its resistance ranges from around 720 kΩ at -0.20 V to 400 Ω at -1.8 V at 600 °C The resistance values for the low frequency semi-circle at all bias values also gradually increase with a decrease in temperature.

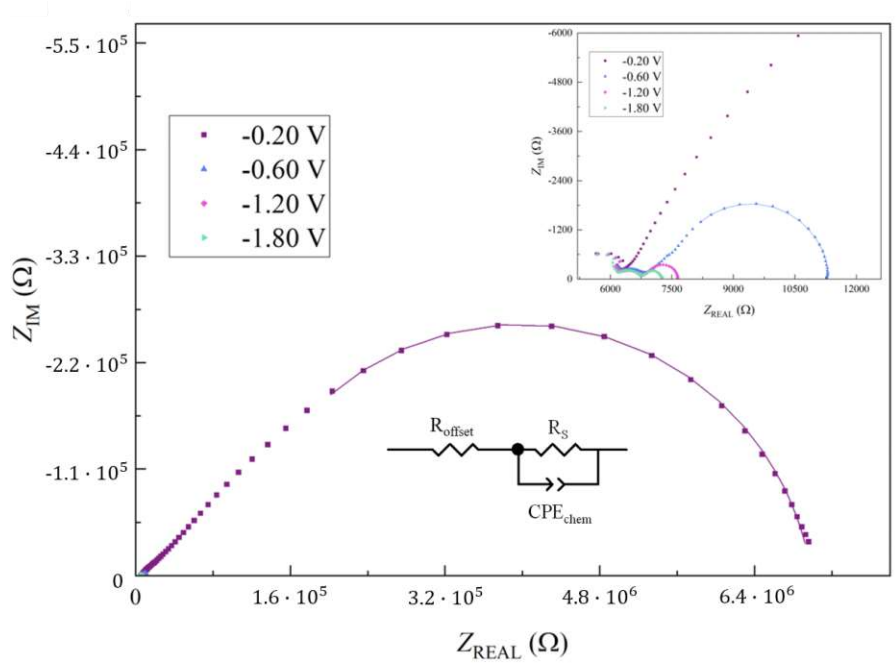

Figure 4.22: Measured impedance spectra of a 300 µm LSCrMn microelectrode under cathodic bias measured in 1% O_2 atmosphere at 600°C. Data points are the measured values, and the fits are represented by solid lines.

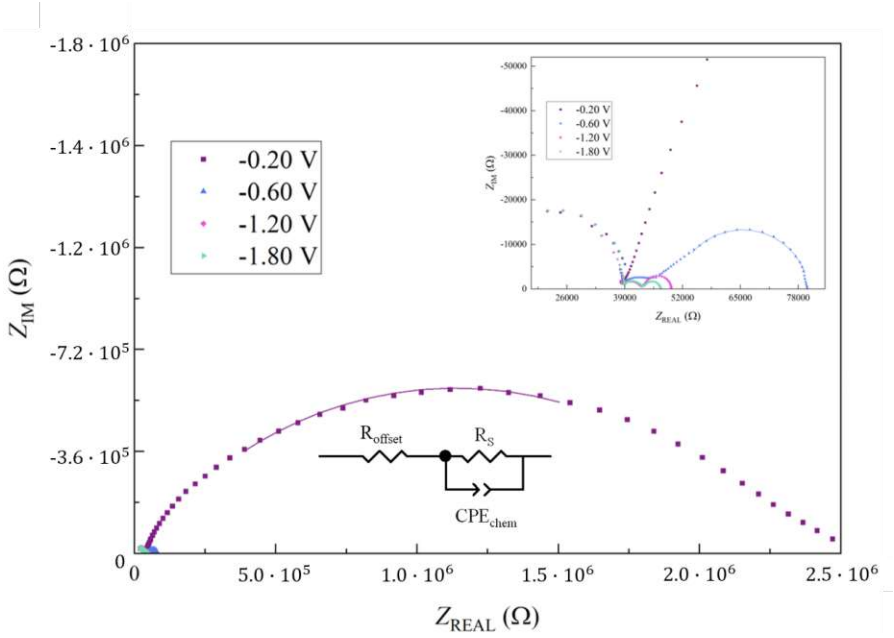

Figure 4.23: Measured impedance spectra of a 300 µm LSCrMn microelectrode under cathodic bias measured in 1% O_2 atmosphere at 500°C. Data points are the measured values, and the fits are represented by solid lines.

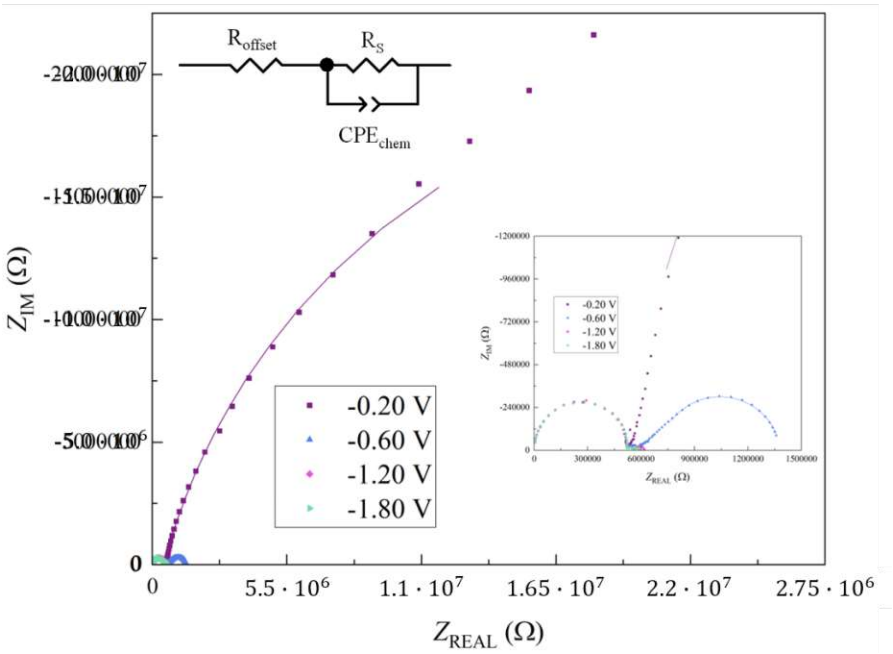

Figure 4.24: Measured impedance spectra of a 300 µm LSCrMn microelectrode under cathodic bias measured in 1% O_2 atmosphere at 400°C. Data points are the measured values, and the fits are represented by solid lines.

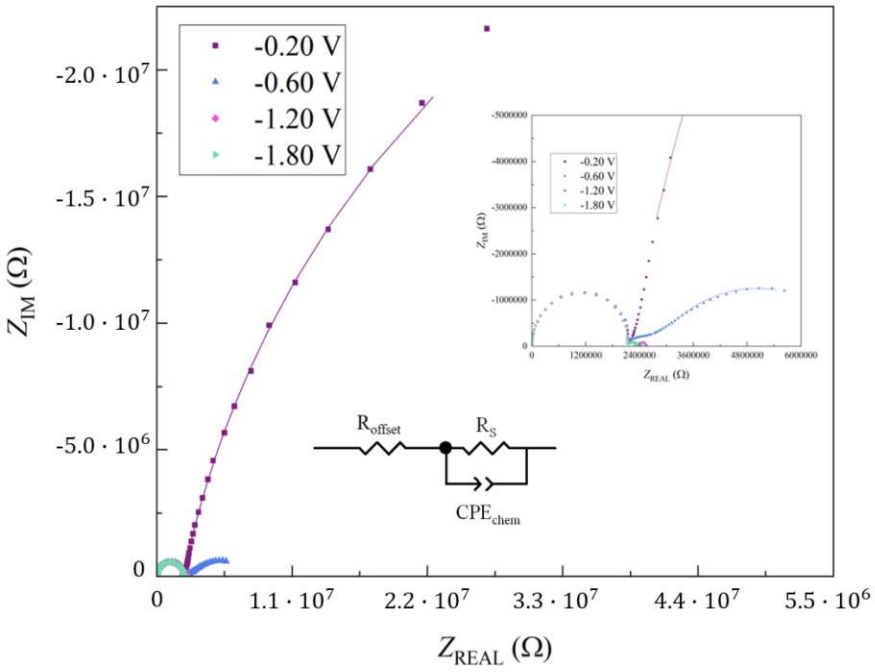

Figure 4.25: Measured impedance spectra of a 300 µm LSCrMn microelectrode under cathodic bias measured in 1% O_2 atmosphere at 350°C. Data points are the measured values, and the fits are represented by solid lines.

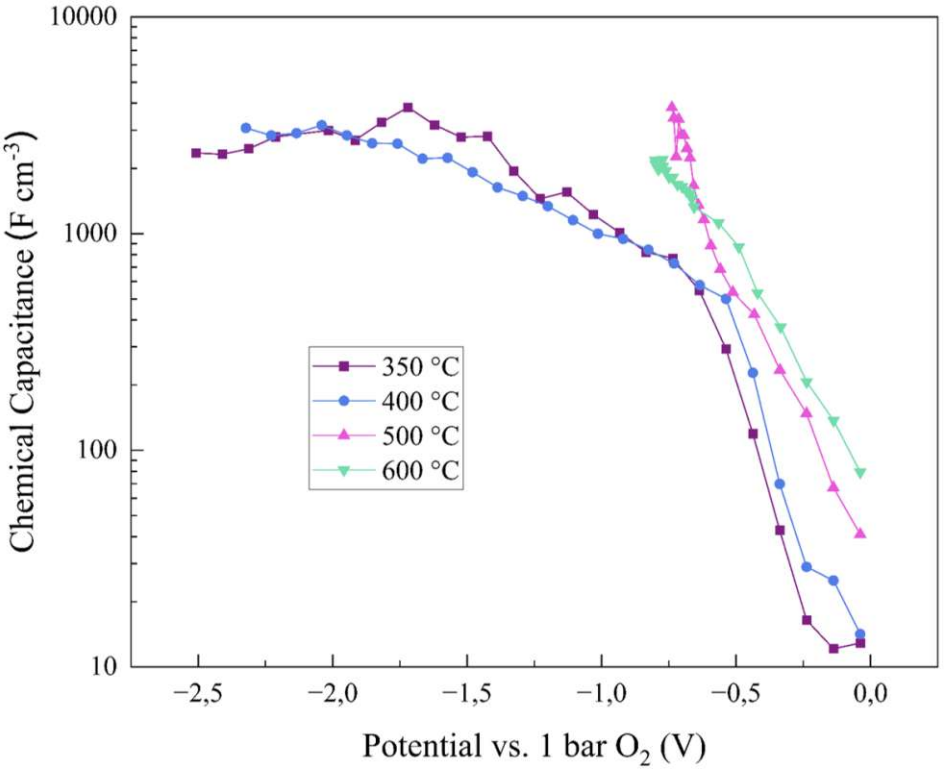

Figure 4.26: Chemical capacitance as a function of the effective electrode overpotential for a 300 µm LSCrMn microelectrode, from 0 to -2500 mV cathodic bias at different temperatures

Reconstruction of the battery curves

Figure 4.26 shows the chemical capacitance C_{chem} against the potential normalized to 1 bar O_2 and Figure 4.27 shows the resulting battery curves reconstructed from the corresponding C_{chem} measurements, compared with the measured DC battery curve. The purple curve for the measurement at 350 °C starts at a value of 12.9 F cm^{-3} at -0.035 V, rises to a plateau with a maximum value of 3823 F cm^{-3} at 1.72 V and stays almost constant until the last measured potential at -2.51 V. The blue curve for the measurements at 400 °C starts at a value of 14.2 F cm^{-3} at -0.039 V and rises to a local maximum of 3164 F cm^{-3} at -0.20 V and also stays constant until the last measured potential at -2.32 V. The pink curve for the measurements at 500 °C starts at a value of 36.0 F cm^{-3} at -0.049 V and rises to a local maximum of 3812 F cm^{-3} at -0.74 V. Higher polarizations of the electrode were not achievable, as the majority of the applied voltage is lost at the electrolyte and interface resistances. The teal curve for the measurements

at 600 °C starts at a value of 79.2 F cm^{-3} at -0.059 V and rises to 2198 F cm^{-3} at -0.77 V. After this, the same happens as for 500 °C - Higher polarizations of the electrode were not achievable, as the majority of the applied voltage is lost at the electrolyte and interface resistances.

To understand the defect chemical phenomena that occur when polarizing the electrode, we have to look at its chemical composition and the elemental charge per unit cell. The exact chemical composition of the LSCrMn is $La_{0.5}Sr_{0.5}Cr_{0.2}Mn_{0.8}O_{3-\delta}$. Without any applied voltage, i.e. under oxidizing conditions, the doping (0.5 charges per unit cell) is fully electronically compensated by the formation of 0.5 electron holes per unit cell. For simplicity, they are formally assigned to the Mn and thus the composition reads $(La_{0.5}Sr_{0.5})(Cr^{3+}_{0.2}Mn^{3+}_{0.3}Mn^{4+}_{0.5})O_3$. The volume of the unit cell (u.c) can be estimated to be $64 \cdot 10^{-24} cm^3$.

Switching the material from the full electronic compensation to the full ionic compensation corresponds to a reduction of Mn^{4+} to Mn^{3+}. This requires a charge of 0.5 e per unit cell, which corresponds to 350 mA h cm^{-3}. At 500 and 600 °C this is approximately the maximum capacity achieved (350 mA h cm^{-3}). At lower temperatures, however, much larger capacities (up to 1200 mA h cm^{-3}) at much lower potentials were achieved. For example, a capacity of 1200 mAh/cm³ corresponds to 1.75 e/u.c. Reducing both Mn and Cr from +3 to +2, thus giving $(La_{0.5}Sr_{0.5})(Cr^{2+}_{0.2}Mn^{2+}_{0.8})O_3$ corresponds to a charge of 1 e/u.c. (700 mA h cm^{-3}), This charge adds to the 0.5 e/u.c. required for reduction of Mn from 4+ to 3+ to give a total charge of 1.5 e per u.c. or 1050 mA h cm^{-3}. This still leaves 0.25 e/uc unaccounted for, which may indicate an even further reduction of the material but may also originate from inaccuracies in the determination of the electrode overpotential or the film volume.

The electrochemical reduction reaction thus reads:

$$0.5e^- + (La_{0.5}Sr_{0.5})(Cr^{3+}_{0.2}Mn^{3+}_{0.3}Mn^{4+}_{0.5})O_3 \rightleftharpoons (La_{0.5}Sr_{0.5})(Cr^{3+}_{0.2}Mn^{3+}_{0.3}Mn^{4+}_{0.5})O_{2.75} + 0.25\ O^{2-}_{\text{yte}} \quad (4.13)$$

for first reduction step, i.e. the transition from electronic to ionic compensation and

$$1e^- + (La_{0.5}Sr_{0.5})(Cr^{3+}_{0.2}Mn^{3+}_{0.3}Mn^{4+}_{0.5})O_3 \rightleftharpoons (La_{0.5}Sr_{0.5})(Cr^{3+}_{0.2}Mn^{3+}_{0.3}Mn^{4+}_{0.5})O_{2.75} + 0.5\ O^{2-}_{\text{yte}} \quad (4.14)$$

for the second reduction step.

Therefore it can be assumed, that LSCrMn it is able to provide two possible ways of changing its electronic properties. Either via the acceptor Sr doping on the A-site or the Cr/Mn ratio on the B-site.

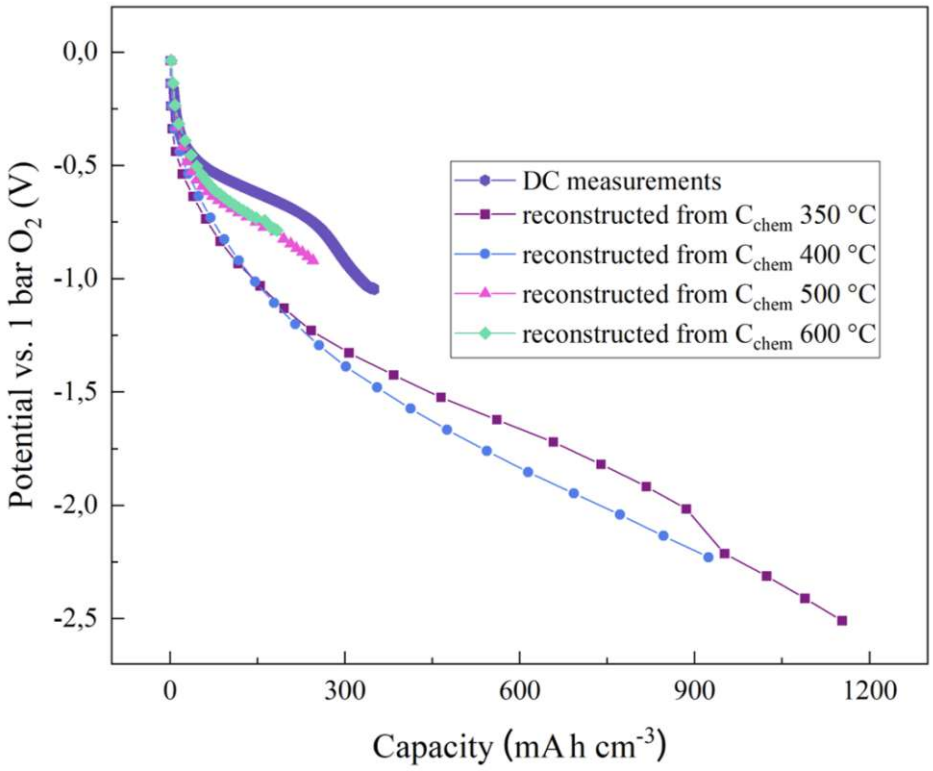

Figure 4.27: Potential vs. capacity curves for a 300 µm LSCrMn microelectrode, from 0 to 900 mV cathodic bias reconstructed from chemical capacitance measurements at different temperatures

When looking at the OIB battery curve in Figure 4.27, the capacity does not have a plateau at a specific potential and rather continues to increase with an increase in potential. For the measurements at 350 °C, the capacity reaches almost 1200 mA h cm^{-3} at a cathodic potential of -2450 mV, for 400 °C measurements more than 900 mA h cm^{-3} at -2200 mV were reached. For the measurements at 500 °C and 600 °C, even though set biases of up to -2500 mV were applied, the maximum potential at the working electrode, reached with the used sample architecture, was -1000 mV with capacitances of ca. 300 and 250 mA h cm^{-3}, respectively. In Figure 4.27 a previously measured DC curve (400 °C) is shown[10], which is in reasonable agreement with the curves deduced from C_{chem} in this thesis. All together, we can conclude that LSCrMn electrodes show a very high capacity at potentials of up to -2.5 V.

4.2.3 GDC Gd:CeO_2

GDC is an acceptor doped A-type fluorite material, with a similar crystal structure as YSZ and was chosen as a possible electrode material due to its high ionic conductivity even at low temperatures (< 700 °C)[53] and its reducibility in H_2 and CO atmospheres[54]. Although GDC is acceptor doped, it is already fully ionically compensated, without any applied potential. The switch between being not fully compensated and being compensated can therefore not be utilized, when using GDC as an electrode material. Instead, the intrinsic reduction from Ce^{4+} to Ce^{3+} at strongly reducing potentials is used.

Case specific for the exact chemical composition of the used GDC ($Gd^{3+}_{0.2}Ce^{4+}_{0.8}O_{2-\delta}$), without any applied voltage, i.e. under oxidizing conditions, 0.1 two-fold positively charged oxygen vacancies per formula unit are introduced into the crystal structure, to compensate the Gd doping. At very reducing conditions, further oxygen vacancies are formed and the Ce^{4+} is reduced to Ce^{3+}.

In Kröger-Vink notation this can be written as:

$$2\,Ce^{x}_{Ce} + O^{x}_{O} \rightleftharpoons V^{\cdot\cdot}_{O} + 2\,Ce'_{Ce} + \frac{1}{2}\,O_2 \tag{4.15}$$

The applied cathodic biases for the measurements in 1% O_2 range from 0 to -1800 mV in -50 mV steps and for humified H_2 from 0 to -1500 mV, with -50 mV steps as well.

EIS Measurements - 1% oxygen atmosphere

The first measurements were conducted in 1% oxygen atmosphere, to see if an applied voltage can indeed be used to reduce the material and store oxygen ions. Figures 4.28, 4.29, 4.30 and 4.31 show the measured impedance spectra (dots) and the respective fit (lines) achieved from the equivalent circuit shown in the inset, of GDC for different set voltages and temperatures. Each figure shows four impedance spectra at -0.20 V (purple), -0.60 V (blue) -1.20 V (pink) and -1.80 V (teal) respectively. The high frequency feature is the intercept arc and represents the YSZ electrolyte. The electrolyte resistance increases from 3.5 kΩ at 600 °C to approximately 1.2 MΩ at 350 °C. It is initially independent from the voltage, indicating that the YSZ electrolyte is not (yet) reduced by the chemical potentials introduced via the applied voltage. The medium frequency feature can be attributed to the interface resistance. It partly overlaps with

the low frequency feature at low bias voltages (up to -0.60 V). At higher bias voltages, this slope gradually decreases and turns the low frequency feature into a more depressed semicircle with a more shallow slope at intermediate frequencies. The low frequency feature represents the electrode material and again decreases with a bias increase and increases with a decrease in temperature. Since only the capacitance of the low frequency feature is important, the split into a high and medium frequency features was neglected in the fit and considered together with an R_{offset} resistance. The low frequency semi-circle shrinks with increasing cathodic bias and its resistance ranges from around 190 kΩ at -0.20 V to 1300 Ω at -1.8 V at 600 °C.

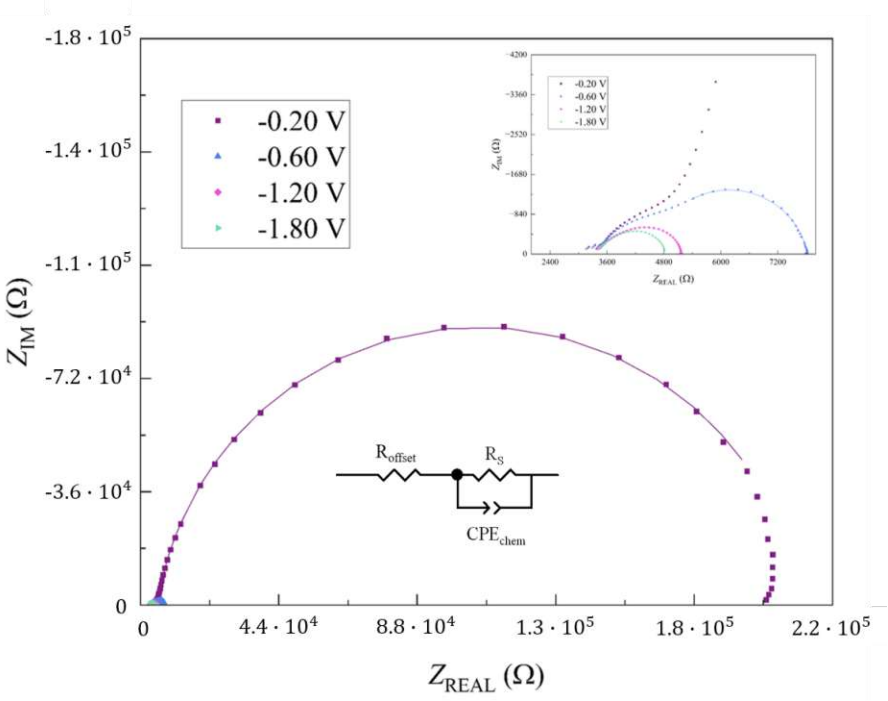

Figure 4.28: Measured impedance spectra of a 300 µm GDC microelectrode under cathodic bias measured in 1% O_2 atmosphere at 600°C. Data points are the measured values, and the fits are represented by solid lines.

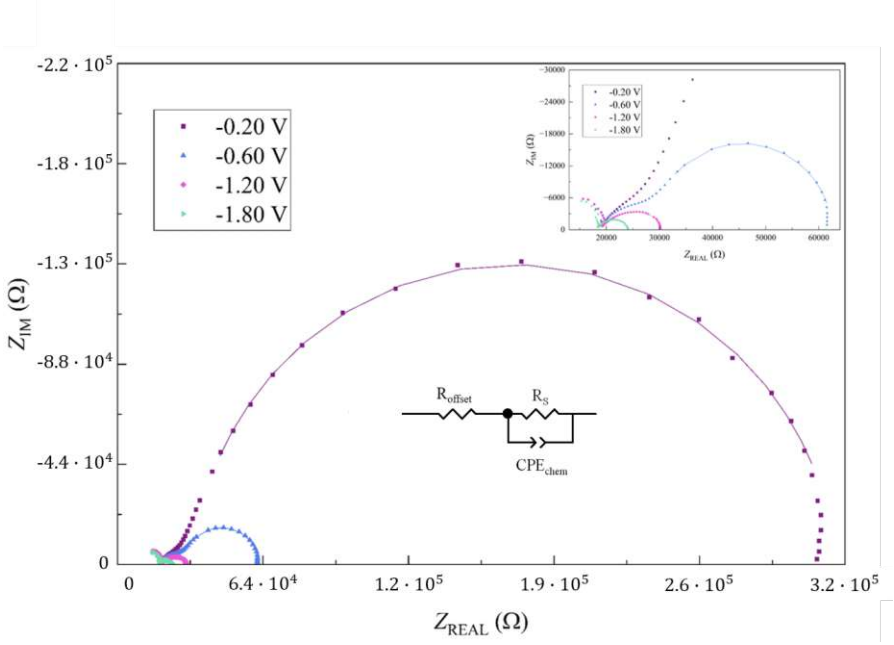

Figure 4.29: Measured impedance spectra of a 300 µm GDC microelectrode under cathodic bias measured in 1% O_2 atmosphere at 500°C. Data points are the measured values, and the fits are represented by solid lines.

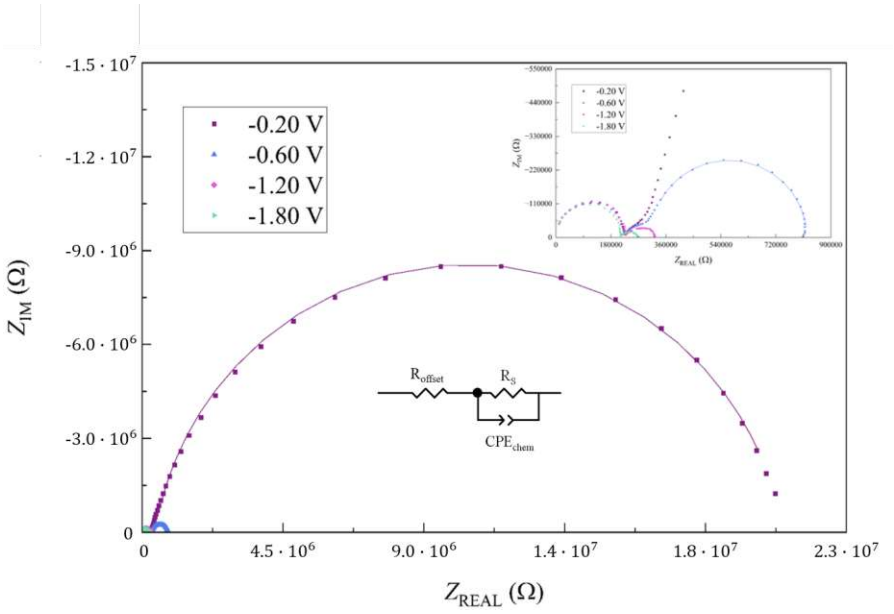

Figure 4.30: Measured impedance spectra of a 300 µm GDC microelectrode under cathodic bias measured in 1% O_2 atmosphere at 400°C. Data points are the measured values, and the fits are represented by solid lines.

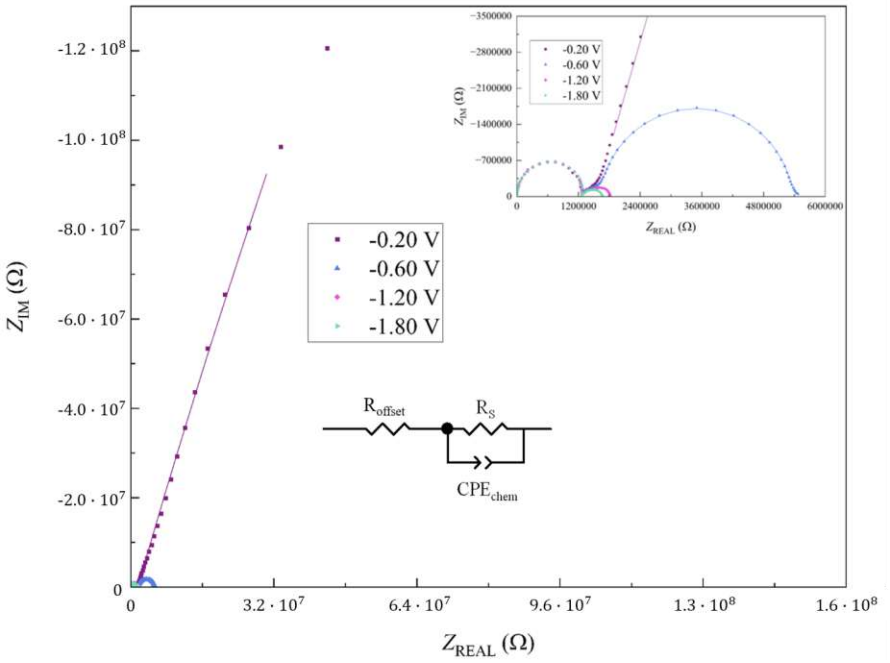

Figure 4.31: Measured impedance spectra of a 300 µm GDC microelectrode under cathodic bias measured in 1% O_2 atmosphere at 350°C. Data points are the measured values, and the fits are represented by solid lines.

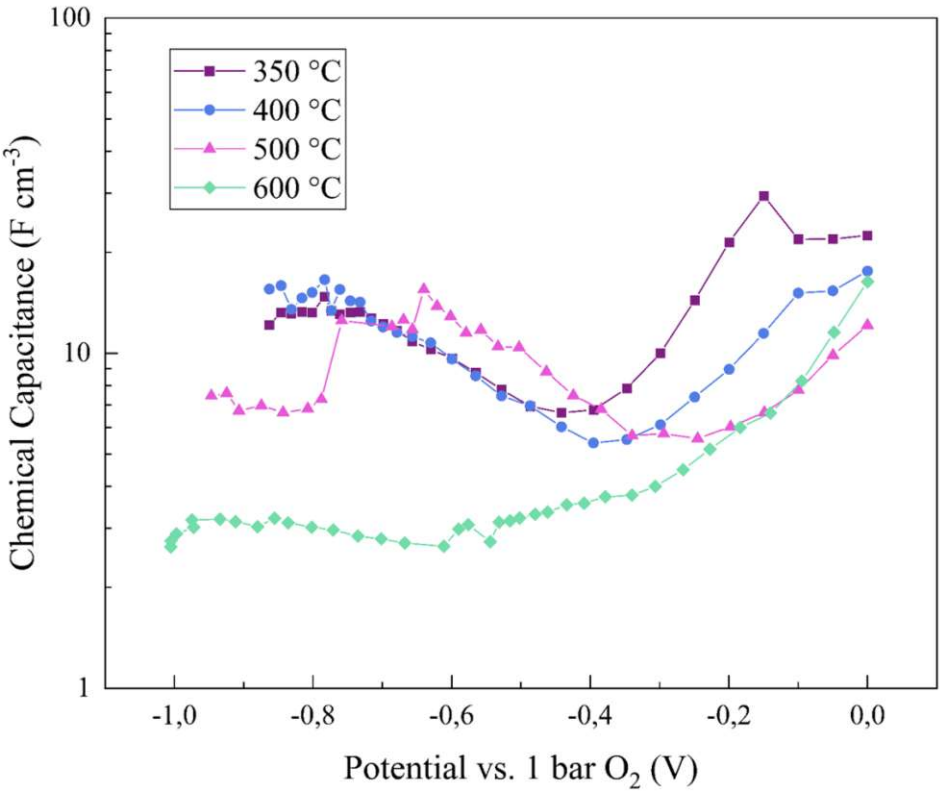

Figure 4.32: Chemical capacitance as a function of the effective electrode overpotential for a 300 µm GDC microelectrode, from 0 to -1000 mV cathodic bias at different temperatures

Reconstruction of the battery curves

Figure 4.32 shows the chemical capacitance C_{chem} against the potential normalized to 1 bar O_2 and Figure 4.33 shows the resulting battery curves reconstructed from the corresponding C_{chem} measurements. As evident from the data, GDC, polarized up to -1 V, exhibits a very low chemical capacitance. Similar to the LSCrMn measurements, the potential at the working electrode, becomes stagnant at around -0.9 to -1.0 V across all temperatures, due to a significant voltage drop across the other elements, instead of the WE. The chemical capacitance at -0.0376 V has values between 12.10 and 22.44 F cm^{-3}. The curves then show a slight decrease and minimum at around -0.2 to -0.45 V, with a slight shift to the left with decreasing temperature. The nature of this minimum is not yet, fully understood. However, comparison with previous

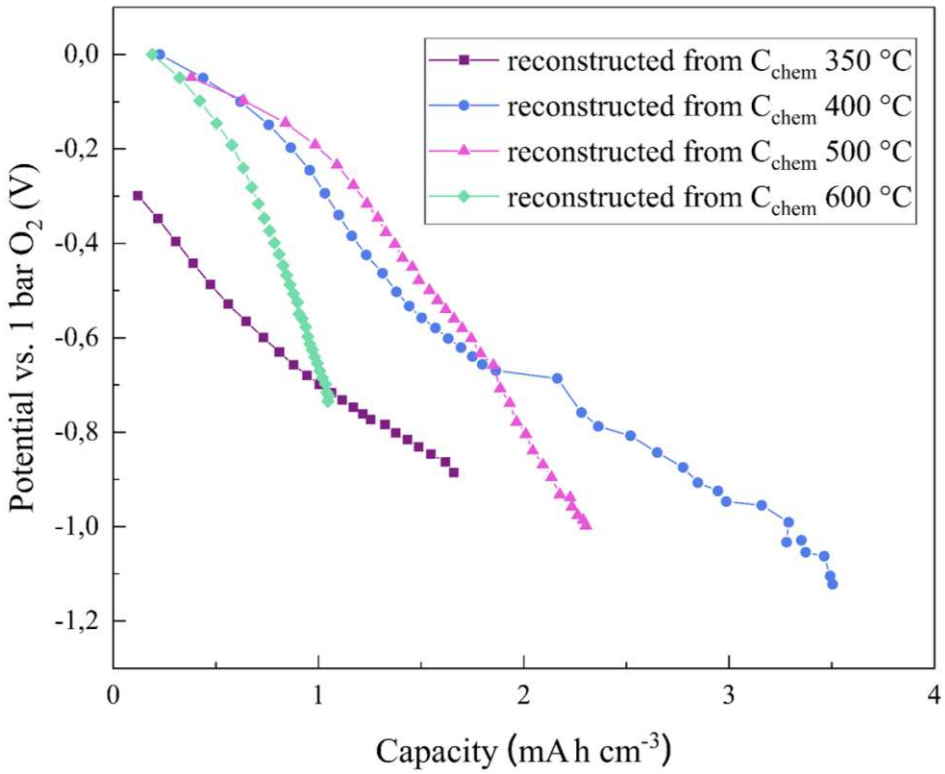

Figure 4.33: Potential vs. capacity curves for a 300 µm GDC microelectrode, from 0 to 900 mV cathodic bias reconstructed from chemical capacitance measurements at different temperatures

scientific papers, indicates, that this could potentially be the intrinsic point of GDC[55],[56]. This would also mean that the already present vacancy concentration in GDC is hardly varied in the potential range under investigation.

EIS Measurements - humidified H2 atmosphere

After the measurements in 1% O_2, a second measurement series in a reducing humidified H_2 atmosphere was carried out. To be able to accurately compare the data sets, the same sample as in the 1% O_2 atmosphere was used. The evaluation of the measured impedance spectra is a current work in progress and will not be included in this work, due to the complexity of the spectra received. Figure 4.34 shows four example spectra at different applied cathodic bias voltages.

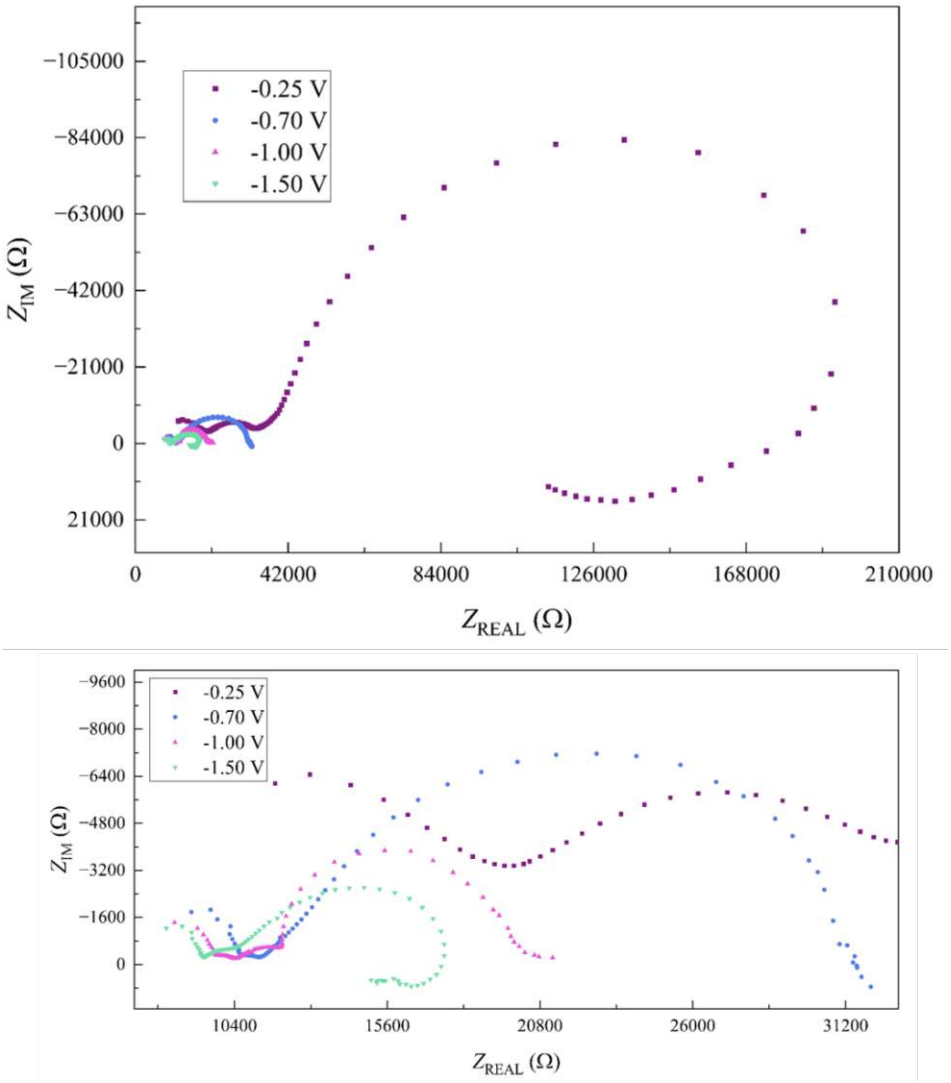

Figure 4.34: Measured impedance spectra of a 300 µm GDC microelectrode under cathodic bias measured in humidified H_2 atmosphere at 600°C. Data points are the measured values.

4.2.4 LNO $La_2NiO_{4+\delta}$

LNO was chosen as a possible electrode material due to its good electronic and ionic conductivity and its ability to be further oxidized[48]. Measurements were conducted in a 1% O_2 atmosphere between 600 and 350 °C. The applied cathodic biases for the measurements ranged from 0 to -1500 mV with -50 mV steps and the anodic biases from 0 to 500 mV, with 50 mV steps.

EIS Measurements

Figures 4.35, 4.36 and 4.37 show the measured impedance spectra (dots) and the respective fit (lines) achieved from the equivalent circuit shown in the inset, for different set voltages and temperatures of LNO samples. Each figure shows six impedance spectra at set voltages of -0.20 V (purple), -0.60 V (blue) -1.20 V (pink) and -1.50 V (teal) for the negative polarizations and +0.25 V (light teal) and +0.50 V (light blue) for the positive polarizations, respectively. The high frequency feature represents the YSZ electrolyte. The medium frequency feature can be attributed to the interface resistance. However, compared to previous measurements, it is small and only becomes visible at lower temperatures. Its visibility also increases with a more anodic polarization and at + 0.50 V at 400 °C it can be determined to be 3 kΩ. The low frequency feature represents the electrode materials chemical capacitance and oxygen exchange resistance. The electrolyte resistance increases from 3.5 kΩ at 600 °C to approximately 250 kΩ at 400 °C and stays constant, no matter, which polarization direction was measured. The low frequency feature again decreases with a both increasing anodic and cathodic polarizations, though much faster with an applied anodic bias. It also increases with a decrease in temperature. Since only the capacitance extracted from the low frequency feature was important, the high and medium frequency features were neglected in the fit and considered together by an R_{offset} resistance. As previously mentioned, the low frequency semi-circle shrinks with an increasingly cathodic bias and its resistance ranges from around 130 kΩ at -0.20 V to 3000 Ω at -1.5 V at 600 °C and 30 kΩ at +0.25 V and 1200 Ω at +0.5 V at 600 °C.

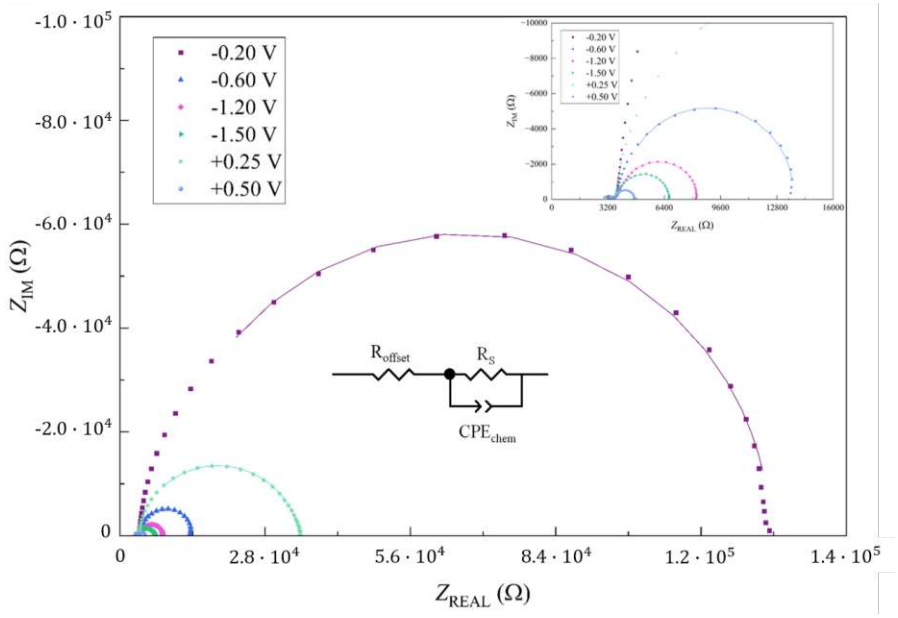

Figure 4.35: Measured impedance spectra of a 300 µm LNO microelectrode under cathodic and anodic bias measured in 1% O_2 atmosphere at 600°C. Data points are the measured values, and the fits are represented by solid lines.

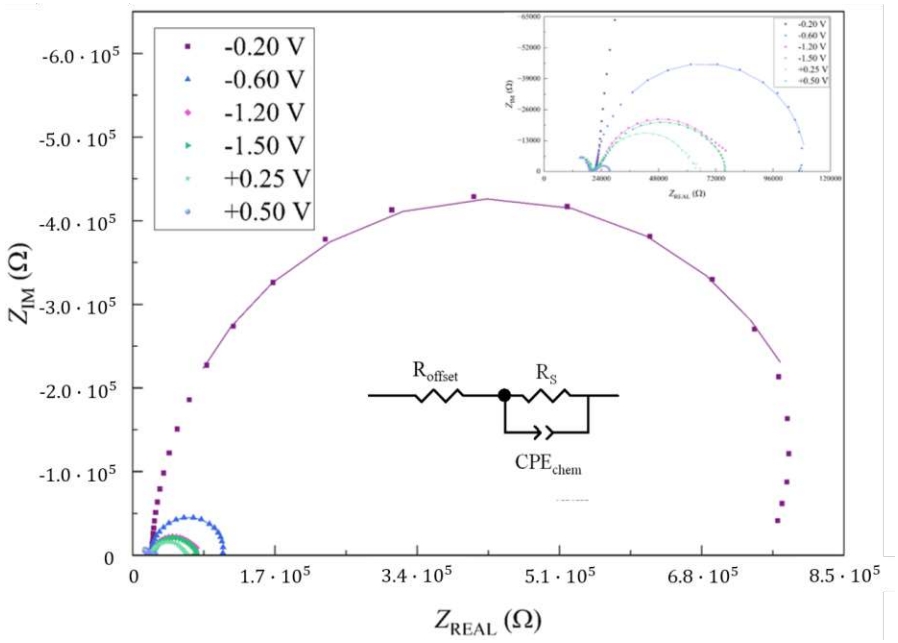

Figure 4.36: Measured impedance spectra of a 300 µm LNO microelectrode under cathodic and anodic bias measured in 1% O_2 atmosphere at 500°C. Data points are the measured values, and the fits are represented by solid lines.

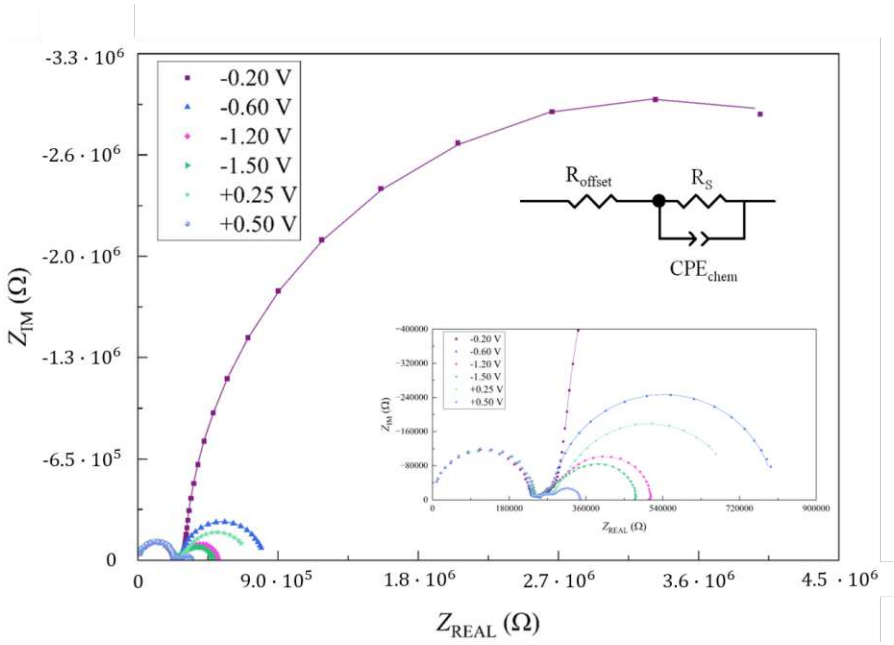

Figure 4.37: Measured impedance spectra of a 300 µm LNO microelectrode under cathodic and anodic bias measured in 1% O_2 atmosphere at 400°C. Data points are the measured values, and the fits are represented by solid lines.

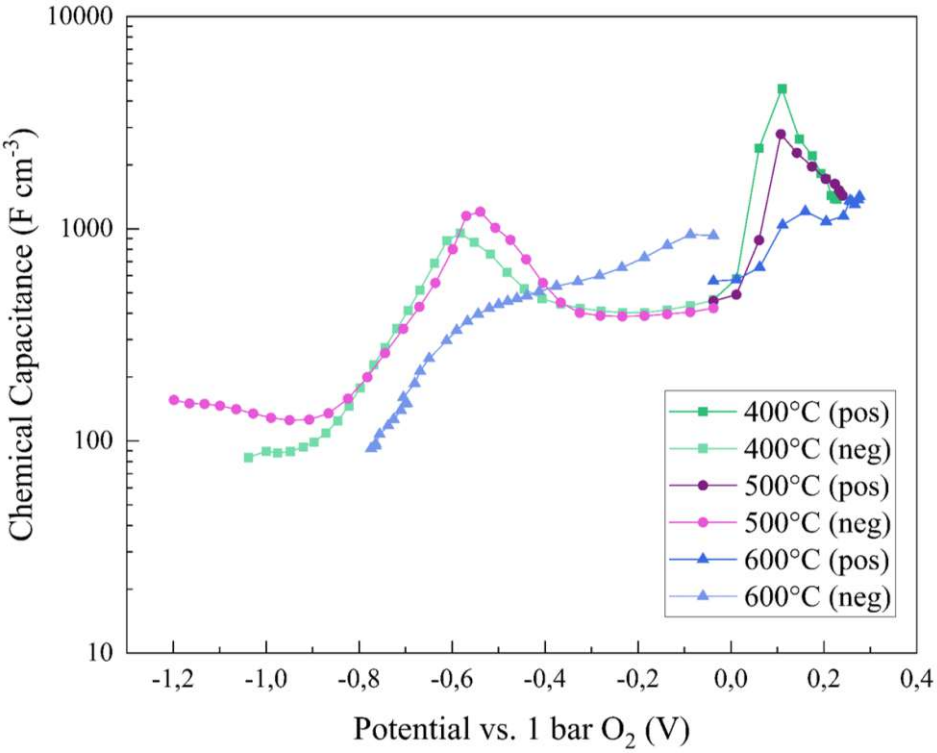

Figure 4.38: Chemical capacitance as a function of the effective electrode overpotential for a 300 µm LNO microelectrode, from 0 to -1200 mV cathodic and 0 to +500 mV anodic bias at different temperatures

Reconstruction of the battery curves

Figure 4.38 shows the chemical capacitance C_{chem} against the potential normalized to 1 bar O_2 and Figure 4.39 the resulting battery curves reconstructed from the corresponding C_{chem} measurements.

LNO can exhibit both oxygen over- and under-stoichiometry. In oxidizing conditions (i.e. anodic overpotential or mildly cathodic overpotentials) the oxygen stoichiometry changes mostly by the creation or annihilation of oxygen interstitials (see Equations (4.16) and (4.17)). This corresponds to a transition from Ni^{2+} to Ni^{3+}.

$$\delta\, O^{2-} + LaNiO_4 \rightleftharpoons LaNiO_{4+\delta} + 2\,\delta e^- \tag{4.16}$$

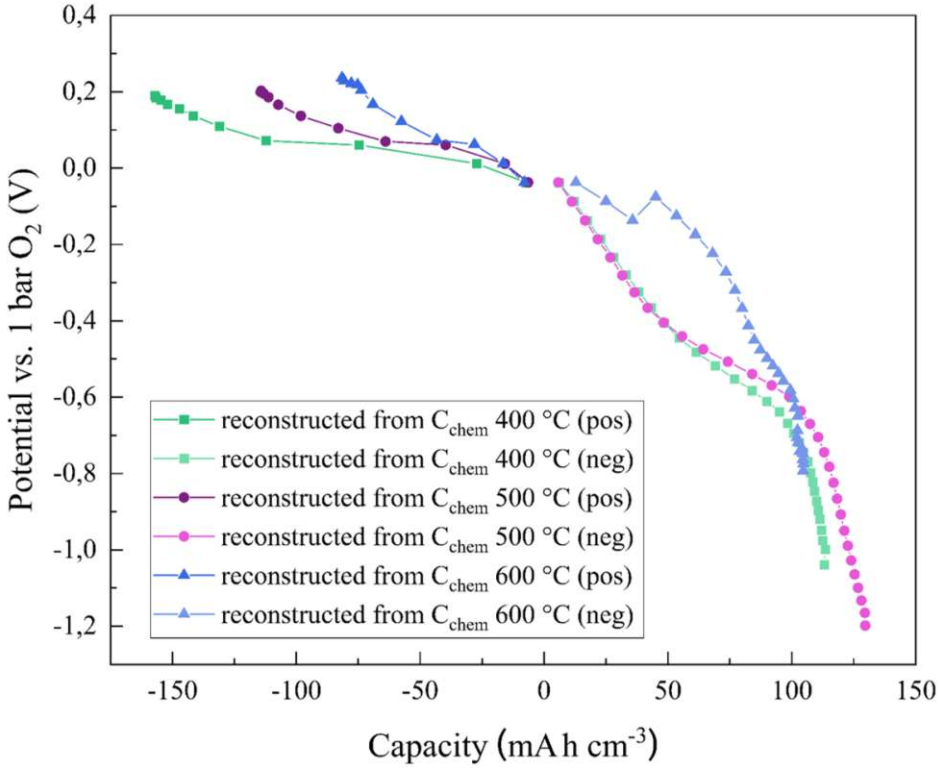

Figure 4.39: Potential vs. capacity curves for a 300 µm LNO microelectrode, from 0 to 900 mV cathodic bias reconstructed from chemical capacitance measurements at different temperatures

$$\delta\, O^{2-} \rightleftharpoons O_i'' + 2\, h^{\cdot} + 2\, e' \tag{4.17}$$

Under reducing conditions (i.e. moderate to high cathodic overpotentials) the oxygen stoichiometry changes are dominated by oxygen vacancy creation and annihilation (see Equations (4.18) and (4.19)) This corresponds to a transition from Ni^{2+} to Ni^{1+}.

$$2\, \delta e^- + LaNiO_4 \rightleftharpoons\ \delta O^{2-} + LaNiO_{4-\delta} \tag{4.18}$$

$$2\, \delta e_{cc}^- + O_O^x \rightleftharpoons\ \delta O_{yte}^{2-} + \delta V_O^{\cdot\cdot} + 2\, \delta e' \tag{4.19}$$

The starting point of the chemical capacitance at -0.039 V to - 0.059 V has values between 422 and 566 F cm^{-3}. For the anodic side, the chemical capacitance rises sharply, with a peak at 0.11 V. However, the higher the temperature, the flatter the peak, with the chemical capacity at the peak reaching 4570 F cm^{-3} for 400 °C, 3371 F cm^{-3} for 500 °C and only 1208 F cm^{-3} for 600 °C. The chemical capacitance at the last measured anodic potential at 0.49 V is similar for all three temperatures and ranges from 1377 F cm^{-3} (400°C), 1432 F cm^{-3} (500°C) and 1370 F cm^{-3} (600 °C). When looking at the cathodic side of the graph, another low temperature feature can be seen in the peaks between 0.51 and 0.58 V. Similar to the anodic side, the peak decreases with a rise in potential and also shows a shift to higher cathodic potentials for higher temperatures. For the 600 °C measurements, the peak is only hinted at. With a rise in cathodic potential, the curves then drop until a minimum of 89 F cm^{-3},

Figure 4.39 shows the capacity in mA h cm^{-3} against the potential normalized to 1 bar O_2. The reference point of the capacity is at -0.039 to -0.059 V for 400, 500 and 600 °C, respectively. Thus, positive voltages lead to nominally negative capacitances. In anodic polarization direction, for the measurements at 400 °C, the capacity reaches up to -154 mA h cm^{-3} at a potential of 0.21 mV, meaning that the electrode can be further charged. For 500 °C and 600 °C this "negative capacity" decreases with an increase in temperature by about 40 mA h cm^{-3} per 100 °C. For cathodic potentials, the measurements reconstructed from the data for 400 °C and 500 °C show a potential drop right at the start of the curve up to -0.45 mV and up to a capacity of 45 mA h cm^{-3}. The curves then reach a small plateau up to about 100 mA h cm^{-3}, before dropping sharply over the course of less than 50 mA h cm^{-3} to a potential of -1.23 V. The curve reconstructed from the 600 °C has slight plateau up to about 50 mA h cm^{-3} at the start, before also showing a potential drop to -0.47 mV. From there on, the curve looks similar to the 400 and 500 °C measurements, with a very small plateau and a final, sharp potential drop to -0.79 mV at a capacity of 117 mA h cm^{-3}.

4.2.5 $YBaCo_4O_{7-\delta}$

$YBCo_4O_7$ was chosen as a possible electrode material due to its high oxygen non-stoichiometry. According to Karppinen et. al. it can absorb oxygen up to δ = 1.5[57] at intermediate temperatures of 270 - 350 °C and release the absorbed oxygen into the atmosphere at temperatures above 400 °C. Bias measurements were conducted to see if this oxygen incorporation and release could not only be achieved chemically, but also electrochemically. Measurements were

performed in a 1% O_2 atmosphere between 350 and 600 °C. The applied cathodic biases for the measurements ranged from 0 to -1500 mV with -50 mV steps. Additionally, an anodic bias, ranging from 0 to 500 mV, with 50 mV steps was applied at 350 °C.

Moreover, a temperature OCV measurement with a temperature range of 250 to 600 °C in 10 °C steps was performed, to see if a change in chemical capacitance could be seen at any point during the heating process.

EIS Measurements

In Figures 4.40, 4.41 and 4.42 the measured impedance spectra (dots) and the respective fit (lines) of $YBaCo_4O_7$, achieved from the equivalent circuit shown in the inset, are shown for different set voltages and temperatures. Figures 4.40 and 4.41 show four impedance spectra at set voltages of -0.20 V (purple), -0.60 V (blue) -1.20 V (pink) and -1.50 V (teal), respectively for the negative polarizations measured at 600 and 400 °C and 4.42 shows six impedance spectra at set voltages of -0.20 V (purple), -0.60 V (blue) -1.20 V (pink) and -1.50 V (teal) for the negative polarization and +0.25 V (light teal) and +0.50 V (light blue) for the positive polarization, respectively. The high frequency arc represents the YSZ electrolyte. The medium frequency feature can be attributed to the interface resistance. However, it is almost fully overlapped by the low frequency feature at all temperatures and bias potentials. The low frequency feature represents the electrode material. The electrolyte resistance increases from 3.25 kΩ at 600 °C to approximately 12 kΩ at 350 °C and stays constant, no matter, which polarization direction was measured. The low frequency feature again decreases with a bias increase both for anodic and cathodic polarizations, and, as for LNO, much faster with an applied anodic bias. It also again increases with a decrease in temperature. Since only the capacitance, that can be extracted from the low frequency feature was important, the high and medium frequency features were neglected in the fit and considered together with an R_{offset} resistance. As previously mentioned, the low frequency semi-circle shrinks with an increasingly cathodic bias and its resistance ranges from around 50 MΩ (-0.20 V, estimated) and 900 kΩ (-1.50 V) at 600 °C and 1.75 GΩ (+0.25 V) to 6.5 MΩ (+0.50 V) at 350 °C.

There are also other electrochemical phenomena that can appear in the spectra as a third or even fourth semi-circle, either between the electrolyte and electrode features, or at the very end of the spectrum as a very low frequency feature. However, their nature is not fully understood yet and their interpretation was not attempted. Those do not affect the main low frequency semi-circle or the chemical capacitance C_{chem}.

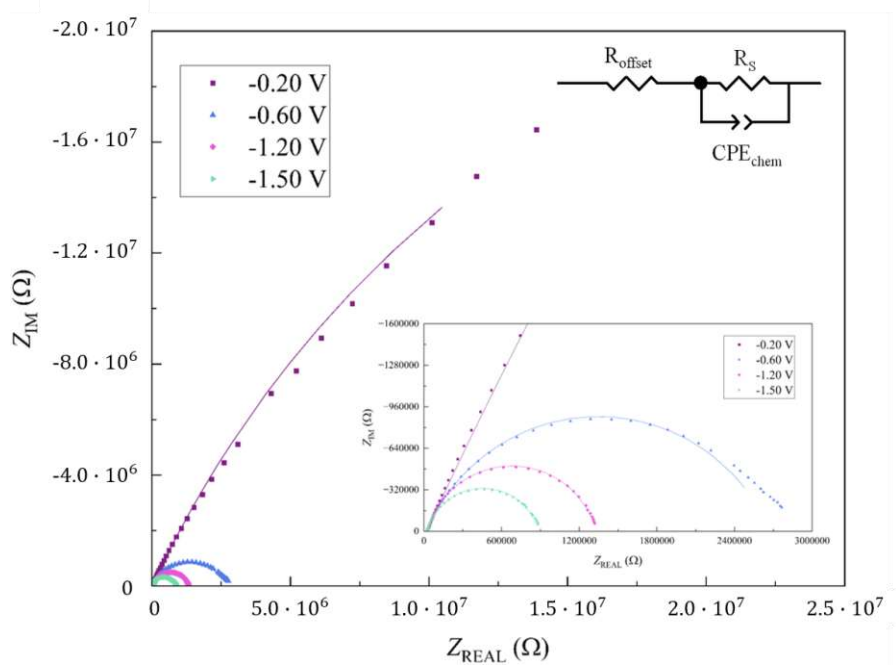

Figure 4.40: Measured impedance spectra of a 300 µm $YBaCo_4O_7$ microelectrode under cathodic bias measured in 1% O_2 atmosphere at 600°C. Data points are the measured values, and the fits are represented by solid lines.

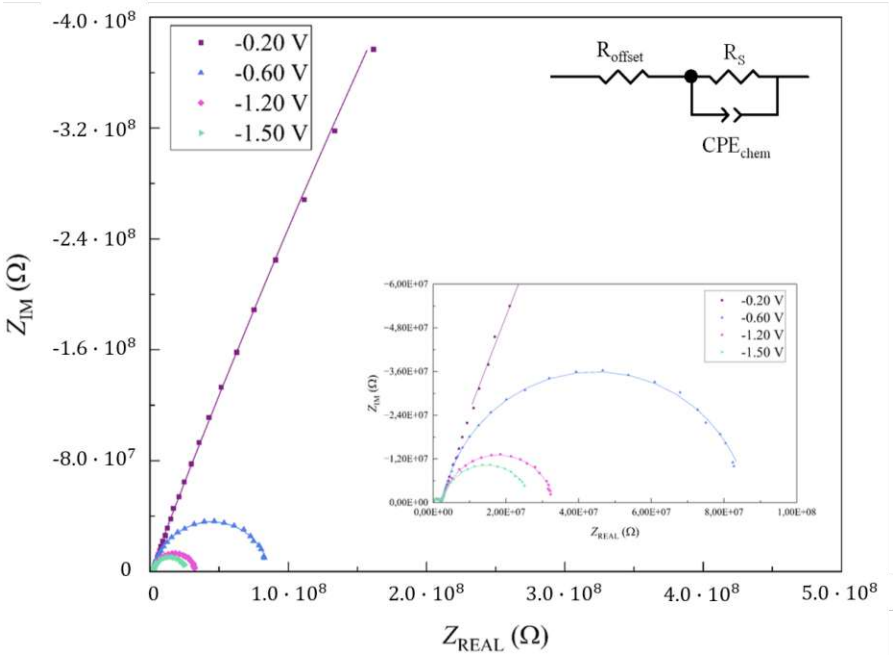

Figure 4.41: Measured impedance spectra of a 300 µm $YBaCo_4O_7$ microelectrode under cathodic bias measured in 1% O_2 atmosphere at 400°C. Data points are the measured values, and the fits are represented by solid lines.

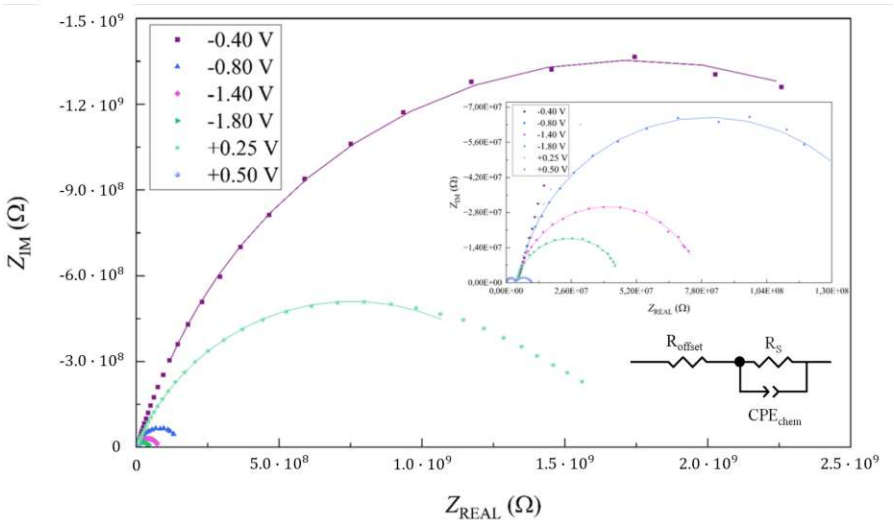

Figure 4.42: Measured impedance spectra of a 300 µm $YBaCo_4O_7$ microelectrode under cathodic and anodic bias measured in 1% O_2 atmosphere at 500°C. Data points are the measured values, and the fits are represented by solid lines.

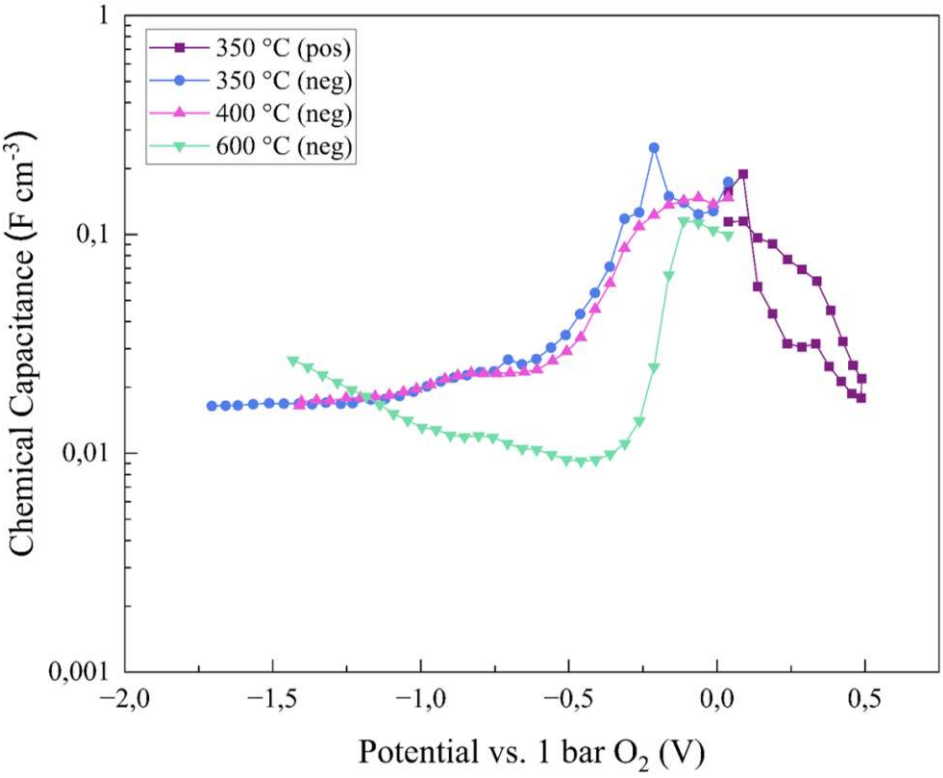

Figure 4.43: Chemical capacitance as a function of the effective electrode overpotential for a 300 µm $YBaCo_4O_7$ microelectrode, from 0 to -1800 mV cathodic and 0 to +500 mV anodic bias at different temperatures

Figure 4.43 shows the chemical capacitance as a function of the effective electrode overpotential for the $YBaCo_4O_7$ measurements in the temperature range from 350 to 600 °C. Although literature states the oxygen non-stoichiometry is one of the highest in ceramic oxides, no appreciable chemical capacitance could be measured at any bias or temperature. It was not possible to electrochemically reduce or oxidize the material. No OIB battery curve of the material was reconstructed and the material was therefore concluded to be not suitable for the usage as an electrode in OIBs.

Temperature spectra without bias voltage were measured between 300 and 600 °C in 1% O_2 to see if any significant chemical capacitance can be measured at any temperature in this range. Figure 4.44 shows the chemical capacitance as a function of the temperature. Similar to the measurements with applied biases, no significant chemical capacitance could be measured at any given temperature.

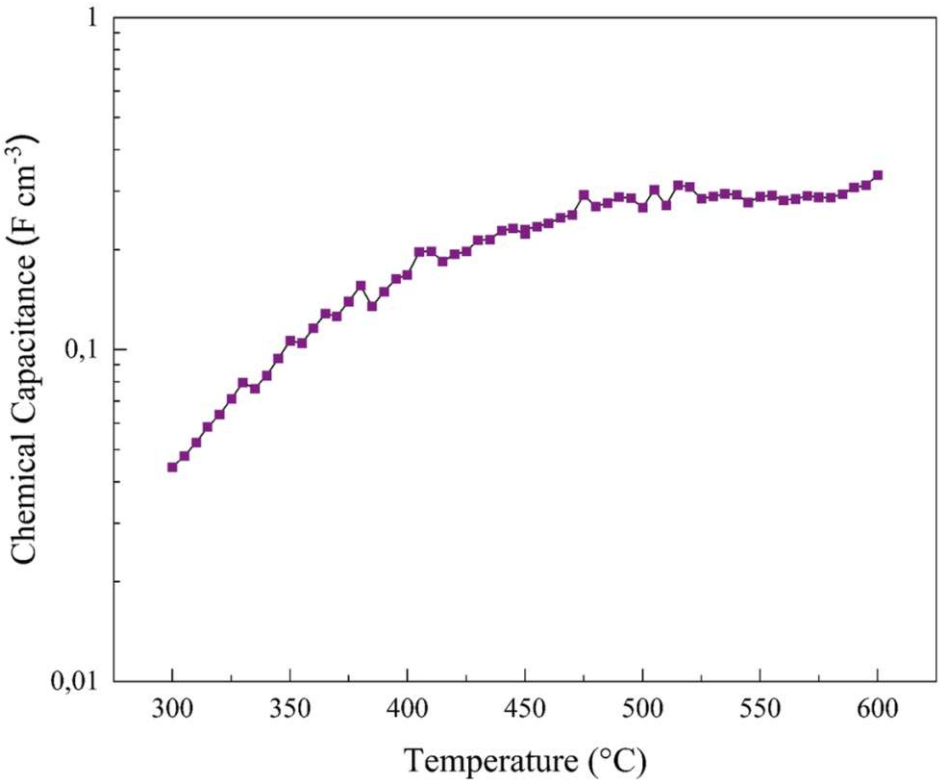

Figure 4.44: Chemical capacitance as a function of the temperature for a 300 µm $YBaCo_4O_7$ microelectrode, ranging from 300 to 600 °C

4.2.6 STO $SrTiO_3$

STO was chosen as a possible elctrode material due to its well known defect chemistry and its already widespread usage as a material in other applications such as solar cells[50]. First measurements were conducted in a 1% O_2 atmosphere and in humidified H_2 at 500 °C to see if STO could be viable for more detailed testing. The applied cathodic biases for the measurements ranged from 0 to -1500 mV with -50 mV steps.

EIS Measurements

Figures 4.45 shows the measured impedance spectra (dots) and the respective fit (lines) of STO for an applied cathodic bias from 0 to -2000 mV in -50 mV steps at 500 °C in a 1% O_2 atmosphere and Figures 4.46 and 4.47 show the measured impedance spectra (dots) and the respective fit (lines) of STO for an applied cathodic bias from 0 to -1500 mV in -50 mV steps for the first

measurement and from -1400 to -2000 mV in -50 mV steps at 500 °C in humidified H_2 atmosphere. At high frequency and under significant applied cathodic bias, the last semi-circle feature curves inwards, leading to a kind of "inductive" loop at the lowest frequencies. This inductive loop appearing with an increasing anodic biases, has been observed before and has been determined to be fully reversible in its nature and identified as a frequency-dependent change of the stoichiometric polarization within the layers[58].

- 500 °C - 1% O_2 Atmosphere

  Figure 4.45 shows four impedance spectra at set voltages of -0.40 V (purple), -0.80 V (blue) -1.50 V (pink) and -2.00 V (teal), respectively for negative polarizations, measured at 500 °C. The resistance of the electrolyte R_{YSZ} at this temperature is approximately 30 Ω for all voltages. The interface resistance R_{inter} is overlapped by the low frequency semi-circle for all spectra. The low frequency semi-circle, from which the chemical capacitance C_{chem} can be fitted, shrinks with a potential increase. However, at an applied voltage of -2000 mV it again increases compared to the -1500 mV applied bias. The corresponding resistances range from around 60 kΩ (purple) to 40 kΩ (pink). The high frequency semi-circles also seem to curve inwards, forming a spiral shape, with positive Z_{IM} at the lowest frequencies and at -1500 mV and -2000 mV, the spectra show even a fourth feature emerging between the large third and the spiral shaped features.

- 500 °C humidified H_2 atmosphere 1st measurement

  Figure 4.46 shows four impedance spectra at set voltages of -0.20 V (purple), -0.60 V (blue) -1.20 V (pink) and -1.50 V (teal), respectively for negative polarizations, measured at 500 °C. The resistance of the electrolyte R_{YSZ} at this temperature is approximately 30 Ω for all voltages, however a sharp distinction of R_{YSZ} is only possible for the highest polarization. For all other spectra, it seems that the electrolyte resistance is partially overlapped by a second semi-circle feature, which sharply decreases with an increasing polarization. The exact nature of this resistance is unclear but it was determines that it is not the semi-circle containing information on the chemical capacitance of the electrode. Once this second feature shrinks, a third semi-circle is revealed at -1200 mV. This feature was also used to determine the chemical capacitance values. The resistances of this third semi circle range from around 550 kΩ (pink) to 300 kΩ (pink). Again, the high frequency semi-circles seem to curve inwards, in an "inductive" loop, at the lowest frequencies for a higher polarization.

- 500 °C humidified H_2 atmosphere 2nd measurement

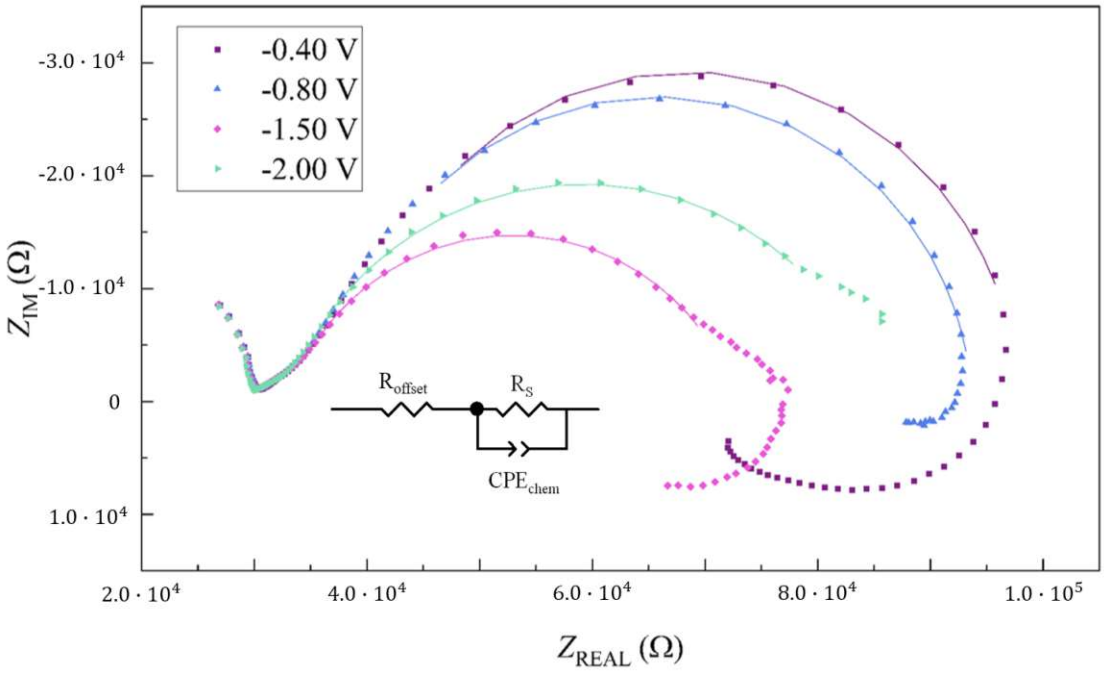

Figure 4.45: Measured impedance spectra of a 300 µm STO microelectrode under cathodic bias measured in 1 % O_2 atmosphere at 500°C. Data points are the measured values, and the fits are represented by solid lines.

Figure 4.47 shows four impedance spectra at set voltages of -1.40 V (purple), -1.60 V (blue) -1.80 V (pink) and -2.00 V (teal), respectively for negative polarizations, measured at 500 °C. This measurement was performed as a follow up after the polarization up to -1500 mV to further investigate the behaviour of STO under bias. The resistance of the electrolyte R_{YSZ} at this temperature was also approximately 30 Ω for all voltages. The previously observed second semi-circle feature, continues to decrease with an increasing polarization. The same holds for third semi-circle feature. At a cathodic bias of -2000 mV, both features almost completely vanish. Again, the high frequency semi-circles seem to curve inwards, in the aforementioned "inductive" loop. This loop also decreases in size with an increasing bias, however, even at -2000 mV it is well defined and visible.

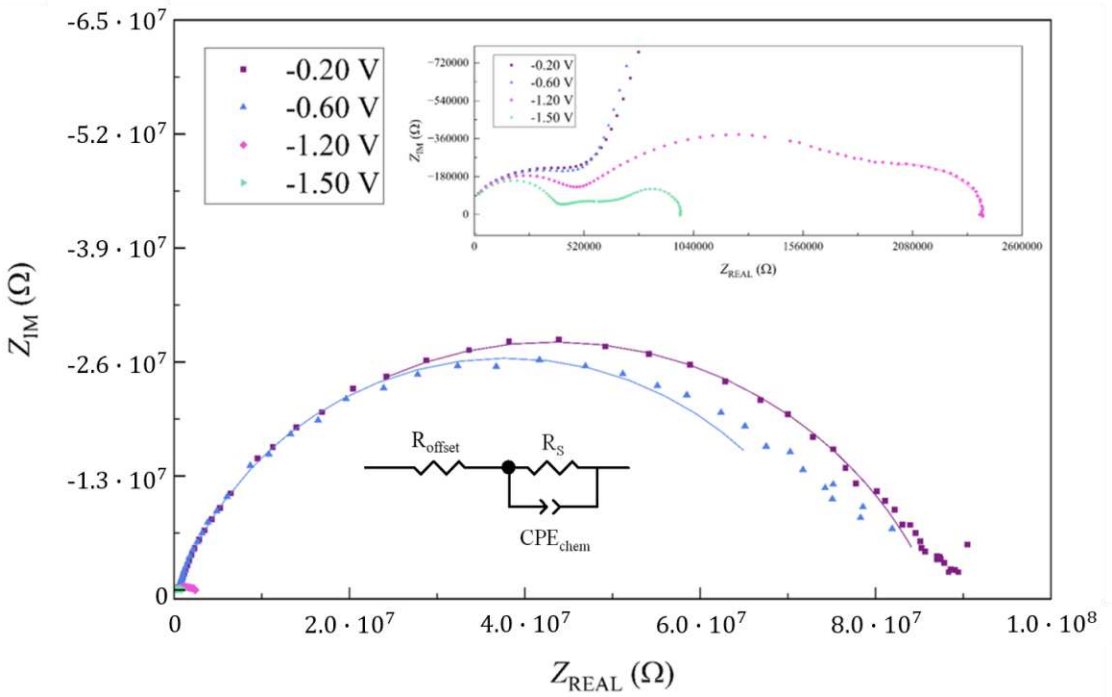

Figure 4.46: Measured impedance spectra of a 300 µm STO microelectrode under cathodic bias measured in humidified H_2 atmosphere at 500°C. Data points are the measured values, and the fits are represented by solid lines.

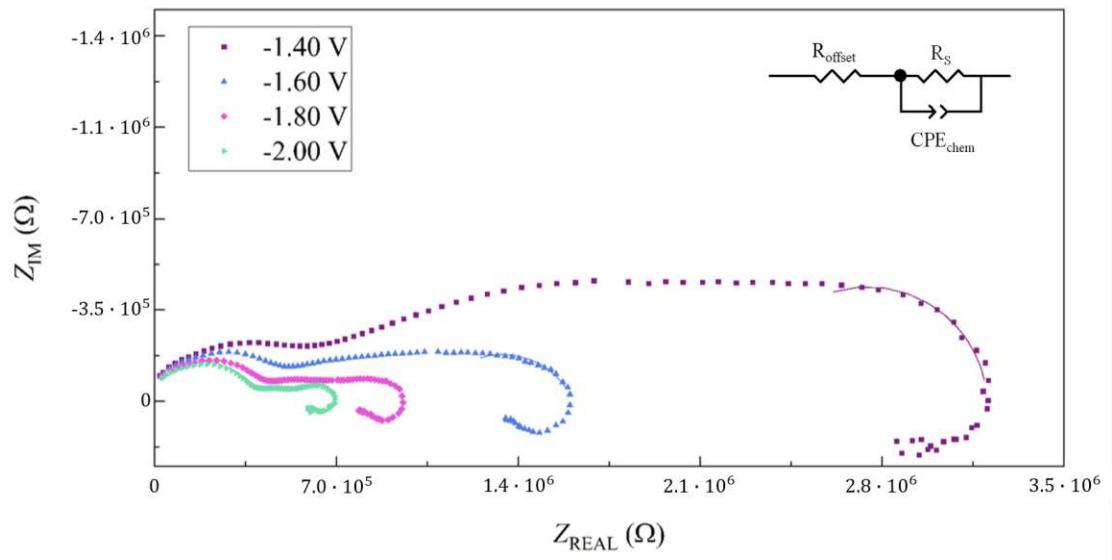

Figure 4.47: Measured impedance spectra of STO for different set voltages at 500 °C in humidified H_2 atmosphere with set voltages from from -1350 to -2000 mV

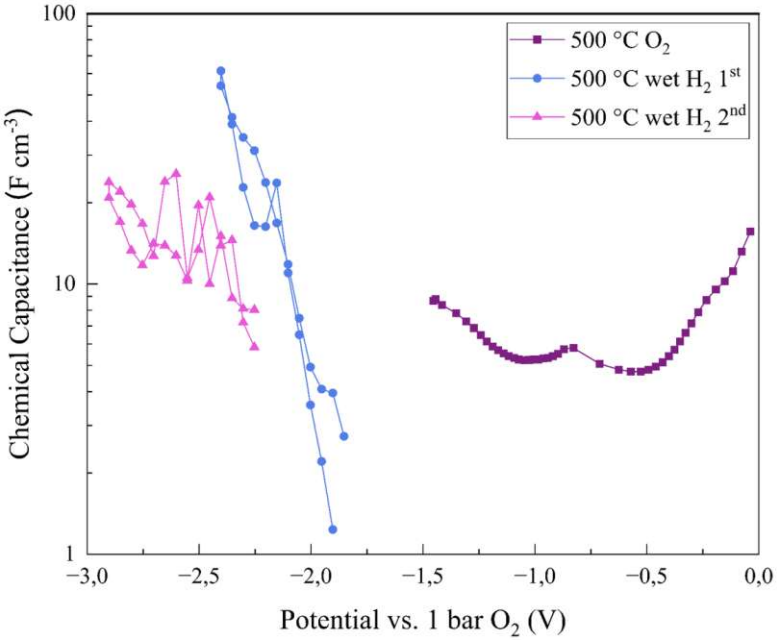

Figure 4.48: Chemical capacitance as a function of the effective electrode overpotential for a 300 µm STO microelectrode at 500 °C in 1% O_2 (purple) and humidified H_2 atmosphere (blue, pink) with set voltages from from 0 to -2000 mV

Reconstruction of the battery curves

$$O_O^x + 2\,Ti_{Ti}^x + 2\,e_{cc}^- \rightleftharpoons O_{yte}^{2-} + V_O^{\cdot\cdot} + 2 + 2\,Ti_{Ti}' \tag{4.20}$$

Figure 4.48 and 4.49 show the chemical capacitance as a function of the effective electrode overpotential and the reconstructed battery curves for the STO measurements at 500 °C for cathodic biases ranging from 0 to - 2000 mV. These first measurements suggests that there might be potential for higher chemical capacitance values at lower bias values. However, based on the reaction this could not successfully be investigated with the used sample architecture. A new sample architecture was proposed with microelectrodes directly on the YSZ electrolyte and a planar current collector on top of it, instead of a current collector grid between the electrode and electrolyte layers. The adapted sample architecture can be seen in Figure 4.50. Measurements, however, are still to be done.

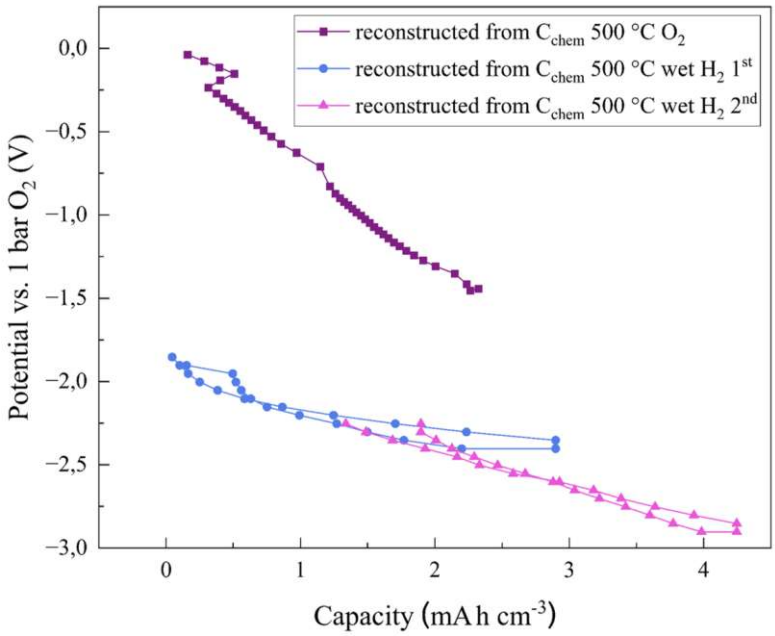

Figure 4.49: Potential vs. capacity curves for a 300 µm STO microelectrode, from 0 to -3000 mV cathodic bias reconstructed from chemical capacitance measurements at different temperatures

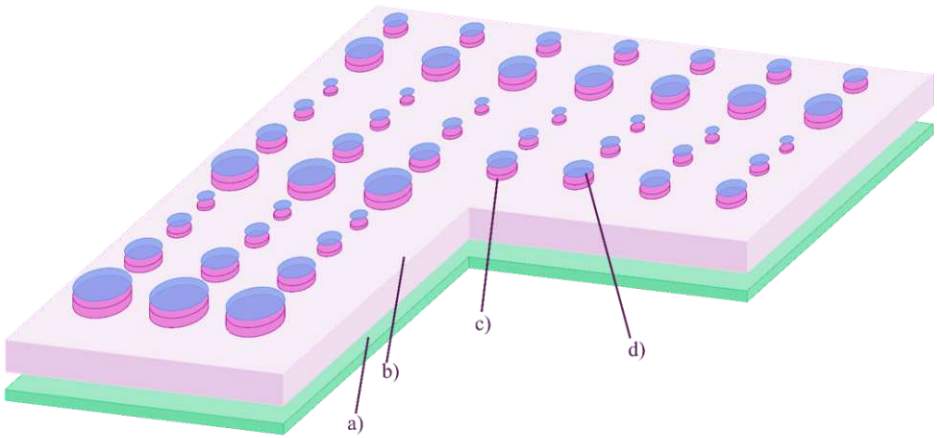

Figure 4.50: Alternative 3D sample architecture for future GDC and STO measurements with a) the LSC counter elctrode, b) the YSZ electrolyte c) the micro working electrodes in different sizes and d) the Pt/Ti current collector grid.

4.2.7 LCF $La_{0.8}Ca_{0.2}FeO_{3-\delta}$

LCF was chosen as a possible electrode material due to its similaries to LSF. Like LCF, it is an A-site acceptor-doped perovskite-type MIEC and changes it's electronic properies with the $Fe^{4+}/Fe^{3+}/Fe^{2+}$ ratio. The sample preparation is finished and measurements are currently underway.

4.3 Comparison

So far, we can conclude that particularly LSF, LSCrMn and LNO are very promising candidates as electrode materials for oxygen ion batteries. Their charging characteristics at 400 °C are summarized and compared in Figure 4.51.

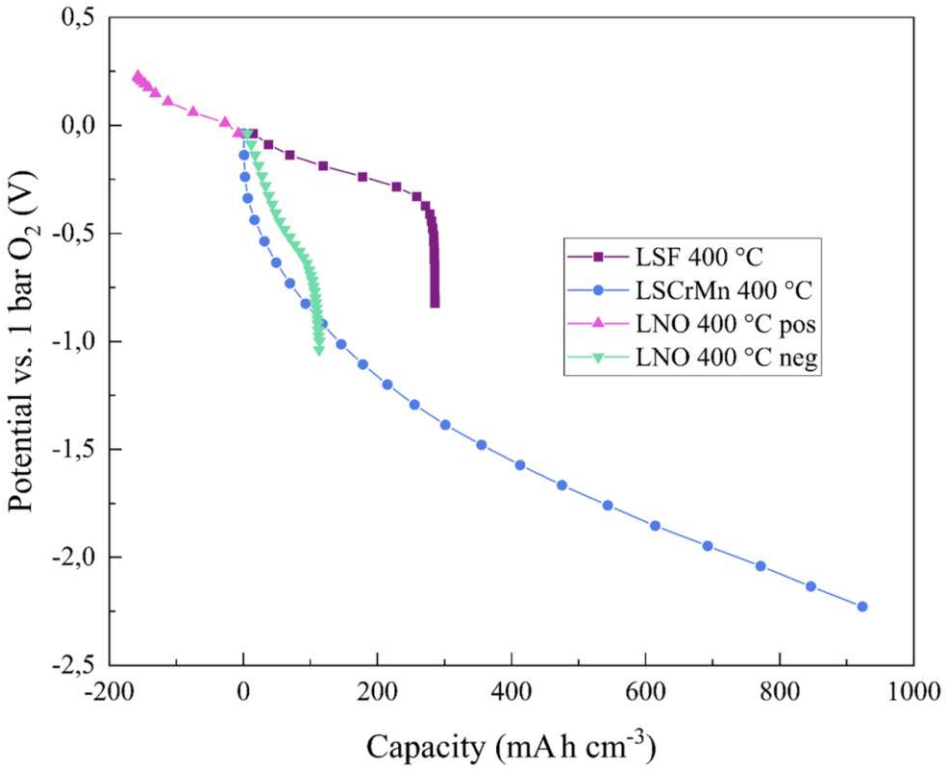

Figure 4.51: Comparison of the capacities of LSF, LSCrMn and LNO at 400 °C

5 Summary and Outlook

Thin film microelectrodes with a diameter of 300 μm were prepared by pulsed laser deposition on YSZ single crystals. The microelectrodes consist of $La_{0.6}Sr_{0.4}FeO_{3-\delta}$ (LSF), $La_{0.5}Sr_{0.5}Cr_{0.2}Mn_{0.8}O_{3-\delta}$ (LSCrMn), Gd:CeO_2 (GDC), $La_2NiO_{4+\delta}$ (LNO), $YBaCo_4O_{7-\delta}$ ($YBCo_4O_7$), $SrTiO_3$ (STO) or $La_{0.8}Ca_{0.2}FeO_{3-\delta}$ (LCF). Between electrode and electrolyte layer a Pt/Ti current collector grid was added by sputter deposition and lift off lithography to ensure a uniform polarization of the microelectrodes. The morphology of all prepared samples was investigated with an optical microscope and a SEM. Impedance spectroscopy was then used for the electrochemical characterization of the thin films. Measurements were done with different polarizations (anodic and cathodic), in different atmospheres (oxidizing - 1% O_2 and reducing - humidified H_2) and at different temperatures (350 - 600 °C) to investigate the effects of polarization, atmosphere and temperature on the chemical capacitance of the thin film electrodes. The chemical capacitance C_{chem} was extracted from Electrochemical Impedance Spectroscopy (EIS) data. Battery capacities Q_{bat} are then calculated by integrating C_{chem} and the Oxygen Ion Battery (OIB) battery curve could thus be reconstructed. Properties of LSF and LSCrMn were found to be in agreement with previously measured DC measurements, conducted at 500 °C in a limited voltage range. LSF displayed good temperature and bias stability with capacity values up to 300 $mA\ h\ cm^{-3}$. LSCrMn showed outstandingly high capacity values of up to 1200 $mA\ h\ cm^{-3}$ at 350 °C and 900 $mA\ h\ cm^{-3}$ at 400 °C at potentials as low as -2450 mV vs. 1 bar O_2. At 600 °C and 500 °C, up to 300 $mA\ h\ cm^{-3}$ at -1000 mV were reached. LNO was able to be polarized in both cathodic and anodic direction, with total capacities up to 350 $mA\ h\ cm^{-3}$ and a good consistency across the measured temperature range. These three in particular have been determined to be good candidates for further investigation as electrodes in oxygen ion batteries.

$YBaCo_4O_7$, although expected to possess a very high oxygen non-stoichiometry, based on literature data, could not be reduced or oxidized electrochemically. Only very small chemical capacitance values were found for all different temperatures and bias voltages. This material was therefore deemed to be not suitable as a possible electrode material in OIBs.

Although, with a thin film microelectrode architecture, STO and GDC did not show very high

chemical potentials, they do show potential for possible high chemical capacitance values with a different sample architecture. They were both measured in 1% O_2 and humidified H_2 atmospheres, which resulted in complex spectra with multiple features, that are not fully understood yet. The proposed new sample architecture for these two materials also uses microelectrodes to be able to neglect the influence of the counter electrode on the impedance spectra, but the Pt/Ti current collector for this architecture is no longer in a grid between electrode and electrolyte, but a planar layer on top of the electrode instead. The sample preparatin for STO is finished and measurements are planned in the near future.

Danksagungen

Es ist ein ganz eigenartiges Gefühl, als allerletzten Absatz eine Danksagung zu verfassen. Letztes Jahr im Oktober, als das "Abenteuer Masterarbeit" begonnen hat, schien das noch in unendlicher Ferne zu liegen, aber letztendlich ist jetzt doch die Zeit dafür. Als allererstes möchte ich mich bei meinen Betreuern, Martin Krammer und besonders Alex Schmid, bedanken. Für die Zusage, eine unbekannte Studentin, als Diplomandin anzunehmen. Für die unendliche Geduld und das immer und immer wieder erklären mancher Dinge, so lange, bis ich es verstanden habe. Für's Übermitteln, dass es keine "zu blöden" Fragen gibt. Für die Ideen, wenn ich nicht weiter wusse. Für das gute Zureden und ganz allgemein für die Unterstützung von Anfang bis Ende. Großer Dank gilt auch Prof. Jürgen Fleig, für das Vertrauen und die Möglichkeit, dass ich in seiner Gruppe meine Diplomarbeit machen durfte. Natürlich hätte das alles nicht so gut geklappt, gäbs da nicht die ganze Arbeitsgruppe, die mich von Tag 1 an, herzlich empfangen hat und mit ganz viel Hilfsbereitschaft und Freundlichkeit nicht nur das Einleben sehr erleichtert hat, sondern auch "die Arbeit" zu einem Ort gemacht hat, an den ich jeden einzelnen Tag gerne hin gegangen bin. Besonders hervorheben möchte ich an dieser Stelle meine drei Bürokollegen - Alex, Claudia und Kirsten - mit denen es nie langweilig wurde, ganz viel Schoko geteilt wurde, ein ganzes ElchiUniverse entstanden ist und die drei der Gründe sind, warum ich mich letzten Endes doch dafür entschieden habe, ein Doktorat zu beginnen. An der Stelle auch nochmal ein extra Danke an Kirsten, für's Aufnehmen der tollen SEM Bilder, die in der Arbeit zu sehen sind, und Claudia für die Grazing Incidence Messungen, auch wenn die es dann doch nicht geschafft haben. :-)

Abgesehen von der Arbeitsgruppe möchte ich mich natürlich auch bei meiner Familie bedanken, ohne deren Unterstützung ich nie die Möglichkeit gehabt hätte, ein Studium überhaupt zu beginnnen - auch wenn manchmal das Ziel der Reise nicht immer ganz so klar war, wie jetzt. Wahrscheinlich ist an dieser Stelle auch eine Entschuldiung angebracht, für die vorallem nächtlichen, verweinten, verzweifelten Anrufe, vor verschiedensten Prüfungen (insbesondere vor Organikprüfungen...), dass eh alles egal ist und ich mit meinem Studium aufhöre. Danke Mama! Danke Papa! Danke Nico! Danke Opa und Oma (auch wenn du nicht mehr da bist)!

Last but not least - möchte ich mich bei meinen Freunden bedanken. Bei Niki, Maddie und Lisa, die sich mit mir durchs organisatorische Master-Dickicht gekämpft haben und die's, trotz Beginn am Höhepunkt der Covidpandemie, zu einer richtig coolen Zeit gemacht haben, die ich nicht missen möchte. Bei Anna, Flo[2], Mina, Romi, Vicky, Christian, Beidong, Nina und allen anderen (bitte fühlt euch an dieser Stelle angesprochen <3) die mich nun schon seit dem Bachelor begleiten, für all die tollen Jahre - die Spieleabende, die Reisen, die DnD Gruppe, die Höhen, die Tiefen, die Motivation bei Lernsessions - das ganze Paket halt - und hoffentlich noch viele weitere. :-)

Abbreviations

CE Counter Electrode. 22

CPE Constant Phase Element. 18, 52

EIS Electrochemical Impedance Spectroscopy. ii, iii, 15, 90

GDC Gd:CeO_2. ii, iii, 4, 33, 66, 90

GID Grazing Incidence Diffraction. 35

LCF $La_{0.8}Ca_{0.2}FeO_{3-\delta}$. ii, iii, 5, 33, 89, 90

LIB Lithium Ion Battery. 15

LNO $La_2NiO_{4+\delta}$. ii, iii, 6, 33, 73, 90

LSC $La_{0.6}Sr_{0.4}CoO_{3-\delta}$. 10, 32

LSCrMn $La_{0.5}Sr_{0.5}Cr_{0.2}Mn_{0.8}O_{3-\delta}$. ii, iii, 5, 28, 33, 58, 90

LSF $La_{0.6}Sr_{0.4}FeO_{3-\delta}$. ii, iii, 5, 28, 33, 39, 90

MIEC Mixed Ionic Electronic Conductor. ii, iii, 5, 51, 54

OIB Oxygen Ion Battery. 1, 5, 90

PI-MOCVD Pulsed-Injection Metalorganic Chemical Vapor Deposition. 30

PLD Pulsed Laser Deposition. 32, 38

QCM Quartz Crystal Microbalance. 38

SEM Secondary Electron Microscope. 35, 38, 90

SOEC Solid Oxide Electrolysis Cells. ii, iii, 4

SOFC Solid Oxide Fuel Cells. ii, iii, 4

STO $SrTiO_3$ Strontium Titanate. ii, iii, 5, 33, 83, 90

WE Working Electrode. 22

XRD X-Ray Diffraction. 35, 38

$YBCo_4O_7$ $YBaCo_4O_{7-\delta}$. ii, iii, 33, 35, 78, 90

YSZ Yttrium stabilized Zirconia. ii, iii, 27, 39

Bibliography

[1] J. Kotcher, E. Maibach, and W. T. Choi. "Fossil fuels are harming our brains: Identifying key messages about the health effects of air pollution from fossil fuels". In: *BMC Public Health* 19 (Aug. 2019), p. 1097. DOI: 10.1186/s12889-019-7373-1.

[2] F. Martins, C. Felgueiras, M. Smitkova, and N. Caetano. "Analysis of fossil fuel energy consumption and environmental impacts in european countries". In: *Energies* 12 (2019), p. 964. DOI: 10.3390/en12060964.

[3] F. P. Perera. "Multiple threats to child health from fossil fuel combustion: Impacts of air pollution and climate change". In: *Environmental Health Perspectives* 125 (Feb. 2017), pp. 141–148. DOI: 10.1289/EHP299.

[4] M. Höök and X. Tang. "Depletion of fossil fuels and anthropogenic climate change-A review". In: *Energy Policy* 52 (Jan. 2013), pp. 797–809. DOI: 10.1016/j.enpol.2012.10.046.

[5] O. Edenhofer, R. P. Madruga, Y. Sokona, U. N. E. Programme., W. M. Organization., I. P. on Climate Change. Working Group III., and P.-I. für Klimafolgenforschung. *Renewable energy sources and climate change mitigation : special report of the Intergovernmental Panel on Climate Change*. Cambridge University Press, 2012. ISBN: 9781107607101.

[6] Y. Yang, S. Bremner, C. Menictas, and M. Kay. "Battery energy storage system size determination in renewable energy systems: A review". In: *Renewable and Sustainable Energy Reviews* 91 (Aug. 2018), pp. 109–125. DOI: 10.1016/j.rser.2018.03.047.

[7] W. Wang, B. Yuan, Q. Sun, and R. Wennersten. "Application of energy storage in integrated energy systems — A solution to fluctuation and uncertainty of renewable energy". In: *Journal of Energy Storage* 52 (Aug. 2022), p. 104812. DOI: 10.1016/j.est.2022.104812.

[8] S. O. Amrouche, D. Rekioua, T. Rekioua, and S. Bacha. "Overview of energy storage in renewable energy systems". In: *International Journal of Hydrogen Energy* 41 (Dec. 2016), pp. 20914–20927. DOI: 10.1016/j.ijhydene.2016.06.243.

[9] T. P. Narins. "The battery business: Lithium availability and the growth of the global electric car industry". In: *Extractive Industries and Society* 4 (Apr. 2017), pp. 321–328. DOI: 10.1016/j.exis.2017.01.013.

[10] A. Schmid, M. Krammer, and J. Fleig. "Rechargeable Oxide Ion Batteries Based on Mixed Conducting Oxide Electrodes". In: *Advanced Energy Materials* 13 (Mar. 2023), p. 2203789. DOI: 10.1002/aenm.202203789.

[11] C. Kittel. *Introduction to Solid State Physics*. Wiley, 1953. ISBN: 978-1-119-45416-8. DOI: 10.1119/1.1974177.

[12] J. R. Hook and H. E. Hall. *Solid state physics*. 2nd ed. The Manchester Physics Series. Wiley, 1991. ISBN: 0-471-92805-4.

[13] J. P. Goff, W. Hayes, S. Hull, M. T. Hutchings, and K. N. Clausen. "Defect structure of yttria-stabilized zirconia and its influence on the ionic conductivity at elevated temperatures". In: *The American Physical Society* 59 (1999), pp. 14202–14219.

[14] M. Yoshimura. "Phase Stability of Zirconia Soft Solution Processing for 2D materials, Graphene, MXene, etc. and their hybrids". In: *Ceramic Bulletin* 67 (1988), pp. 1950–1955.

[15] J. Kondoh, H. Shiota, K. Kawachi, and T. Nakatani. "Yttria concentration dependence of tensile strength in yttria-stabilized zirconia". In: *Journal of Alloys and Compounds* 365 (Feb. 2004), pp. 253–258. DOI: 10.1016/S0925-8388(03)00640-6.

[16] J. B. Goodenough, N. Orlovskaya, and N. Browning. *Mixed Ionic Electronic Conducting Perovskites for Advanced Energy Systems*. 1st ed. Nato Science Series 173. Springer, 2004. ISBN: 978-1-4020-1944-9,978-1-4020-2349-1. DOI: 10.1007/978-1-4020-2349-1.

[17] M. Kuhn, S. Hashimoto, K. Sato, K. Yashiro, and J. Mizusaki. "Oxygen nonstoichiometry, thermo-chemical stability and lattice expansion of La0.6Sr0.4FeO3-δ". In: *Solid State Ionics* 195 (July 2011), pp. 7–15. DOI: 10.1016/j.ssi.2011.05.013.

[18] X. Xu, Y. Pan, Y. Zhong, R. Ran, and Z. Shao. "Ruddlesden-Popper perovskites in electrocatalysis". In: *Materials Horizons* 7 (July 2020), pp. 2519–2565. DOI: 10.1039/d0mh00477d.

[19] W. Kleber, H.-J. Bautsch, and J. Bohm. *Einführung in die Kristallographie*. Oldenburg Verlag, 2010. ISBN: 978-3-11-046023-0. DOI: 10.1515/9783110460247.

[20] W. Fowler. *Point Defects*. Ed. by F. Bassani, G. L. Liedl, and P. Wyder. Elsevier, 2005. ISBN: 978-0-12-369401-0. DOI: https://doi.org/10.1016/B0-12-369401-9/00412-5.

[21] R. J. D. Tilley. *Defects in Solids*. Wiley, 2008. ISBN: 9780470077948. DOI: 10.1002/9780470380758.

[22] H.-J. Bargel and G. Schulze. *Werkstoffkunde*. Ed. by H.-J. Bargel and G. Schulze. Springer Berlin Heidelberg, 2008. ISBN: 978-3-540-79296-3. DOI: 10.1007/978-3-540-79297-0.

[23] A. J. Moulson and J. M. Herbert. *Electroceramics: Materials, Properties, Applications*. Wiley, 2003. ISBN: 0471497479. DOI: 10.1002/0470867965.

[24] F. A. Kröger and H. J. Vink. "Relations between the Concentrations of Imperfections in Crystalline Solids". In: *Journal of Physics C: Solid State Physics* 3 (1956), pp. 307–435. DOI: 10.1016/S0081-1947(08)60135-6.

[25] H. Schmalzried and F. A. Kröger. "The Chemistry of Imperfect Crystals". In: *Berichte der Bunsengesellschaft für physikalische Chemie* 68.6 (1964), pp. 608–608. DOI: https://doi.org/10.1002/bbpc.19640680615.

[26] K. Singh, J. Nowotny, and V. Thangadurai. "Amphoteric oxide semiconductors for energy conversion devices: A tutorial review". In: *Chemical Society Reviews* 42 (Feb. 2013), pp. 1961–1972. DOI: 10.1039/c2cs35393h.

[27] T. Norby. *Lecture notes in Defects and Reactions*. Mar. 2009. URL: https://www.uio.no/studier/emner/matnat/kjemi/KJM5120/v09/undervisnings%20materiale/KJM5120-9120-Defects-and-Reactions-Ch3.pdf.

[28] P. Fielitz and G. Borchardt. "Oxygen exchange at gas/oxide interfaces: How the apparent activation energy of the surface exchange coefficient depends on the kinetic regime". In: *Physical Chemistry Chemical Physics* 18 (2016), pp. 22031–22038. DOI: 10.1039/c6cp02131j.

[29] C. Endler-Schuck, J. Joos, C. Niedrig, A. Weber, and E. Ivers-Tiffée. "The chemical oxygen surface exchange and bulk diffusion coefficient determined by impedance spectroscopy of porous La0.58Sr0.4Co0.2Fe0.8O3 - δ (LSCF) cathodes". In: *Solid State Ionics* 269 (2015), pp. 67–79. DOI: 10.1016/j.ssi.2014.11.018.

[30] R. Merkle and J. Maier. "How is oxygen incorporated into oxides? A comprehensive kinetic study of a simple solid-state reaction with SrTiO3 as a model material". In: *Angewandte Chemie - International Edition* 47 (May 2008), pp. 3874–3894. DOI: 10.1002/anie.200700987.

[31] J. Maier. "Chemical resistance and chemical capacitance". In: *Zeitschrift fur Naturforschung - Section B Journal of Chemical Sciences* 75 (Feb. 2020), pp. 15–22. DOI: 10.1515/znb-2019-0163.

[32] D. Chen, S. R. Bishop, and H. L. Tuller. "Nonstoichiometry in oxide thin films operating under anodic conditions: A chemical capacitance study of the praseodymium-cerium oxide system". In: *Chemistry of Materials* 26 (Nov. 2014), pp. 6622–6627. DOI: 10.1021/cm503440v.

[33] J. Fleig, A. Schmid, G. M. Rupp, C. Slouka, E. Navickas, L. Andrejs, H. Hutter, L. Volgger, and A. Nenning. "The chemical capacitance as a fingerprint of defect chemistry in mixed conducting oxides". In: *Acta Chimica Slovenica* 63 (2016), pp. 509–518. DOI: 10.17344/acsi.2016.2302.

[34] A. Schmid, G. M. Rupp, and J. Fleig. "Voltage and partial pressure dependent defect chemistry in (La,Sr)FeO3δ thin films investigated by chemical capacitance measurements". In: *Phys. Chem. Chem. Phys.* 20 (2018), pp. 12016–12026. DOI: 10.1039/C7CP07845E.

[35] E. Barsoukov and J. R. Macdonald. *Impedance Spectroscopy Theory, Experiment and Applications*. Wiley, Apr. 2004. ISBN: 9781119074083. DOI: 10.1002/0471716243.fmatter.

[36] H. Wang, A. Gaillard, and D. Hissel. "A review of DC/DC converter-based electrochemical impedance spectroscopy for fuel cell electric vehicles". In: *Renewable Energy* 141 (Oct. 2019), pp. 124–138. DOI: 10.1016/j.renene.2019.03.130.

[37] D. V. Ribeiro and J. C. Abrantes. "Application of electrochemical impedance spectroscopy (EIS) to monitor the corrosion of reinforced concrete: A new approach". In: *Construction and Building Materials* 111 (May 2016), pp. 98–104. DOI: 10.1016/j.conbuildmat.2016.02.047.

[38] G. Marín, L. Essaleh, S. Amhil, S. M. Wasim, R. Bouferra, A. Zoubir, M. E. E. A. E. Moujahid, D. P. Singh, and L. Vivas. "Electrical impedance spectroscopy characterization of n type Cu5In9Se16 semiconductor compound". In: *Physica B: Condensed Matter* 593 (Sept. 2020), p. 412283. DOI: 10.1016/j.physb.2020.412283.

[39] D. A. Dean, T. Ramanathan, D. Machado, and R. Sundararajan. "Electrical impedance spectroscopy study of biological tissues". In: *Journal of Electrostatics* 66 (Mar. 2008), pp. 165–177. DOI: 10.1016/j.elstat.2007.11.005.

[40] A. C. Lazanas and M. I. Prodromidis. "Electrochemical Impedance Spectroscopy A Tutorial". In: *ACS Measurement Science Au* (2022), pp. 162–193. DOI: 10.1021/acs\measuresciau.2c00070.

[41] B.-Y. Chang and S.-M. Park. "Electrochemical Impedance Spectroscopy". In: *Annual Review of Analytical Chemistry* 3.1 (2010), pp. 207–229. DOI: 10.1146/annurev.anchem.012809.102211.

[42] J. Huang, Z. Li, B. Y. Liaw, and J. Zhang. "Graphical analysis of electrochemical impedance spectroscopy data in Bode and Nyquist representations". In: *Journal of Power Sources* 309 (2016), pp. 82–98. DOI: https://doi.org/10.1016/j.jpowsour.2016.01.073.

[43] J. Jamnik and J. Maier. "Generalised equivalent circuits for mass and charge transport: Chemical capacitance and its implications". In: *Physical Chemistry Chemical Physics* 3 (2001), pp. 1668–1678. DOI: 10.1039/b100180i.

[44] A. Nenning, A. K. Opitz, T. M. Huber, and J. Fleig. "A novel approach for analyzing electrochemical properties of mixed conducting solid oxide fuel cell anode materials by impedance spectroscopy". In: *Phys. Chem. Chem. Phys.* 16 (2014), pp. 22321–22336. DOI: 10.1039/C4CP02467B.

[45] M. P. Pechini and N. Adams. *Method of preparing lead and alkaline earth titanates and niobates and coating method using the same to form a capacitor*. U.S. Patent 3 330 697, July 1967.

[46] S. Kogler, A. Nenning, G. M. Rupp, A. K. Opitz, and J. Fleig. "Comparison of Electrochemical Properties of La 0.6 Sr 0.4 FeO 3-δ Thin Film Electrodes: Oxidizing vs. Reducing Conditions". In: *Journal of The Electrochemical Society* 162 (2015), pp. 317–326. DOI: 10.1149/2.0731503jes.

[47] M. Morgenbesser. *Diploma Thesis - Electrochemical properties of (La,Sr)(Cr,Mn)O 3-δ thin film electrodes*. 2016. DOI: 10.34726/hss.2016.37331. URL: https://publik.tuwien.ac.at/files/PubDat_252198.pdf.

[48] A. Stangl, A. Riaz, L. Rapenne, J. M. Caicedo, J. D. D. Sirvent, F. Baiutti, C. Jiménez, A. Tarancón, M. Mermoux, and M. Burriel. "Tailored nano-columnar La2NiO4cathodes for improved electrode performance". In: *Journal of Materials Chemistry A* 10 (Feb. 2022), pp. 2528–2540. DOI: 10.1039/d1ta09110g.

[49] M. Valldor and M. Andersson. "ChemInform Abstract: The Structure of the New Compound YBaCo4O7 with a Magnetic Feature." In: *Solid State Sciences* 4 (June 2002), pp. 923–931. DOI: 10.1016/S1293-2558(02)01342-0.

[50] M. Morgenbesser. "Nonstoichiometry in SrTiO3 and its relevance for tunable conductivity and photovoltage". PhD thesis. TU Wien, 2021. DOI: 10.34726/hss.2021.71932. URL: https://repositum.tuwien.at/handle/20.500.12708/18827.

[51] P. Ciambelli, S. Cimino, L. Lisi, M. Faticanti, G. Minelli, I. Pettiti, and P. Porta. "La, Ca and Fe oxide perovskites: preparation, characterization and catalytic properties for methane combustion". In: *Applied Catalysis B: Environmental* 33.3 (2001), pp. 193–203. DOI: https://doi.org/10.1016/S0926-3373(01)00163-1.

[52] K. Rath. *Diploma Thesis - Towards an Improved Understanding of the Oxygen exchange Kinetics close to the Triple Phase Boundary of Platinum and Yttria-stabilised Zirconia*. 2022. DOI: 10.34726/hss.2022.99063. URL: https://repositum.tuwien.at/handle/20.500.12708/19625.

[53] S. P. Badwal, D. Fini, F. T. Ciacchi, C. Munnings, J. A. Kimpton, and J. Drennan. "Structural and microstructural stability of ceria-gadolinia electrolyte exposed to reducing environments of high temperature fuel cells". In: *Journal of Materials Chemistry A* 1 (Sept. 2013), pp. 10768–10782. DOI: 10.1039/c3ta11752a.

[54] C. Endler-Schuck, A. Weber, E. Ivers-Tiffe, U. Guntow, J. Ernst, and J. Ruska. "Nanoscale Gd-Doped CeO2 buffer layer for a high performance solid oxide fuel cell". In: *Journal of Fuel Cell Science and Technology* 8 (2011), p. 041001. DOI: 10.1115/1.4003016.

[55] W. Jung, J. O. Dereux, W. C. Chueh, Y. Hao, and S. M. Haile. "High electrode activity of nanostructured, columnar ceria films for solid oxide fuel cells". In: *Energy and Environmental Science* 5 (Sept. 2012), pp. 8682–8689. DOI: 10.1039/c2ee22151a.

[56] W. C. Chueh and S. M. Haile. "Electrochemical studies of capacitance in cerium oxide thin films and its relationship to anionic and electronic defect densities". In: *Physical Chemistry Chemical Physics* 11 (2009), pp. 8144–8148. DOI: 10.1039/b910903j.

[57] M. Karppinen, H. Yamauchi, S. Otani, T. Fujita, T. Motohashi, Y. H. Huang, M. Valkeapää, and H. Fjellvåg. "Oxygen nonstoichiometry in YBaCo 4O 7+δ: Large low-temperature oxygen absorption/desorption capability". In: *Chemistry of Materials* 18 (Jan. 2006), pp. 490–494. DOI: 10.1021/cm0523081.

[58] S. Huber. "Dissertation - Mass and charge transport properties of Fe-doped SrTiO 3 thin films and their dependence on DC voltage". PhD thesis. TU Vienna, 2014. DOI: 10.34726/hss.2014.21525.